

**INSTRUMENTATION FOR AERODYNAMIC AND THERMAL
PERFORMANCE TESTS OF A TURBINE STAGE IN SHORT-DURATION
FACILITIES**

by

JAMEEL J. JANJUA

Bachelor of Engineering in Chemical and Materials Engineering
Royal Military College of Canada, 2000

Submitted to the Department of Aeronautics and Astronautics
in Partial Fulfillment of the Requirements for the Degree of

MASTER OF SCIENCE

in

AERONAUTICS AND ASTRONAUTICS

at the

MASSACHUSETTS INSTITUTE OF TECHNOLOGY


June 2002

© 2002 Massachusetts Institute of Technology. All rights reserved.

Author: _____

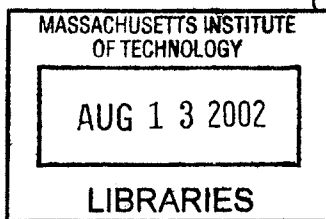
Department of Aeronautics and Astronautics
May 24, 2002

Certified by: _____


Dr. Gerald R. Guenette
Principal Research Engineer
Gas Turbine Laboratory
Department of Aeronautics and Astronautics
Thesis Supervisor

Accepted by: _____

Wallace E. Vander Velde
Professor Aeronautics and Astronautics
Chair, Committee on Graduate Students



AERO

INSTRUMENTATION FOR AERODYNAMIC AND THERMAL PERFORMANCE TESTS OF A TURBINE STAGE IN SHORT-DURATION FACILITIES

by

Jameel J. Janjua

Submitted to the Department of Aeronautics and Astronautics on May 24, 2002, in partial fulfillment of the requirements for the degree of Master of Science in Aeronautics and Astronautics

ABSTRACT

Instrumentation intended for aerodynamic and thermal performance measurements in a rotating turbine facility were design, developed, and fabricated. These included multi-layer, thin-film heat flux gauges and a flow angle probe (FAP). An experimental study of rotor exit tangential flow angle of a fully scaled turbine stage was conducted with the FAP. Spatially-resolved and spatially-average tangential flow angle data are examined and discussed in this study.

The experimental tests were conducted in the MIT Blowdown Turbine Facility using a film-cooled turbine stage. The facility is a short-duration experimental apparatus capable of testing turbine stages under fully scaled conditions, producing useful data for comparison over a time period of approximately 500 ms for each test run. The FAP developed for this project was designed to have sufficient frequency response to resolve certain unsteady characteristics in the turbine flow field. Prior to introducing the FAP into the turbine test section, a detailed calibration was carried out in order to relate measured surface static pressures to tangential flow angles via a non-dimensional pressure parameter. A detailed uncertainty analysis was carried out for the calibration procedure and the reduction of experimental data.

Turbine tests were carried out at several FAP radial positions at the design operating point of the turbine stage. This allowed for radial mapping of the circumferential spatially-averaged flow angle measurements. In addition, some turbine test runs were carried out at high corrected speed operating conditions. Spatially-resolved results were taken to measure flow angle variations through nozzle guide vane (NGV) wakes. Periodic fluctuations observed in the measured flow angle with run time confirmed the expected variations through the NGV wakes. These fluctuations, which were observed to occur with a frequency of approximately 11 Hz, were due to the FAP passing the NGV wakes since the FAP was mounted on a rotating downstream translator for the turbine tests. High corrected speed test runs consistently showed lower spatially-averaged flow angle values than their corresponding design point tests. This is explained by the difference in rotor mechanical speed between these runs.

In addition, the design, development, and fabrication of multi-layer, thin-film heat flux gauges was a portion of this research work. These heat transfer gauges consisted of thin nickel temperature sensors on either side of 25 μm thick polyimide (Kapton[®]) film. The fabrication of these gauges with the desired gauge geometry and material composition employed techniques including electroless nickel deposition, photomachining using an excimer laser, and electrolytic copper plating.

Thesis Supervisor: Dr. Gerald R. Guenette
Title: Principal Research Engineer
Gas Turbine Laboratory
Department of Aeronautics and Astronautics

Acknowledgements

First and foremost, I must express my deepest thanks to my research advisor Dr. Gerald R. Guenette for his undying guidance and instruction. In addition to Jerry's endless wealth of technical knowledge, "the Colonel" was always there to offer a familiar smile and make me feel more at home around the laboratory. I feel truly humbled and honoured to have studied under such an exceptional researcher and human being.

I am also greatly indebted to many of the staff at the Gas Turbine Laboratory, including Lori Martinez, James Letendre, Viktor Dubrowski, Holly Anderson, Mary McDavitt, and Bill Ames. I especially enjoyed working closely with Jack Costa, who was of great assistance in almost every aspect of my experimental research work. In addition to his outstanding technical skills and dedication, Jack was always a good friend and a source of advice on any matter.

I would like to offer my thanks to my friends and fellow students at MIT who have made my experience here more enjoyable. It is not difficult to become enriched when surrounded by a collection of so many exceptional young individuals.

I would be remiss if I did not acknowledge the special role that fellow students Captain Bret Van Poppel and Captain Steven Braddom, United States Army, have played in my personal growth and maturation over the past two years. As a young officer still trying to shape myself, I could always look up to these two individuals as excellent examples of what it really means to be military officer. Thank you, Sirs, for exemplifying leadership.

Another student that has had a significant impact on my work here is William Fournier. I have yet to meet a young individual as bright and curious as Will. As an undergraduate research assistant, he is to thank for helping make so many components of the Blowdown Turbine work properly over the last two years. Will, if I thought that you needed luck in any of your professional endeavours, I'd wish it to you. The fact of the matter is that I have absolutely no doubts in your abilities. However, I would like to see you get that hair cut more than twice a year, kid.

The Canadian Armed Forces have been exceptional with their flexibility in allowing me to pursue my post-graduate studies at this point in my career. Thank you also to all my friends currently serving their country in various roles. Your continual support of me from afar makes me feel proud about my work and efforts. At the same time, I appreciate the job that you do for Canadians on a daily basis.

To my family, thank you for always having faith in my abilities from the beginning. My beloved mother has always pushed me to be at my best, especially in times of adversity and challenge. My big brother, Arif, is and has been the most influential role model and best source of sound advice in my life for as long as I can remember. Thank you both for your love and support.

I extend my gratitude to Alstom Power for sponsoring this research program. None of this work would have been possible without their support.

Per Ardua Ad Astra – Through Adversity to the Stars

Table of Contents

Abstract	3
Acknowledgements	5
Table of Contents	7
List of Figures	11
List of Tables	15
Nomenclature	17
1. Introduction	
1.1. Background	19
1.2. Previous Work	20
1.3. Motivation	21
1.4. Objectives	22
1.5. Thesis Outline	23
2. Blowdown Turbine Test Facility	
2.1. Introduction	25
2.2. Facility Configuration	25
2.2.1. Supply Tank and Fast Acting Valve	27
2.2.2. Test Section	27
2.2.3. Circumferential Probe Translator	30
2.2.4. Eddy Current Brake	31
2.2.5. Critical Flow Venturi Nozzle	32
2.2.6. Coolant Feed System	32
2.2.7. Film-Cooled Turbine Stage	33
2.3. Scaling of Test Condition	34
2.4. Test Procedure	35

2.5. Instrumentation	37
2.5.1. Total Temperature Instrumentation	37
2.5.2. Total Pressure Instrumentation	39
2.5.3. Nozzle Guide Vane Static Pressure Taps	40
2.5.4. Flow Angle Probe	41
2.5.5. Other Instrumentation	41
2.6. Pressure Transducer Calibration	46
2.7. Data Acquisition	47
2.8. Summary	48
3. Heat Flux Gauges	
3.1. Introduction	51
3.2. Multi-Layer, Thin-Film Heat Flux Gauges	53
3.2.1. Multi-Layer, Time-Dependent Heat Conduction Model	53
3.2.2. Gauge Model Discussion	57
3.2.3. Substrate Material Selection	58
3.3. Temperature Sensors	60
3.4. Gauge Fabrication	62
3.4.1. Nickel Deposition on Insulating Substrate	63
3.4.1.1. Cleaning of Substrate Material	63
3.4.1.2. Electroless Nickel Plating	65
3.4.2. Implementing Gauge Geometry and Detail	69
3.4.3. Electrolytic Copper Plating of Gauge Leads	71
3.5. Summary	73
4. Flow Angle Probe	
4.1. Introduction	75
4.2. Flow Angle Probe Design	75
4.3. Pressure Transducers	82
4.4. Flow Angle Probe Installation	83
4.5. Summary	85

5. Flow Angle Probe Calibration	
5.1. Introduction	87
5.2. Motivation	87
5.3. Calibration Procedure	88
5.4. Calibration Results	91
5.4.1. Surface Pressure Measurements	91
5.4.2. Dimensionless Pressure Parameter for Tangential Flow Angle	92
5.4.3. Tangential Flow Angle Calibration Curve	95
5.5. Calibration Error Analysis	96
5.6. Summary	99
6. Flow Angle Probe Experimental Results	
6.1. Introduction	101
6.2. Turbine Operating Point	102
6.2.1. Turbine Stage Operating Point Map	102
6.2.2. Flow Similarity Time Interval	103
6.3. Development of Test Conditions	103
6.4. Approach to Experimental Results	104
6.5. Experimental Error Analysis	112
6.6. Design Operating Point Results	113
6.6.1. Measurement Repeatability	113
6.6.2. Spatially-Resolved Measurements	119
6.6.3. Spatially-Averaged Measurements	126
6.7. High Corrected Speed Results	133
6.7.1. Spatially-Resolved Measurements	133
6.7.2. Spatially-Averaged Measurements	137
6.8. Summary	143
7. Conclusions and Recommendations	
7.1. Review of Objectives	145

7.2. Summary of Work	146
7.3. Recommendations for Future Studies	147
References	149
Appendix A: Heat Flux Gauge Fabrication Procedure	
A.1. Cleaning of Substrate Material	153
A.2. Electroless Nickel Plating	154
A.3. Electrolytic Plating of Gauge Leads	154
A.4. Chemical Compositions	155

List of Figures

2.1:	MIT Blowdown Turbine Test Facility	26
2.2:	Detailed View of Test Section	28
2.3:	Detailed View of Turbine Installation	29
2.4:	Test Section Flow Path	30
2.5:	Schematic of Coolant Feed System	33
2.6:	Detailed View of Temperature Probe Head	38
2.7:	Downstream Total Temperature Rake	39
2.8:	Nozzle Guide Vane Static Pressure Taps	41
2.9:	Typical Differential Pressure Transducer Calibration Trace	47
3.1:	Schematic Cross-Section of Multi-Layer, Thin-Film Heat Transfer Gauges	54
3.2:	Schematic Representation of Simplified Two-Layer Gauge Model	55
3.3:	Structural Formula of Kapton [®] Polyimide	59
3.4:	Detailed Schematic of Gauge Sensor Geometry	70
3.5:	Schematic of Top and Bottom Side of a Single Heat Flux Gauge	70
4.1:	Front and Side Views of Flow Angle Probe Tube and Stem	78
4.2:	Side and Top Views of Flow Angle Probe Tube, with Internal Leads	79
4.3:	Flow Angle Probe Pressure Transducer Wells	81
4.4:	Flow Angle Probe Complete Assembly	83
4.5:	Flow Angle Probe Installed in Blowdown Test Section	84
5.1:	Calibration Arrangement for Flow Angle Probe	89
5.2:	Flow Angle Convention for Flow Angle Probe	90
5.3:	Flow Angle Probe Surface Pressure Measurements with Incident Flow Angle, $M=0.57$	91

5.4:	Flow Angle Probe Dimensionless Pressure Parameter with Incident Flow Angle	94
5.5:	Flow Angle Probe Incident Flow Angle with Experimental Averaged Dimensionless Pressure Parameter (for Mach 0.57, 0.53, 0.47)	95
6.1:	Turbine Stage Operating Point Map, T222	102
6.2:	Filtered Flow Angle Probe Pressure Measurements with Run Time, T222	105
6.3:	Flow Angle Convention with Offset for Flow Angle Probe	106
6.4:	Flow Angle Measurement with Run Time, T222	107
6.5:	Turbine Test Run Operating Point Maps	108
6.6:	Measured Flow Angle Power Spectral Density, T222	110
6.7:	Spatially-Averaged Flow Angle, Stage Corrected Speed, and Stage Pressure Ratio with Run Time over FSTI, T222	111
6.8:	Stage Operating Point Maps, T223 and T224	114
6.9:	Flow Angle Measurement and Uncertainty Bounds with Run Time, T223	115
6.10:	Flow Angle Measurement and Uncertainty Bounds with Run Time, T224	116
6.11:	Spatially-Averaged Flow Angle, Stage Corrected Speed, and Stage Pressure Ratio with Run Time over FSTI, T223	117
6.12:	Spatially-Averaged Flow Angle, Stage Corrected Speed, and Stage Pressure Ratio with Run Time over FSTI, T224	118
6.13:	Flow Angle Measurement and Uncertainty Bounds with Run Time, R=0.15 in., T225	120
6.14:	Flow Angle Measurement and Uncertainty Bounds with Run Time, R=0.35 in., T224	121
6.15:	Flow Angle Measurement and Uncertainty Bounds with Run Time, R=0.54 in., T222	122
6.16:	Flow Angle Measurement and Uncertainty Bounds with Run Time, R=0.75 in., T227	123
6.17:	Flow Angle Measurement and Uncertainty Bounds with Run Time, R=0.94 in., T229	124
6.18:	Spatially-Averaged Flow Angle, Stage Corrected Speed, and Stage Pressure Ratio with Run Time over FSTI, R=0.15 in., T225	126
6.19:	Spatially-Averaged Flow Angle, Stage Corrected Speed, and Stage Pressure Ratio with Run Time over FSTI, R=0.35 in., T224	127
6.20:	Spatially-Averaged Flow Angle, Stage Corrected Speed, and Stage Pressure Ratio with Run Time over FSTI, R=0.54 in., T222	128

6.21:	Spatially-Averaged Flow Angle, Stage Corrected Speed, and Stage Pressure Ratio with Run Time over FSTI, R=0.75 in., T227	129
6.22:	Spatially-Averaged Flow Angle, Stage Corrected Speed, and Stage Pressure Ratio with Run Time over FSTI, R=0.94 in., T229	130
6.23:	Average Turbine Tangential Flow Angle with Normalized Flow Angle Probe Radial Position at Design Operating Point, (t = 600-650 ms)	132
6.24:	Flow Angle Measurement and Uncertainty Bounds with Run Time, R=0.15 in., T226	134
6.25:	Flow Angle Measurement and Uncertainty Bounds with Run Time, R=0.75 in., T228	135
6.26:	Flow Angle Measurement and Uncertainty Bounds with Run Time, R=0.94 in., T230	136
6.27:	Spatially-Averaged Flow Angle, Stage Corrected Speed, and Stage Pressure Ratio with Run Time over FSTI, R=0.15 in., T226	137
6.28:	Spatially-Averaged Flow Angle, Stage Corrected Speed, and Stage Pressure Ratio with Run Time over FSTI, R=0.75 in., T228	138
6.29:	Spatially-Averaged Flow Angle, Stage Corrected Speed, and Stage Pressure Ratio with Run Time over FSTI, R=0.94 in., T230	139
6.30:	Rotor Exit Velocity Triangles for Design and High Mechanical Speed	140
6.31:	Average Turbine Tangential Flow Angle with Normalized Flow Angle Probe Radial Position at Design Operating Point and High Corrected Speed, (t = 600-650 ms)	142

List of Tables

2.1:	MIT Blowdown Turbine Facility Scaling	35
2.2:	Blowdown Turbine Instrumentation	43
2.3:	Blowdown Turbine Facility Data Acquisition System	48
3.1:	Bulk Material Properties of Various Film Thermometer Materials	62
6.1:	Flow Angle Probe Test Run Summary	104
6.2:	Measurement Repeatability Test Matrix	118
6.3:	Design Operating Point Test Matrix	131
6.4:	High Corrected Speed Operating Point Test Matrix	139

Nomenclature

Roman

<i>a</i>	Speed of sound
<i>c</i>	Intercept of line of best fit
<i>c</i>	Specific heat capacity
<i>d</i>	Thickness of insulating substrate
<i>f_c</i>	Response frequency bandwidth
<i>k</i>	Thermal conductivity
<i>l</i>	Film sensor length
<i>m</i>	Slope of line of best fit
<i>q</i>	Heat flux
<i>q_d</i>	Heat dissipation
<i>r</i>	Experimental result for uncertainty analysis
<i>t</i>	Film sensor thickness
<i>t</i>	Time
<i>w</i>	Film sensor width
<i>x</i>	Heat flux gauge depth coordinate
<i>z</i>	Valence electron count
<i>L</i>	Layer thickness for heat flux gauge model
<i>M</i>	Mach number
<i>N</i>	Number of data pairs
<i>N_c</i>	Corrected speed
<i>P</i>	Pressure
<i>Q</i>	Dynamic pressure
<i>R</i>	Electrical resistance
<i>R</i>	Specific gas constant
<i>Re</i>	Reynolds Number
<i>T</i>	Temperature
<i>U</i>	Absolute random uncertainty
<i>V</i>	Voltage
<i>X</i>	Measured variable for uncertainty analysis

Greek

<i>α</i>	Temperature coefficient of resistivity
<i>γ</i>	Ratio of specific heats

δ	Offset angle for flow angle probe sensing locations
θ	Absolute tangential flow angle
θ'	Relative tangential flow angle
κ	Thermal diffusivity
ρ	Density
ρ	Electrical resistivity
ψ	Dimensionless pressure parameter
ω	Frequency of input heat load
ω_c	Heat flux sensor cutoff frequency
ω_r	Mechanical Speed
Δ	Change in quantity

Subscripts

0	Total or stagnation quantity
<i>offset</i>	Offset flow angle quantity
<i>rel</i>	Relative flow angle quantity
C	Centre flow angle probe location
L	Left flow angle probe sensing location
R	Right flow angle probe sensing location

Acronyms

ABS	Acrylonitrile Butadiene Styrene
ASME	American Society of Mechanical Engineers
ANSI	American National Standards Institute
BDT	Blowdown Turbine
CFD	Computational Fluid Dynamics
DAQ	Data Acquisition
DSA	Direct Sensor Array
EDM	Electrical Discharge Machining
FAP	Flow Angle Probe
FSTI	Flow Similarity Time Interval
GTL	Gas Turbine Laboratory
MACOR	Machineable Ceramic
MIT	Massachusetts Institute of Technology
NGV	Nozzle Guide Vane
NIST	National Institute of Standards in Technology
PR	Pressure Ratio
PSD	Power Spectral Density
RTD	Resistance Temperature Detector

Chapter 1: Introduction

1.1 Background

The aerodynamic performance and efficiency of gas turbine engines has seen dramatic increases since the inception of these devices some half a century ago. Axial flow gas turbine engines used for electrical power generation currently operate with polytropic efficiencies in excess of 90 % and turbine inlet temperatures above 1700 K. Continual efforts to improve performance of gas turbine engines require a variety of unique instrumentation capable of acquiring relevant data. Devices designed to measure heat loads experienced by engine components have been among those at the focus of various research efforts in the past decade. In addition, instruments that measure flow characteristics inside turbine engines are also of interest because of the difficulty associated with accurately modeling these flow fields using computer simulations. There have been significant advances in the field of Computational Fluid Dynamics (CFD) in recent times, but experimental testing should always be performed to support and validate such activities.

In both research circles and industry alike, experimental gas turbine testing has been used to make various aerodynamic and thermal performance measurements. However, current steady-state turbine testing practices have proven to be very expensive and impractical. The cost associated with a steady-state gas turbine experiment can easily be in the millions of dollars for relatively simple test conditions. As a result, steady-state testing is not a practical alternative at academic institutions. In the specific case of turbine engine used for power generation, full-scale, steady-state experimental apparatus are not used due to their large size and resource requirements. In these cases, engine components are typically tested in service, thus resulting in minimal improvements in efficiency and performance over the life of an engine due to constraints imposed on in-service equipment.

In the early 1980's, the Blowdown Turbine (BDT) was developed at the Massachusetts Institute of Technology's (MIT) Gas Turbine Laboratory (GTL) in order to study turbine performance. The BDT is a fully-scaled, short-duration experimental test facility. Using transient testing techniques, researchers at the GTL have been able to obtain highly accurate data relating to aerodynamic and thermal performance of axial flow turbines. The time scales associated with this short duration test facility are on the order of several hundred milliseconds. Useful data relating to steady-state operation can be obtained using instrumentation with sufficiently high frequency response. Both turbine inlet temperature and rotor tip speed can be significantly reduced in such an apparatus by scaling appropriate dimensionless parameters including Reynolds number, total stage pressure ratio, gas-to-wall temperature ratio, and corrected speed. A facility such as the BDT requires far fewer overall resources for its construction, maintenance, and operation than its steady-state counterparts.

Various instruments for aerodynamic and thermal measurements have been previously developed during research programs for the BDT. A program to develop instrumentation intended to measure the heat transfer rates to individual blades, and to develop instrumentation and measure the rotor exit flow angle of a film-cooled turbine stage has been undertaken. This thesis is a summary of research efforts focused on these goals.

1.2 Previous Work

A brief summary of the work conducted on the MIT Blowdown Turbine Facility since its construction in the early 1980's is included below.

The MIT Blowdown Turbine Facility was design and constructed by Guenette [8]. Initial work on the facility was focused on the design and development of the fundamental components of the test apparatus. Significant effort was involved in the development of the fast-acting main valve, eddy current brake, and heat flux instrumentation. Early research efforts focused on heat transfer measurements to the tip casing and nozzle guide vanes in an uncooled turbine stage.

Shang [19] examined the influence of non-uniformities in turbine inlet temperature on the heat transfer to turbine blades. Radial temperature distortions were found to have a significant effect on blade heat transfer, while circumferential distortions seemed to have little impact.

Keogh [10] and Spadaccini [25] examined and compared the aerodynamic performance of uncooled and film-cooled turbine stages. Significant modifications to the existing turbine stage were required in order to incorporate film-cooling. Keogh [10] also examined and quantified the specific aerodynamic losses associated with the addition of film-cooling.

Van Poppel [28] made measurements of heat transfer rates to the tip casing of the turbine stage under various operating conditions. This required the design and fabrication of a complicated instrumented tip casing insert.

1.3 Motivation

The characterization of flow fields, including the measurement of flow angle, is not a new endeavour. Several pieces of literature exist [3,14] that describe various aspects of flow measurement including the design and fabrication of appropriate instruments. These instruments are easily incorporated in stationary apparatus such as blade cascades. However, the task of flow characterization in rotating turbomachinery is a much more complicated task. Research work focused on measuring the flow characteristics in experimental engines with rotating components, such as the MIT Blowdown Compressor Facility, has been conducted in the past [16,27]. Thompkins and Kerrebrock [27] studied the flow, including flow angles, ahead and downstream of a high-work transonic compressor rotor in order to develop theoretical models capable of quantitatively describing the flow. Often times, however, such studies do not include a comprehensive uncertainty analysis, which is extremely useful in validating experimental data. These types of measurements have not to date been made in the MIT Blowdown Turbine Facility. The most significant portion of the research reported herein was conducted in order to obtain spatially-resolved rotor exit tangential flow angle

measurements, with an appropriate uncertainty analysis, that may be used in comparisons with other theoretical predictions of flow field in the turbine stage tested.

Both semi-infinite and thin-film heat flux gauges have been employed to make heat transfer measurements on various turbine engine components in the past. The task of making these measurements on the surface of rotating blades is extremely difficult. Guenette [8] was successful in achieving this using multi-layer, thin-film heat flux gauges in previous research efforts, but the fabrication methods used to produce these gauges proved too difficult to make their duplication a worth while activity in subsequent test series. The development of innovative methods to produce such gauges was required in order to render a gauge manufacturing process that was sufficiently reliable to be applied to subsequent experimental testing. This effort was also a portion of the research that is the subject of this document.

1.4 Objectives

The objectives involved in this research effort revolved around instrumentation for aerodynamic and thermal performance measurements in a short-duration turbine test facility. These objectives include:

- 1) The design and fabrication of an instrument capable of measuring the tangential flow angle in a short-duration test facility with adequate sensitivity and frequency response to resolve spatial flow characteristics associated with circumferential surveys
- 2) The calibration of the flow angle measuring device in a separate wind tunnel to allow for the experimental determination of flow angle from raw pressure measurements
- 3) The integration of the flow angle instrument into the existing downstream translator of the turbine test section with the provision varying the radial height of the probe once installed

- 4) The measurement of tangential flow angle downstream of the turbine rotor in the test section
- 5) The design of multi-layer, thin-film heat flux gauges capable of measuring heat transfer rates to turbine blades with sufficient frequency response
- 6) The development of new fabrication techniques for reliably manufacturing multi-layer, thin-film heat flux gauges

1.5 Thesis Outline

This chapter outlines the content of the thesis, reviews previous research work in the Blowdown Turbine Facility and other related work, and reviews the motivation and objectives of the project. Chapter 2 introduces the MIT Blowdown Facility including details of the primary components. Facility scaling issues and typical run conditions are discussed. Details pertaining to recent modifications to the facility, instrumentation, and data acquisition system are discussed. The design, development, and fabrication of multi-layer, thin-film heat flux gauges capable of measuring heat transfer to turbine blades are discussed in Chapter 3. This section also includes a gauge model and selection criteria for the design and materials selected for these gauges. Chapter 4 presents the design, development, and fabrication of a three-hole, hemispherical-nose, multi pressure sensor, flow angle probe (FAP). The integration of the FAP into the existing Blowdown Facility is also discussed. The calibration of the FAP that was performed prior to implementing the probe into the test section is the subject of Chapter 5. A description of the calibration procedure and associated analysis of the calibration results is included. In addition, a detailed error analysis of the calibration of the FAP is also discussed. Chapter 6 discusses the experimental results obtained using the FAP in the Blowdown Facility. The development of the test conditions and the approach taken to analyze the experimental results are included in this chapter. Both spatially-resolved and spatially-averaged tangential flow angle results are presented and discussed. Results from several radial FAP positions are included to map the tangential flow angle at different turbine

stage operating point settings. Chapter 7 is the conclusion of the thesis, including a summary of the results and recommendations for future research work.

Chapter 2: Blowdown Turbine Test Facility

2.1 Introduction

The MIT Blowdown Turbine Facility is a short-duration, blowdown wind tunnel capable of accommodating a complete, rotating stage in an environment that rigorously simulates the fluid physics and heat transfer phenomena that occur in a turbine. This chapter presents an overview of the MIT Blowdown Turbine Facility. A description of the facility design, configuration, and operational procedures is included. Scaling of the turbine operating point for achieving full-scale similarity is discussed. Both the individual components and instrumentation used are examined herein. The data acquisition system is also briefly presented.

2.2 Facility Configuration

The MIT Blowdown Turbine Test Facility is shown in Figure 2.1. The facility consists of seven primary components: the supply tank, fast acting valve, test section, eddy current brake torque meter, critical flow venturi nozzle, coolant feed system (not shown), and dump tank. A detailed review of the overall design of the facility can be found in Guenette [8].

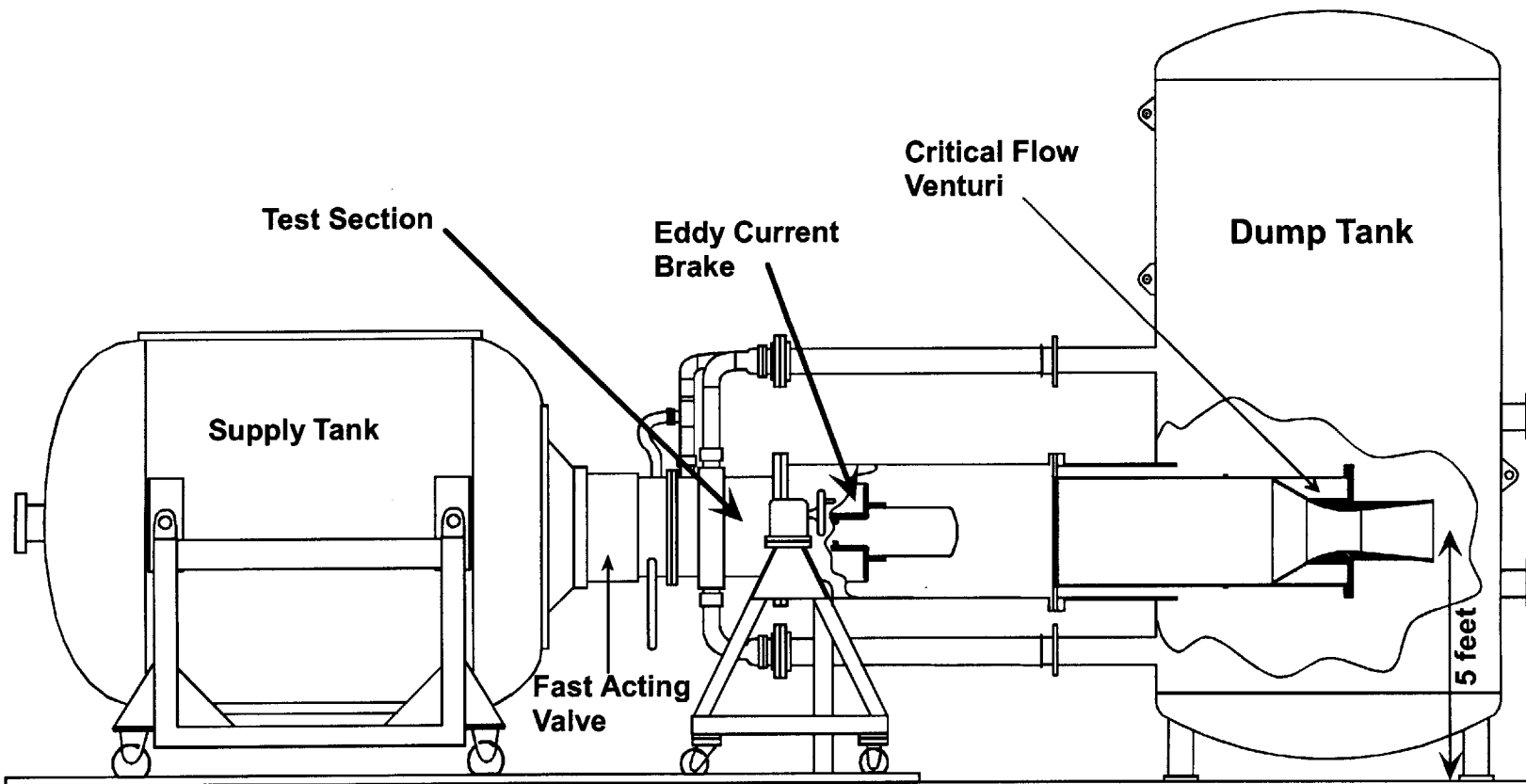


Figure 2.1: MIT Blowdown Turbine Test Facility

2.2.1 Supply Tank and Fast Acting Valve

The supply tank is a 364 ft³ cylindrical pressure vessel rated at 150 psia. It is surrounded by an external jacket through which heat transfer oil is circulated to warm the tank to the desired test temperature. An electric stirring fan is employed to ensure a uniform test gas temperature distribution.

The test section is separated from the supply tank by a fast-acting, axially traversing, plug valve. This valve is designed to fully open in approximately 50 ms and introduce disturbance-free flow into the test section. Valve dynamics are controlled by damping chambers, which produce a force on the plug whose magnitude and direction depend on its position and velocity. In its fully closed position, this force acts to seal the plug. After the seal is broken, the valve plug is accelerated open. As it nears its fully open position the plug is decelerated to rest. An internal pneumatic piston assembly actuated by a small compressed argon gas cylinder provides the force used to break the seal.

2.2.2 Test Section

A cut-away of the test section assembly is shown in Figure 2.2 and Figure 2.3. The test section is composed of the forward frame, main frame, and the rotor unit. The forward frame contains the nozzle guide vanes, the inlet boundary layer bleeds, and the rotor heat shield and mates to the main valve. The forward frame is followed by the main frame, which houses the turbine rotor assembly, the downstream probe translator package, the eddy current brake magnet assembly, the turbine throttle, and drive motor. The rotor unit contains the rotor discs, blades, bearings, shaft, and the eddy current brake 'loss' drum (not shown). This drum is inserted into the eddy current brake magnet assembly.

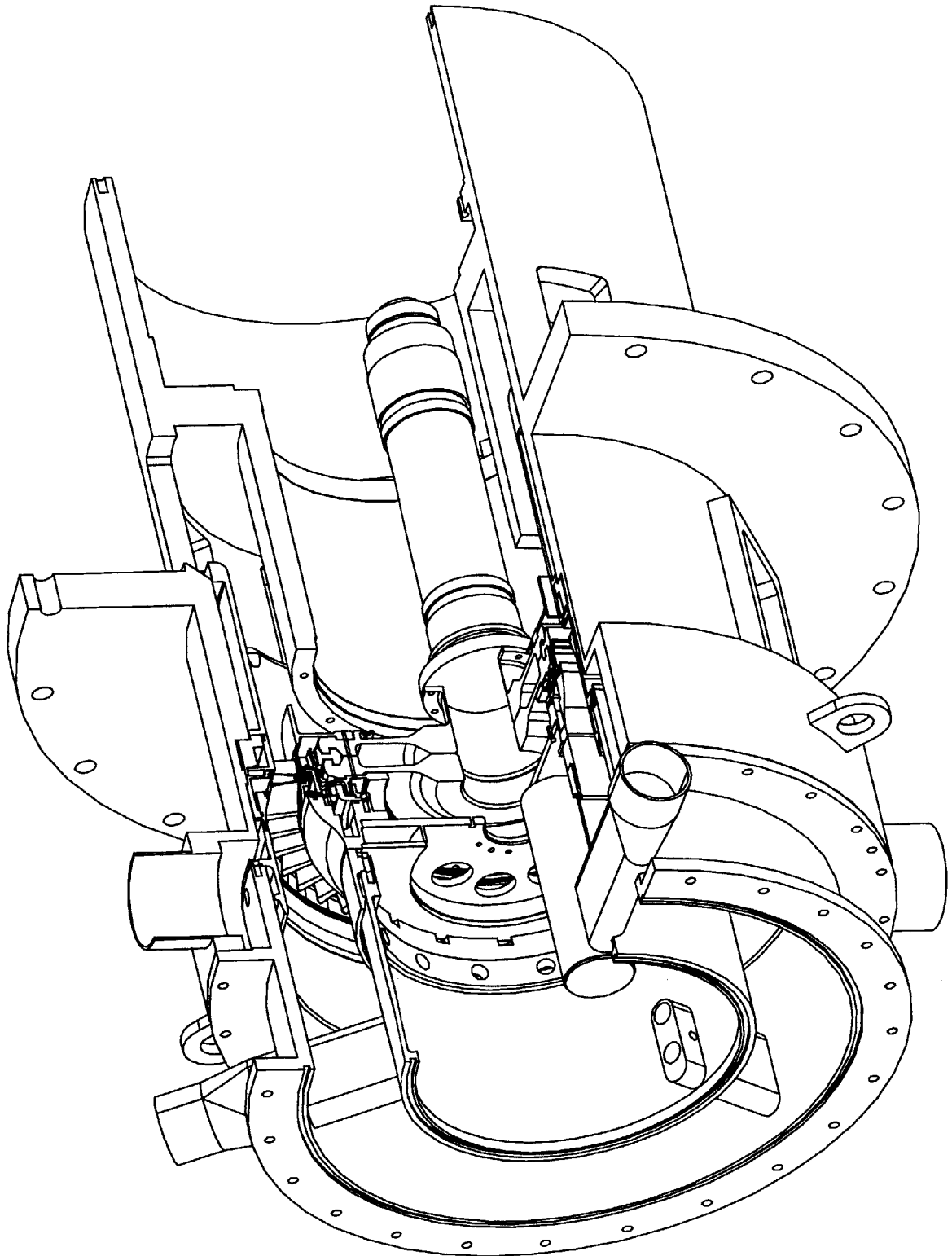


Figure 2.2: Detailed View of Test Section

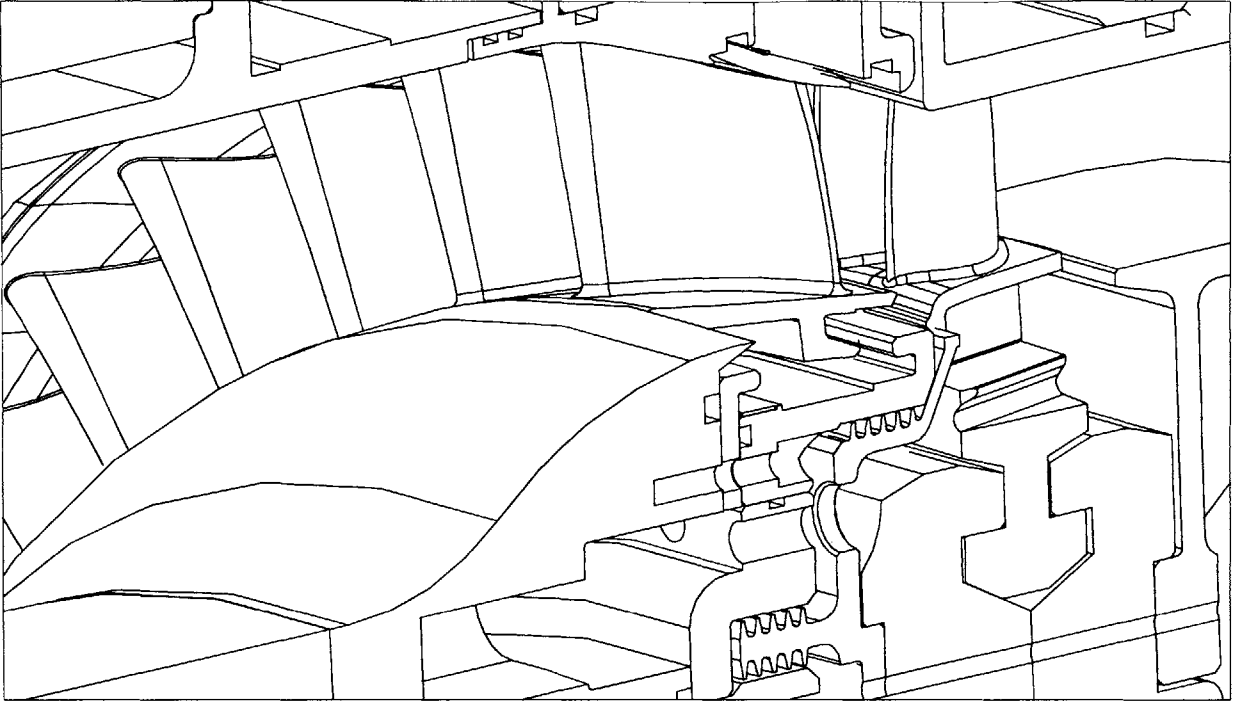


Figure 2.3: Detailed View of Turbine Installation

A cross-sectional view of the test section flow path is shown in Figure 2.4. Upstream of the turbine stage a boundary layer bleed provides clean inlet flow. The rotor exit flow is exhausted through an adjustable throttling area to provide the desired pressure ratio across the turbine. During the usable portion of the test, this area is choked. Also shown in Figure 2.4 are the upstream and downstream measurement locations. Downstream, the total temperature and pressure probes, and a flow angle probe are mounted on a circumferential translator.

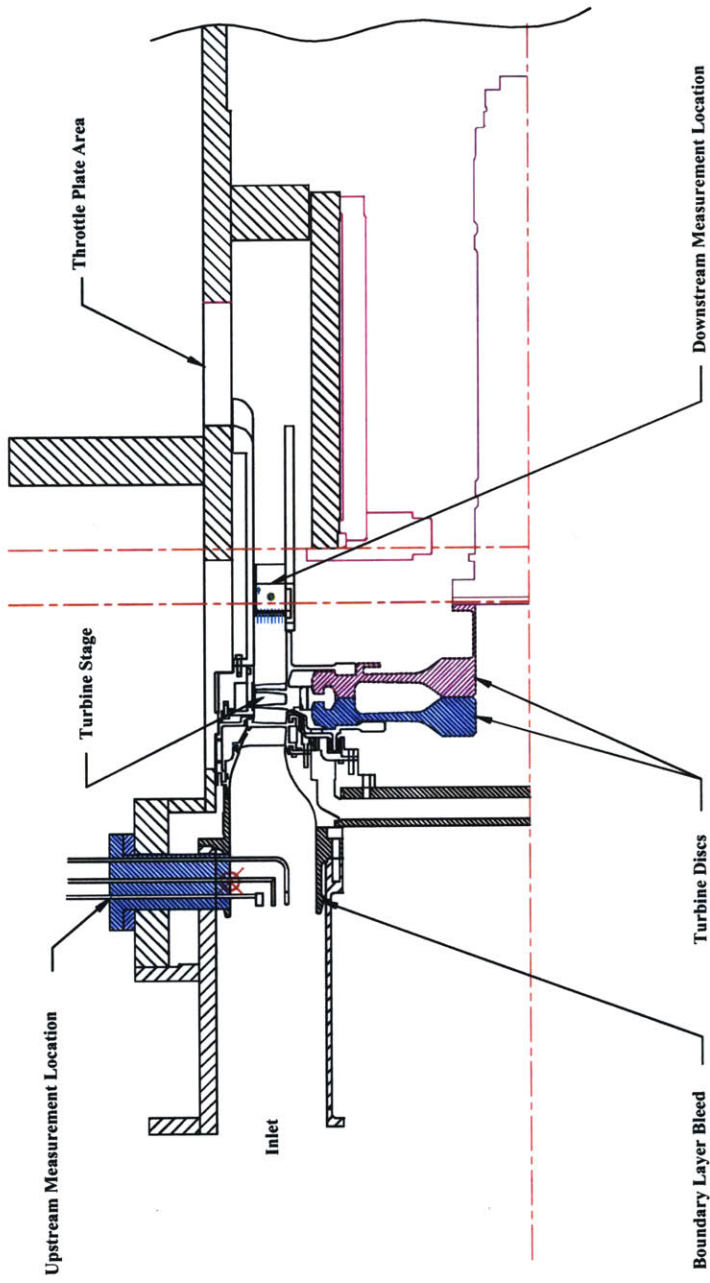


Figure 2.4: Test Section Flow Path

2.2.3 Circumferential Probe Translator

A downstream circumferential translator is available to provide measurement of non-axisymmetric features of the turbine flow field. Circumferential non-uniformities downstream of the turbine stage are a result of nozzle guide vane wakes. Downstream

flow field measurements are thus biased by their circumferential location. The downstream translator is used as a solution to this problem in the MIT Blowdown Facility. For all of the experiments reported herein, the downstream translator was employed with instrumentation.

The downstream translator is composed of a drum forming the inner annulus of the turbine exit and is mounted on thin-line bearings. The downstream translator houses three ‘canisters’ spaced 20° apart, which contain the appropriate electrical and pneumatic connections to support total temperature or pressure rakes, or other instrumentation. Connections are also available for several wall static pressure taps. The translator is restricted to a 350° rotation angle by a spring-loaded hard stop to prevent the translator from freely spinning and destroying the canisters' electrical wiring. A Baldor ME-4090-BLBCE servomotor drives the translator, delivering approximately 3 in-lb of torque through an equivalent 13.5:1 gear ratio. This motor is controlled by a Galil DMC-400-10 card and powered by a Copley MB6-10 amplifier. In addition to the hard stop, an aluminum shear pin is installed on the shaft coupling exiting the servomotor to prevent translator runaway. The downstream translator rotates at a constant angular speed of approximately 0.25 revolutions per second during the test window [9].

2.2.4 Eddy Current Brake

The eddy current brake serves as both the turbine load and the turbine torque meter. It consists of two components: a cylindrical Inconel drum directly attached to the rotor shaft and a stationary array of DC-excited electromagnets arranged circumferentially around the drum. Electric currents are induced in the drum as it rotates through the applied magnetic field. The flow of this current through the electrical resistance of the drum dissipates the power produced by the turbine, which appears as resistive heating of the drum. Setting the magnitude of the applied magnetic field controls turbine speed.

The braking system was modified by Keogh [10] to serve as a shaft torque meter. The electromagnet assembly was mounted on bearings and the braking torque was measured through two load cells.

2.2.5 Critical Flow Venturi Nozzle

A critical flow venturi, developed and installed by Keogh [10] and Spadaccini [25] in line with the exit flow path, is used to measure the mass flow rate through the turbine. The nozzle design and upstream duct requirements are based on the American National Standards Institute (ANSI) standard [2] for a toroidal throat critical flow venturi. Modifications to the facility were required to meet installation requirements for the nozzle. A 66 in. extension was added between the dump tank and main frame in order to relocate the eddy current brake and starter motor. Extensions were also required to connect the boundary layer bleeds to the dump tank, and to connect the fill system to the supply tank.

A 50 % open area screen is installed at the entrance to the upstream duct. This reduces the total pressure non-uniformity caused by the stepped transition from annular to circular cross section around the starter motor. The nozzle was calibrated with the upstream duct and a simulated blockage in place.

The nozzle was designed and built by Flow Systems Incorporated of Boulder Colorado and calibrated by Colorado EESI. This calibration is traceable to the National Institute for Standards and Technology (NIST). A cross section of the critical flow venturi nozzle is shown in Figure 2.1.

2.2.6 Coolant Feed System

The coolant system consists of a coolant supply tank, a fast-acting pneumatic ball valve, a pipe network, and several orifice plates for metering the flow. In a similar manner to the facility itself, the cooling system operates in a blowdown mode. The existing facility coolant system was modified by Spadaccini [25] to provide three independent and separately metered streams to the rotor blades, vanes, and tip casing.

The coolant supply tank is 3.97 ft³ and has a pressure rating of 450 psia. Like the main supply tank, it is surrounded by a metal jacket and insulation for controlling tank temperature. A flow of liquid nitrogen mixed with compressed air is used to cool the

tank lining and the coolant gas to the desired temperature. The fast-acting ball valve at the tank exit is actuated by a 1000 psi argon bottle. It is triggered simultaneously with the main valve and closes approximately 1.2 s later. The piping network feeds the coolant gas from the coolant supply tank into the test section and to the turbine.

An overhead view of this network can be seen in Figure 2.5. Three independent feed lines are employed, one each to the rotor blades, nozzles, and tip casing. The flow is split in a manifold downstream of the ball valve. A thick, square edged, choked orifice with known discharge coefficient meters each feed split. Each orifice accurately sets the mass flow to each turbine component, provided the desired flow ratio.

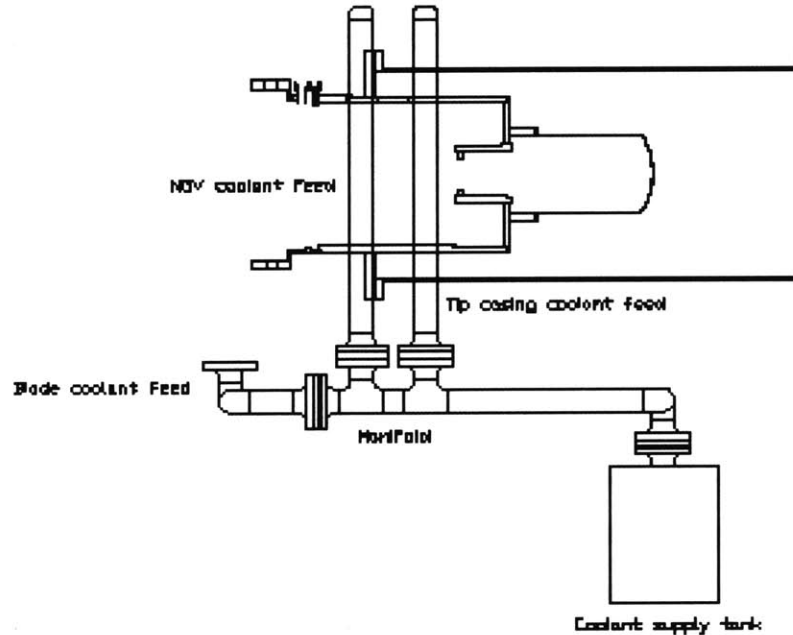


Figure 2.5: Schematic of Coolant Feed System

2.2.7 Film-Cooled Turbine Stage

In order to modify the uncooled turbine stage for coolant flow injection, the $\frac{1}{4}$ -scale film-cooled model turbine was required to have similar external geometry, including film hole quantity, distribution, diameters, and injection orientations over the airfoil surfaces. However, the internal passages were not directly replicated since the

focus of the program was on external heat transfer. Keogh [10] and Spadaccini [25] made extensive modifications to the existing non film-cooled turbine stage. Sophisticated machining techniques, including electrical discharge machining (EDM), and laser machining were employed to produce the film cooling holes.

The nozzle guide vanes, rotor blades, and the tip casing were modified for cooling. Nozzle guide vanes were retrofitted with 12 rows of coolant injection holes on the airfoil surface, as well as several holes on the upper and lower platforms. Two vertical channels were required to feed all of the airfoil surface cooling holes. Coolant was supplied to the platform holes via manifolds above and below the locations where the vanes mate to the facility. The scaled film-cooled turbine blades include five rows of coolant injection holes: two on the leading edge, one on the suction surface and one on the pressure surface. The leading edge holes are oriented at compound angles. Although not used for this experiment, the rotor tip casing was modified with film-cooling holes on the leading and trailing edges of the tip casing ring.

2.3 Scaling of Test Conditions

Validity of scaled wind tunnel experiments depends on the similarity between the test flow and the actual flow being simulated. In dimensionless form, the equations for mass continuity, momentum and energy transfer produce non-dimensional parameters that completely characterize the physics of flow field. Similarity between experiment and reality only requires that these non-dimensional parameters be reproduced.

For an uncooled turbine stage operating under adiabatic conditions, corrected mass flow and total temperature ratio (or efficiency) depend on four dimensionless parameters: total pressure ratio, corrected speed, Reynolds number, and specific heat ratio [8]. Two additional parameters are required to simulate the heat flux distribution: the gas-to-wall temperature ratio and the Prandtl number. For a film-cooled turbine test, the coolant mass and momentum flux ratios must also be reproduced. These parameters, which govern test similarity, can be matched by properly setting the facility initial operating conditions.

The operating conditions consist of the test gas composition, upstream total temperature and pressure, coolant total temperature and pressure, mechanical speed, throttle area, and brake excitation. The supply tank temperature is set by matching the gas-to-wall temperature ratio. Specific heat ratio is matched by setting the test gas mixture ratio, typically argon and carbon dioxide. Shaft mechanical speed is set by matching the corrected speeds. Initial supply pressure is set by the Reynolds number, and pressure ratio by the downstream throttle position. Table 2.1 summarizes the conditions of a typical blowdown experiment and compares them to that of a full scale engine.

Table 2.1: MIT Blowdown Turbine Facility Scaling

Parameter	Full Scale Engine	MIT Blowdown Facility
Working Fluid	Air	Argon-CO ₂
Ratio of Specific Heats	1.28	1.28
Mean Metal Temperature	1100 K	300 K
Metal to Gas Temperature Ratio	0.647	0.647
Inlet Total Temperature	1700 K	464 K
Reynolds Number	5.6 x 10 ⁶	5.6 x 10 ⁶
Inlet total Pressure	15 atm	7 atm
Exit Total Pressure	7.4 atm	3.47 atm
Exit Total Temperature	1470 K	401 K
Prandtl Number	0.928	0.742
Design Rotor Speed	3600 rpm	5954 rpm
Design Mass Flow	312 kg/s	23.3 kg/s
Coolant/Inlet Flow	9.8 %	9.8 %
Stage Power Output	91 MW	1.26 MW
Test Time	Continuous	~ 0.800 s

2.4 Test Procedure

Preparations for a blowdown experiment begin by determining the required conditions for achieving full-scale turbine operating point. These consist of the upstream total temperature and pressure, coolant total temperature and pressure, test gas composition, mechanical speed, throttle area, and brake excitation. The experiment then proceeds as follows:

- 1) The entire facility is evacuated and the throttle plate is positioned for a predetermined area based on operational experience.

- 2) The main supply tank is heated to the desired upstream total temperature and is brought to thermal equilibrium.
- 3) The main valve is sealed and the supply tank is filled with the required test gas mixture to the desired upstream total pressure.
- 4) Simultaneously, the coolant supply tank is filled to the desired pressure and cooled to the predetermined temperature.
- 5) At this post-fill state, all differential pressure transducers are calibrated by cycling their back-pressure ports between vacuum and atmosphere. This provides a scale factor for each transducer. Instrumentation and calibration are discussed in further detail below.
- 6) The brake excitation is set.
- 7) The data acquisition system and translator servo-motor controller are set to stand-by mode and are waiting to be triggered.
- 8) The turbine rotor is then accelerated to the desired mechanical speed by a starter motor.
- 9) Once this speed is exceeded, the motor is powered down and the rotor spins freely in the vacuum. It is slowly decelerated by bearing friction and the applied back EMF of the drive motor.
- 10) When the decelerating rotor reaches the preset speed, a trigger causes the main valve and coolant ball valve to open. Simultaneously, the data acquisition system begins collecting data, the downstream translator begins its traverse, and the eddy current brake torque meter is energized.
- 11) The test gases then flow through the test section and quasi-steady state operation is reached after a 300 ms transient. The useful test window is approximately 500 ms.
- 12) After approximately 1.2 s the coolant ball valve closes and the brake is turned off.
- 13) The rotor decelerates and comes to a stop.
- 14) Once the gas inside the tunnel stabilizes, all differential pressure transducers are re-calibrated to check for drift.
- 15) The tunnel is then re-evacuated and cooled to room temperature.

2.5 Instrumentation

The facility was designed to provide a relatively benign experimental environment for flow measurement. The nature of the short duration experiment imposes a strict requirement on the time response of instrumentation used to sample its flow field. Performance calculations based on these measurements also require a high level of instrumentation accuracy. These considerations led to the development of highly accurate total temperature and pressure instrumentation with the capability of accurately characterizing turbine performance.

2.5.1 Total Temperature Instrumentation

The MIT Gas Turbine Laboratory has engaged in the development of total temperature probes for use in turbine aero-performance measurements in the Blowdown Test Facility. With each new design, time response and instrument accuracy generally improved. Work focused on reducing the transient errors resulting from the heat transfer processes within the thermocouple junction support wires and led to a design with much faster time response than previously achieved. Special attention was also given to the probe head design to reduce probe sensitivity to flow angle, which is important for downstream wake measurements.

Details of the temperature probes are shown in Figure 2.6 and Figure 2.7. The measurement heads consist of 0.0005 in. diameter type-K thermocouple junctions mounted in vented stagnation tubes. The rake probe shown in Figure 2.7 is mounted on the downstream translator and contains an internal temperature reference junction. A stationary six head version is mounted upstream of the turbine. The radial rake with six heads is positioned roughly mid-way between two of the facility's inner annulus support struts. The inlet rake can employ either an internally mounted or external reference junction.

Three additional single head probes, spaced 120° apart, are mounted upstream at mid-span on the inlet annulus. The thermocouple reference junctions for these probes are

external. Three total temperature probes are dedicated to monitoring the flow through the critical flow venturi nozzle. These probes are also 0.0005 in. diameter type-K thermocouples and have similar time response and accuracy to the upstream probes.

The cooling system is instrumented with seven type-K thermocouples. These probes do not require the time response of the turbine inlet and outlet sensors and employ 0.003 in. junctions. These probes are located at points upstream of the choked metering orifices and as close as possible to where the coolant enters the test section.

With the exception of the turbine inlet and outlet rakes, all thermocouples are referenced to Omega TRCIII ice point cells. The signals are processed using high stability DC amplifiers and filters prior to being recorded by the data acquisition system. The long-term static accuracy of the system—consisting of the measurement head, reference junction and signal conditioning electronics—is 0.13 K.

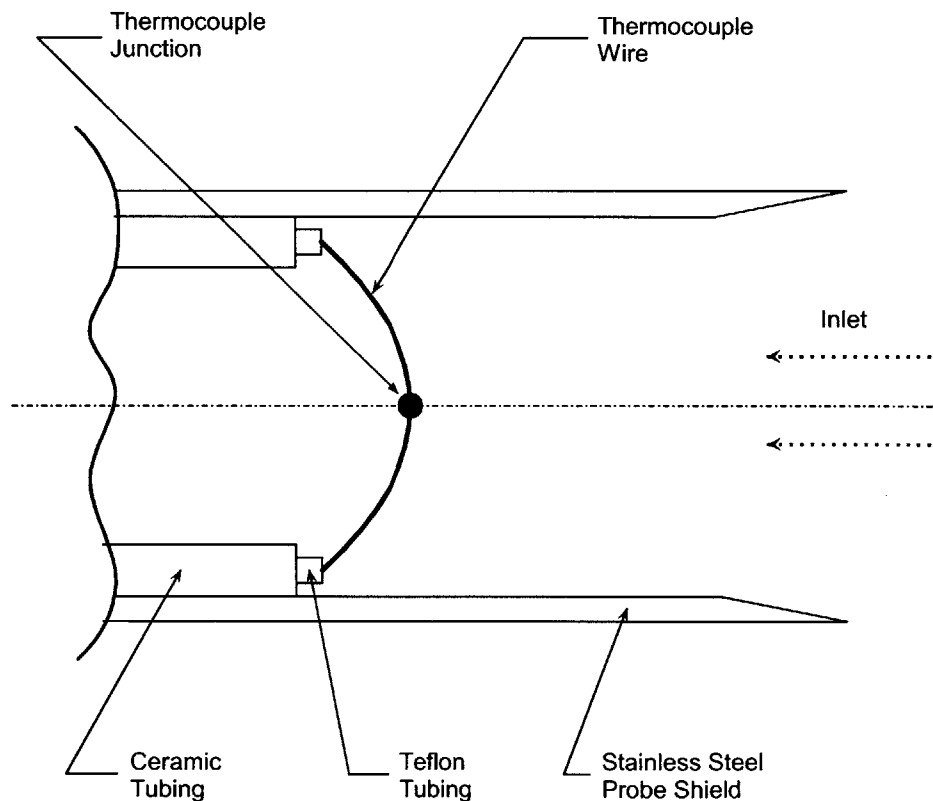


Figure 2.6: Detailed View of Temperature Probe Head

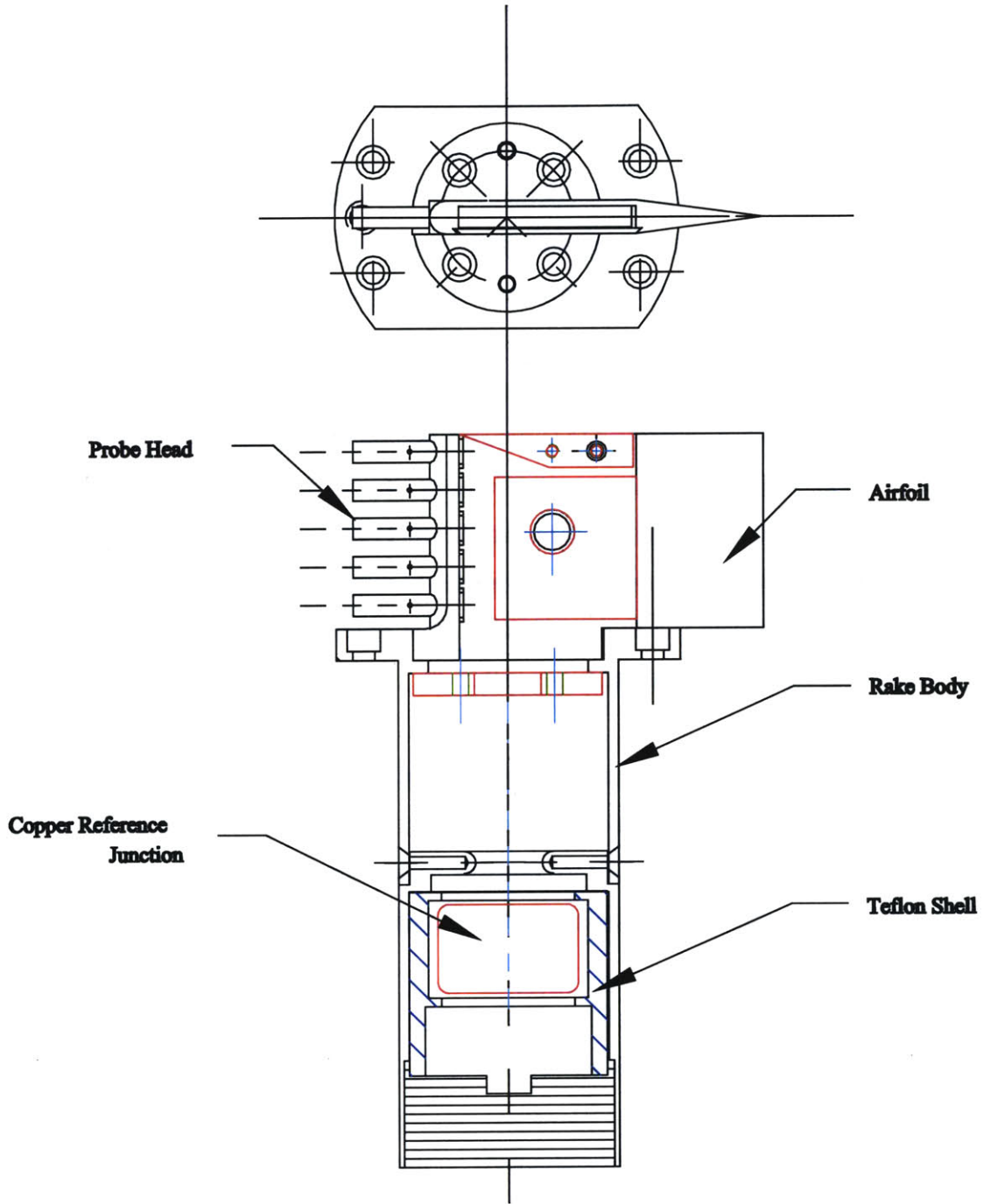


Figure 2.7: Downstream Total Temperature Rake

2.5.2 Total Pressure Instrumentation

The primary concerns in the design of the total pressure sensors for this facility are sufficient time response and flow angle insensitivity. Flow angle sensitivity is

particularly important for downstream measurements where the probes are circumferentially translated through the wakes created by the nozzle guide vanes. To achieve the desired time response, semiconductor strain gauge type pressure transducers, manufactured by Kulite, were used. A disadvantage of these transducers is their tendency to drift with changes in temperature. As a consequence, extensive run-time calibration routines were developed and used during every experiment. To allow a larger range of inlet flow angle to the probe head, either vented Keil type or 15° beveled impact heads were employed. The maximum acceptable flow angles are estimated to be $\pm 27.5^\circ$.

Downstream of the turbine stage, a rake type pressure probe with eight 15° beveled impact heads is employed to survey the pressure in the radial direction. The probe is mounted on the downstream translator to also resolve flow characteristics in the circumferential direction. The pressure transducers (100psig XCQ-063-100) are mounted inside the probe body below the heads. Transducer reference backpressure is provided via a tubing arrangement within the translator. The estimated average uncertainty in total pressure measurement from these heads is 0.25 %. Cai [4] provides more information on the design of this probe.

In addition to this rake, there are differential sensors located upstream of the turbine and in the supply, coolant, and dump tanks. There are also several highly accurate Sensotec (0.05 %) and Heise (0.02 %) pressure sensors mounted throughout the facility for calibration reference. The coolant system is instrumented with lower accuracy (0.1%) Sensotec transducers.

2.5.3 Nozzle Guide Vane Static Pressure Taps

To take static pressure measurements on the hub and tip region of the platform surfaces of the nozzle guide vanes (NGV), one NGV is instrumented with static pressure “taps” on the platform hub and tip surfaces. Four through holes were drilled into each platform surface spaced one-quarter nozzle pitch apart. On the tip end, tubulations are bonded into grooves machined into the outer manifold support of the nozzle cassette. For the hub static tap, stainless steel tubes are bonded onto the top and run through the NGV’s cooling plenum. The outer manifold support of the nozzle cassette was modified

with a feed through hole to allow access to the static tap tubulations. With an access window removed, the tubulations are visible and accessible, as shown in Figure 2.8. Urethane tubing connects to each of four hub and four tip tubulations and is passed through Cajon fittings. The nylon tubing connects to brazed brass tubes (on a brass support piece) which hold the tubes in place and provide a seal with the fitting. Additional urethane tubes connect the brass tubes to a Scanivalve Direct Sensor Array (DSA) 3017 pressure-monitoring device. To maximize frequency response and measurement fidelity the DSA is placed as close to the tubulations as facility construction permits.

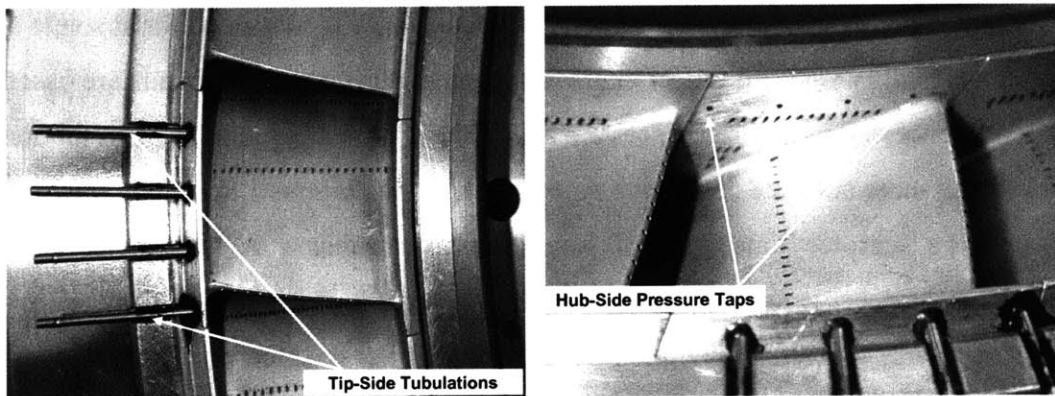


Figure 2.8: Nozzle Guide Vane Static Pressure Taps

2.5.4 Flow Angle Probe

A three hole flow angle probe was developed and fabricated during this research effort at the MIT Blowdown Facility. This instrument was used to determine the angle of the flow leaving the rotor blades of the turbine stage. The design and construction of this instrument will be discussed in detail in subsequent sections.

2.5.5 Other Instrumentation

Various other measurements are taken from the MIT Blowdown Facility with the help of a number of instruments. Digital encoders are used to monitor turbine speed and

translator position independently. The optical shaft encoder consists of two rings of 366 divisions per revolution in quadrature and a once per revolution ring. It is directly mounted to the turbine shaft. Both digital and analog circuitry process the encoder signals to provide shaft position and velocity for storage by the computer data acquisition system.

Two piezoelectric sensors are mounted on the bearing housing to record shaft vibration during an experiment.

The eddy current brake torque meter is instrumented with two load cells that provide a measure of shaft torque. The brake voltage and current are also recorded by the data acquisition system. A list of all instrumentation is provided in Table 2.2.

Facility reference instrumentation provides known conditions for use in the calibration procedures. For these instruments, time response is sacrificed for absolute accuracy and stability since all tunnel temperature and pressure measurements are based on these references. Pressure references are available in the supply tank and test section via slower, but more accurate capacitive type pressure transducers. Located on the supply tank is a Sensotec Super TJE 150 psia (0.05 %) transducer. A Sensotec TJE 50 psia (0.1 %) transducer is located in the critical flow venturi. Recent augmentations to the pressure reference instrumentation have included the use of three very accurate Heise (0.02 %) pressure transducers in the supply, dump, and coolant tanks. These pressure transducers give direct digital readings of the pressures that they measure, thus bypassing the errors associated with other instruments that must pass through the intermediate data collection system. The upstream Pitot probes are referenced to a Setra Model 228 1 psid capacitive type pressure transducer. Temperature calibrations are referenced to a Rosemount Standard Platinum Resistance Thermometer, Model 162N100A (S/N3779), and when possible thermocouples are referenced to Omega TRCIII ice point calibration cells. Efforts are now being made to convert all temperature references, with the exception of those on the downstream translator probes, to the ice point to simplify temperature data reduction.

Table 2.2: Blowdown Turbine Instrumentation

Sensor	Type	Location
Facility Reference		
Heise 2012	50 psia, Heise	Calibration: Dump Tank Run Time: Dump Tank Initial Pressure / Atmosphere
Heise 2013	150 psia, Heise	Calibration: Supply Tank Run Time: Supply Tank Initial Pressure
Heise 2014	500 psia, Heise	Calibration: Coolant Tank Run Time: Coolant Tank Initial Pressure
PFEF300	300 psia, Sensotec: STJE/1835/15 S/N: 589494	Calibration: Coolant Tank / Facility Run Time: Coolant Tank Initial Pressure
PREF150	150 psia, Sensotec: STJE/1833-12-04 S/N: 587965	Calibration: Supply Tank / Facility Run Time: Supply Tank Initial Pressure
PREF050	50 psia, Sensotec: TJE/0713-04TJA-12 S/N: 631656	Calibration: Facility Run Time: Critical Flow Venturi, Test Section Initial Pressure
PREF001	1 psid, Setra: 228-1 S/N:708984	Calibration: Inlet Pitot Tubes
TREF3997	Rosemount Model 162N100A, S/N3779 Standard Platinum Resistance Thermometer	Standard Calibration Reference
TREF10	0-100 °C Platinum RTD	Run Time Reference
Supply Tank		
Heise 2013	150 psia, pressure, Heise	Supply Tank, Internal
PT0A	150 psid, pressure, Kulite	Supply Tank, Internal
PT0B	150 psid, pressure, Kulite	Supply Tank, Internal
TT0A	600 °F temperature, type J T/C	Supply Tank, Internal
TT0B	600 °F temperature, type J T/C	Supply Tank, Internal
TT0C	600 °F temperature, type J T/C	Supply Tank, Internal
Shaft Monitoring		
FTACH	Speed, Digital	Shaft/Bearing Assembly
ATACH	Speed, Analog	Shaft/Bearing Assembly
FBRING	Vibration, forward	Shaft/Bearing Assembly
RBRING	Vibration, rear	Shaft/Bearing Assembly
Eddy Current Brake		
VTOT	Excitation Volt	External
ITOT	Total Current	External
IBRK	Excitation Current	External
ECBF1	Load Cell #1	Internal
ECBF2	Load Cell #2	Internal

Table 2.2: Blowdown Turbine Instrumentation, continued

Sensor	Type	Location
Main Valve		
PVLV	450 psia Kulite	Valve Damping Chamber
XVLV	0-8 in Linear Potentiometer	Valve Slider
Turbine Inlet		
PT2x, (x=A,B,C)	Total Pressure	Main Frame, 120° apart
TT2x, (x=A,B,C)	Total Temperature	Main Frame, 120° apart
PP2x, (x=A,B,C)	Dynamic Pressure	Main Frame, 120° apart
PTYRn, (n=1,2,3,4,5,6)	Total Pressure, 6 head radial rake	Main Frame, fixed location
TTR101-n,(n=1,2,3,4,5,6)	Total Temperature, 6 head radial rake	Main Frame, fixed location
Turbine Outlet		
PFAPn, n=L,C,R	Static Pressure, 3-hole flow angle probe	Downstream Translator
PT45Rn, n=1,2,3,4,5,6,7,8	Total Pressure, 8 head radial rake	Downstream Translator
TTR103-n, n=1,2,3,4,5	Total Temperature, 5 head radial rake	Downstream Translator
RTD103-n, n=1,2	T/C Reference RTD's, 2 locations	Downstream Translator
TTR104-n, n=1,2,3,4	Total Temperature, 4 head radial rake	Downstream Translator
RDT104-n, n=1,2	T/C Reference RTD's, 2 locations	Downstream Translator
P45HUB	50 psid wall static pressure	Downstream Translator Hub
P45A	50 psid wall static pressure	Main Frame Window
Critical Flow Venturi		
PREF050	Static Pressure	Venturi Inlet
PNOZ	Static Pressure	Flow Conditioning Nozzle
TTMFM1	Total Temperature	Venturi Inlet
TTMFM2	Total Temperature	Venturi Inlet
TTNOZ1	Total Temperature	Flow Conditioning Nozzle
TTNOZ2	Total Temperature	Flow Conditioning Nozzle
Dump Tank		
Heise 2012	50 psia, pressure, Heise	Dump Tank
PDMP	Static Pressure	Dump Tank

Table 2.2: Blowdown Turbine Instrumentation, continued

Sensor	Type	Location
Cooling System		
Heise 2014	500 psia, pressure, Heise	Coolant Tank
PREF300	300 psia, Sensotec: STJE/1835/15 S/N: 589494	Coolant Supply Tank
PTC0	300 psia Kulite	Coolant Supply Tank
PTC1	Total Pressure, 300 psig Sensotec	Coolant Supply Manifold
PTC2V	Total Pressure, 100 psig Sensotec	Vane Feed Manifold
PTC2B	Total Pressure, 100 psig Sensotec	Blade Feed Manifold
PCCV	Static Pressure, 100 psig Sensotec	Vane Feed Entrance
PCCC	Static Pressure, 100 psig Sensotec	Tip Casing Entrance
TTC0	Total Temperature	Coolant Tank Exit
TTC1	Total Temperature	Coolant Supply Manifold
TTC2B	Total Temperature	Blade Feed Manifold
TTCBV	Total Temperature	Vane Feed Entrance, B window
TTCBC	Total Temperature	Casing Feed Entrance, B window
TTCV	Total Temperature	Vane Feed Entrance, C window
TCCC	Total Temperature	Casing Feed Entrance, C window

2.6 Pressure Transducer Calibration

A standard calibration procedure is used for the calibration of all differential pressure transducers. The calibration is performed immediately after the supply tank is filled and at the conclusion of each experiment. Calibrating data just before and after each experiment allows transducer drift and scale factor to be quantified. Figure 2.9 shows a typical calibration trace of a differential pressure transducer. This figure and the calibration sequence are described below.

- 1) All transducers are provided a vacuum back-pressure reference by an external vacuum pump. For a post-fill calibration this produces a zero pressure differential across the transducers that are located inside the tunnel, since the tunnel is under vacuum. For those in the supply or coolant tanks, a pressure differential equal to the initial absolute tank pressure is recorded.
- 2) Data is taken at this condition for approximately two minutes as shown by the first segment of the trace in Figure 2.9.
- 3) After two minutes, the back-pressure reference is exposed to atmospheric pressure. Data is acquired for two minutes as shown in Figure 2.9.
- 4) After four minutes, the back-pressure reference is returned to vacuum where it remains for the experiment.
- 5) This procedure is repeated after the blowdown experiment has been completed.

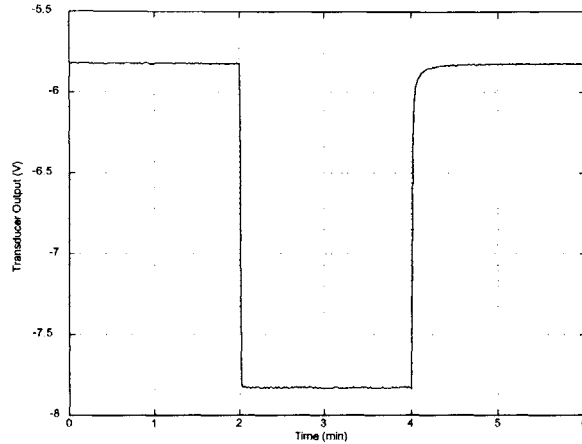


Figure 2.9: Typical Differential Pressure Transducer Calibration Trace

This data provides a voltage change for each differential transducer that corresponds to the local atmospheric pressure. A transducer scale factor can then be computed. Transducer zeros are taken to be the average output prior to the opening of the main valve. The scale and zero can then be used in the data reduction process via the linear calibration relation.

2.7 Data Acquisition

The short duration nature of the blowdown experiment not only places special requirements on instrumentation, but on data acquisition (DAQ) systems as well. The DAQ systems must monitor all instrumented channels at a sampling rate sufficient to capture all time scales of interest for the duration of the experiment. For aerodynamic performance measurements, 1 kHz data sampling is sufficient to resolve the necessary time scales. The required DAQ envelope typically spans 2-4 s in order to record useful data and monitor tunnel ‘spin-down.’ The precise clocking sequence can be modified to capture the desired window. In addition, the post-test calibration provides further insight into the post-test tunnel state.

The current DAQ system consists of three computers. The low-speed system used to monitor and record data from the majority of the instrumentation employs two

National Instruments NI 6031E 16-bit data acquisition boards each with 64 channels in a Dell OptiPlex Pentium® III computer, which is programmed with LabView lab automation software. The 16-bit system is capable of monitoring up to 128 instrumentation channels, sampling at 1 kHz.

An IBM ThinkPad® 386CD laptop computer collects NGV static pressure tap data from the Scannivalve DSA 3017 system. This computer interfaces with the DSA pressure measurement system via a PCMCIA card and simple Ethernet protocol. The operating parameters of the DSA unit can be specified through the laptop interface. Data is also passed to and saved on the computer.

A third computer is used to interface with the three Heise pressure transducers used with the facility. An IBM ThinkPad® 720ED laptop computer is programmed with LabView software that allows each pressure transducer to be sampled at 4 Hz. This low-speed data is used to monitor tunnel reference conditions, which can be used for calibrations. Table 2.3 summarizes the Blowdown Turbine Facility DAQ equipment.

Table 2.3: Blowdown Turbine Facility Data Acquisition System

Specification	Dell OptiPlex Pentium® III	IBM ThinkPad® 386CD	IBM ThinkPad® 720ED
Speed	Low	Low	Low
Operating System	MS Windows 98	MS Windows 95	MS Windows 98
DAQ Platform	LabView	DSALink 2	LabView
DAQ Board	NI 6031E		
Resolution	16 bit		
Board Channels	64	16	3
Number of Boards	2	1	1
Total Channels	128	16	3
Sampling Rate	1 kHz	200 Hz	4 Hz

2.8 Summary

This section has discussed the MIT Blowdown Turbine short duration experimental facility used to acquire turbine stage data for calculation of adiabatic efficiency. As well as a summary of the major components of the facility, run-time preparations including the determination of blowdown operating conditions required to achieve full-scale turbine similarity have been discussed. Total temperature and pressure

instrumentation for highly accurate flow field measurements was briefly discussed along with other instrumentation used to characterize turbine performance. This was followed by a description of the standard differential pressure transducer calibration procedure. Also included in this section was information regarding the Blowdown Turbine Facility data acquisition system.

Chapter 3: Heat Flux Gauges

3.1 Introduction

The development of heat transfer gauges capable of measuring the heat flux to turbine blades was an important part of recent research at the MIT Blowdown Turbine Facility. The availability of accurate data of this sort is very valuable to those who wish to improve upon the performance of gas turbine engines. Included herein is a description of the development and fabrication of heat flux gauges intended for use with rotating components in a Blowdown Facility.

Any heat transfer gauge produced for use in the MIT Blowdown Turbine Facility or any other short-duration research facility must be capable of simultaneously measuring steady state and time resolved heat flux to a turbine rotor blade. To this end, certain design requirements were necessary. Such an instrument must:

- 1) Be capable of operating in the test environment (450 K gas temperature, 400 K blade metal temperature)
- 2) Be small enough in size that several gauges can be placed on a single airfoil in order to spatially resolve heat transfer on the blade surface
- 3) Provide minimal disruption to the flow and heat transfer processes on a rotor blade
- 4) Be able to be implemented with minimal modification to the turbine blades
- 5) Be independent of the heat conduction distribution within the blade body
- 6) Be capable of operating under the high centrifugal accelerations experienced by rotating components
- 7) Have a frequency response from DC to five times blade passing frequency
- 8) Be relatively simple, economical, and safe to manufacture

Two candidate techniques for fulfilling these requirements were considered based on recent work to measure heat transfer at the MIT Blowdown Facility. Both semi-infinite heat flux gauges and multi-layer, thin-film heat flux gauges have been researched and employed for this purpose in the past.

The former involves mounting a thin-film resistance thermometer on an insulating substrate. Van Poppel [28] further developed previously employed techniques [11] of using platinum paint on machineable ceramic (MACOR) in order to construct heat transfer gauges for use in an instrumented tip casing insert. One very attractive feature of such gauges is the ease with which they can be manufactured with in-house resources. In addition, when these gauges are employed in an array of rows and columns for spatial heat flux resolution, defective gauges can be individually removed and replaced. Although very successful, this technique of heat flux measurement could not be as easily modified for use on the surface of turbine blades. These MACOR gauges are such that they would need to be recessed into the surface for which heat transfer measurements are desired. Due to physical design constraints, this would not be possible with a film-cooled turbine rotor blade. Adaptations such as the fabrication of ceramic turbine blades, or the coating of existing metal blades with a suitable insulator would require far too complex and costly.

Multi-layer, thin-film heat flux gauges were first investigated for use with the MIT Blowdown Facility by Guenette [8], and have been used to successfully instrument both tip casing inserts and rotor blades. These multi-layer heat flux gauges are comprised of two metallic temperature sensors on either side of a thin insulating substrate. The gauge is bonded directly to the surface under investigation. Previously instrumented Blowdown Facility components have employed thin nickel temperature sensors on either side of a 25 μm polyimide (Kapton[®]-DuPont commercial designation) insulating film, which can be bonded to a metal surface using standard strain gauge glue. As a result, no modifications are necessary in order to implement these heat transfer gauges on a turbine rotor blade. By design, such gauges do not pose a large disturbance to the normal flow conditions in the turbine. Previous research has demonstrated a frequency response of almost 60 kHz, surpassing the current requirements. Below a certain frequency, normally less than 20 Hz, these gauges operate in a direct mode in which the heat flux is

determined by a measure of the temperature difference across an insulator. At higher frequencies, normally above 1.5 kHz, the heat flux is deduced using only the upper temperature measurement coupled with a one-dimensional semi-infinite heat conduction model. Despite all of these advantages, the use of these gauges has been somewhat limited recently due to the difficulty associated with their fabrication. Variations to previously employed fabrication methods were required in order to render a gauge manufacturing process that was sufficiently reliable to incorporate into research activities. One of the key goals of this research effort was to seek improvements in fabrication techniques of these multi-layer, thin-film heat transfer gauges.

3.2 Multi-Layer, Thin-Film Heat Flux Gauges

A multi-layer, thin-film heat transfer gauge consists of two thin-film temperature sensors on either side of an insulating substrate. However, there are several design criteria that need to be decided upon during the development and fabrication, including physical design and material selection. In order to address these points and justify design choices, Guenette [8] employed a multi-layer, time dependent, mathematical conduction model. This model can provide exact solutions of internal thermal response to a known external heat load in both modes of gauge operation. The model also proved very useful for gauge calibration and data reduction. As a prelude to gauge design, a summary of the pertinent points of this model is included in the following sections.

3.2.1 Multi-Layer, Time Dependent Heat Conduction Model

When employed to measure the heat flux to the test surface, a metal blade in our case, the multi-layer, thin-film heat transfer gauge becomes part of a five-layered system as shown in Figure 3.1.

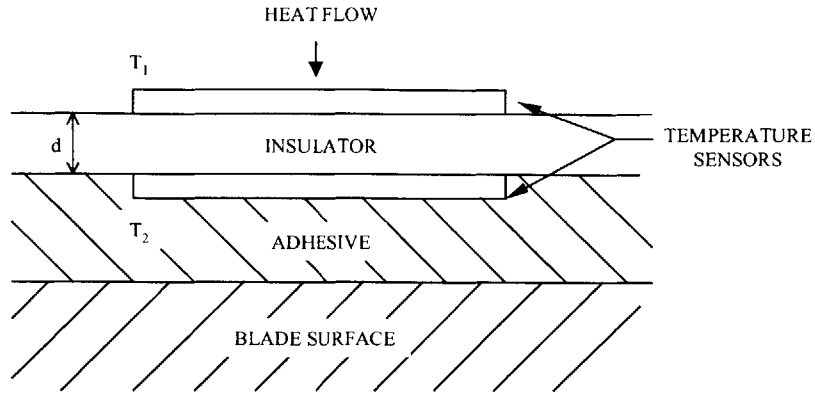


Figure 3.1: Schematic Cross-Section of Multi-Layer, Thin-Film Heat Transfer Gauges

The five layers include an upper thin-film temperature sensor, the insulating substrate of thickness d , a lower thin-film temperature sensor, the adhesive layer, and the blade surface under examination. Under the model used, these five layers were simplified to two layers in order to make for a much less complicated and more practical mathematical interpretation. This was done by assuming the thin-film temperature sensors to be thermally transparent, as well as being negligible sources of heat when excited. The assumption that the adhesive and insulating substrate layers had similar thermal properties was also applied. This assumption is actually extended to any surface layer, such as dirt on the gauge, which may exist. Thus, as illustrated in Figure 3.2, Layer 1 consists of the surface coating, insulating substrate, and adhesive, of total thickness L , and Layer 2 consists of simply the blade.

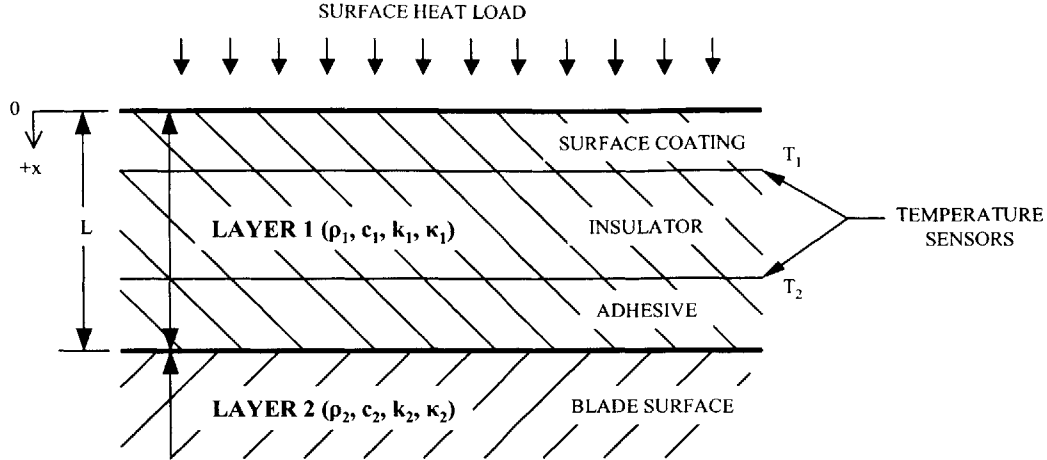


Figure 3.2: Schematic Representation of Simplified Two-Layer Gauge Model

In order to determine the temperature distribution in the two layers, heat conduction equations were solved with the following assumptions and criteria:

- 1) Spatially uniform surface input heat flux, $q(t)$
- 2) Semi-infinite medium of infinite lateral extent (one-dimensional heat flow)
- 3) Uniform thermal properties within each layer
- 4) Layers make perfect thermal contact

As a result, the equations governing the temperature distribution in Layers 1 and 2, respectively, are

$$\frac{\partial T_1}{\partial t} = \kappa_1 \frac{\partial^2 T_1}{\partial x^2} \quad 0 \leq x \leq L \quad (3.1)$$

$$\frac{\partial T_2}{\partial t} = \kappa_2 \frac{\partial^2 T_2}{\partial x^2} \quad L \leq x \leq \infty \quad (3.2)$$

where κ is the thermal diffusivity of a particular layer in the model. The boundary condition that exists at the surface of Layer 1 is

$$k_1 \left. \frac{\partial T_1}{\partial x} \right|_{x=0} = q(t) \quad (3.3)$$

where k is the thermal conductivity of a particular layer in the model. The conditions that exist at the interface between the two layers are

$$T_1(L, t) = T_2(L, t) \quad (3.4a)$$

$$k_1 \left. \frac{\partial T_1}{\partial x} \right|_{x=L} = k_2 \left. \frac{\partial T_2}{\partial x} \right|_{x=L} \quad -\infty < t < +\infty \quad (3.4b)$$

In addition, the semi-infinite boundary condition must be included,

$$T_2(\infty, t) = 0 \quad (3.5)$$

The initial condition that applies over the entire length of the layered model is

$$T(x, 0) = \text{constant} = 0 \quad 0 \leq x \leq \infty \quad (3.6)$$

Setting the surface boundary condition and the initial conditions given by Equation (3.3) and Equation (3.6), respectively, will fully define the problem. However, these conditions are dependent on the external driving heat load to be applied to the surface being investigated. The cases involving a steady harmonic variation in surface heat flux and a step in surface heat flux were considered. For each of these cases, the exact solutions for temperature distribution in Layer 1, $T_1(x, t)$, were included with the development of the model. For the sake of brevity, the solutions themselves will not be included herein. Only the important details drawn from their derivation that pertain to gauge design will be discussed below. For a rigorous derivation of intermediate steps, one should consult the work of Guenette [8].

3.2.2 Gauge Model Discussion

As noted earlier, there are two limiting modes of operation (low-frequency and high-frequency) for multi-layer, thin-film heat flux gauges while measuring heat transfer rates. In the direct mode, the heat flux applied to the surface of the gauge is assumed proportional to the temperature difference across the gauge. Previous work involving a steady harmonic variation in heat load to a gauge operating in the direct mode showed that the temperature rise with surface heat flux, also known as the gauge sensitivity, can be approximated by

$$\frac{\Delta T}{q} = \frac{d}{k} \quad (3.7)$$

This is applicable below a characteristic sensor cutoff frequency, ω_c , of the applied heat flux described by

$$\omega_c = \frac{\kappa}{2d^2} = \frac{1}{2} \left(\frac{(k/d)}{\sqrt{\rho ck}} \right)^2 \quad (3.8)$$

Equations (3.7) and (3.8) can be combined to obtain a relationship between gauge sensitivity, $\Delta T/q$, and response frequency bandwidth, f_c ,

$$\frac{\Delta T}{q} f_c^{1/2} = \frac{1}{2\sqrt{\pi}} \frac{1}{\sqrt{\rho ck}} \quad (3.9)$$

The response bandwidth is simply the cutoff frequency, or the frequency below which the gauge is said to operate in the direct mode, expressed in Hertz. From Equation (3.9), it is clear that the product of the gauge sensitivity and the cutoff frequency is inversely proportional to the thermal property $\sqrt{\rho ck}$ of the insulating substrate to which the thermal sensors are mounted. Certain points regarding material selection should be

drawn from this. These equations show that a low thermal inertia ρc , good for maximizing f_c , as well as low thermal conductivity k , good for high $\Delta T/q$, are desirable gauge substrate properties. Once material thermal properties $\sqrt{\rho ck}$ have been selected, the choice of the substrate thickness, d , will determine the trade-off between gauge sensitivity and cutoff frequency.

The direct mode of operation as outlined above is only valid for uniform temperature gradients across the gauge. However, this is not always the case. The second mode of operation of the multi-layer, thin-film heat flux gauges is the semi-infinite mode. This case arises when the thermal penetration depth is smaller than the thickness of the gauge itself. In that event, the insulating substrate layer of the gauge essentially damps frequency components of the applied heat load. Since the thermal penetration depth is such that changes in the surface heat load do not reach the lower temperature sensor, the heat flux must be inferred from the upper thin-film temperature sensor. Previous analysis of this model showed that the lower temperature sensor would be completely damped for input frequencies above $100\omega_c$ for a steady harmonic heat load input, resulting in semi-infinite mode operation. The upper surface temperature of the gauge in such a scenario was given to be

$$T(0,t) = \frac{q_o}{\sqrt{\rho ck}} \omega^{-1/2} \sin\left(\omega t - \pi/4\right) \quad (3.10)$$

As was the case with the direct mode of operation, the high-frequency temperature sensitivity improves with low $\sqrt{\rho ck}$ of the insulating substrate. Additionally, it can be seen from the above that for a specific value of gauge sensitivity, the upper limit of frequency response is increased with lower values of $\sqrt{\rho ck}$.

3.2.3 Substrate Material Selection

The thermal properties discussed above play a significant role in qualifying potential insulating substrate materials for multi-layer, thin-film heat transfer gauges.

Early developmental efforts by Guenette [8] determined that polyimide film had the lowest $\sqrt{\rho c k}$ of a number of materials considered. This yielded the highest practical sensitivity bandwidth combination. The substrate thickness was chosen to be 25 μm , which yields a direct mode cutoff frequency of 20 Hz and a semi-infinite mode lower response limit of 1.5 kHz. The same substrate thickness was employed for the fabrication of gauges during this research effort. Additional factors involving ease of fabrication and installment were also a consideration regarding the use of the same substrate. Polyimide is known for displaying excellent temperature resistance and retaining mechanical properties up to approximately 600 K. In addition, polyimide displays excellent electrical properties and resistance to chemical attack in comparison to other plastic materials. Many of these properties are a result of the structural form of Kapton[®] polyimide shown below.

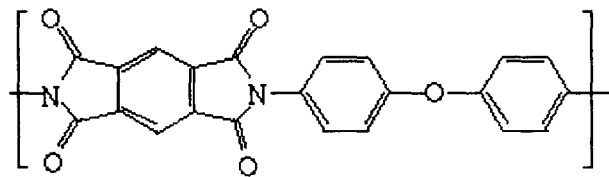


Figure 3.3: Structural Formula of Kapton[®] Polyimide

The nitrogen atoms have a higher electron density than the carbonyl groups and the resulting transfer of charge causes adjacent molecules to bond to each other forming polymer chains. Similar intermolecular bonds can also exist between individual chains causing them to stack on top of each other in cross-linking reactions. This cross-linking occurs between nitrogen and carbonyl components from adjacent chains. These intermolecular forces are sometimes referred to as van der Waals forces and result in improved material properties [26].

3.3 Temperature Sensors

Multi-layer, thin-film heat flux gauges employ two film resistance thermometers to measure the temperature on either side of the insulating substrate layer. These resistance thermometers are thin layers of a material that experiences a resistance change with a change in temperature. Important design characteristics pertaining to resistance thermometers that were the focus of previous research, Guenette [8], include the material chosen as well as the physical design of the sensor itself. Some of the details regarding the design of these temperature sensors are noteworthy.

As mentioned, temperature sensors rely on a change in resistance with changes in temperature. The temperature coefficient of resistivity, $\alpha(T)$, which is itself a function of temperature, quantifies the dependence of resistance on temperature. However, metals normally chosen for use in such applications have temperature coefficients of resistivity that do not significantly vary with temperature, so the change in resistance with temperature can be expressed by

$$\Delta R = R\alpha\Delta T \quad (3.11)$$

The actual measurement made with these sensors when in operation is a voltage drop, expressed by

$$\Delta V = V\alpha\Delta T \quad (3.12)$$

The sensitivity of the resistance thermometers can be defined as the drop in voltage across the sensor over the change in temperature,

$$\frac{\Delta V}{\Delta T} = V\alpha \quad (3.13)$$

From Equation (3.13), it is clear that the sensitivity of the temperature sensors in the heat flux gauge is directly proportional to the excitation voltage, V , and the temperature

coefficient of resistivity, α . The excitation voltage must be limited based on the amount of heat dissipated by the sensor, q_d ,

$$q_d = \frac{V^2}{Rlw} \quad (3.14)$$

where l and w are the length and width of the film sensor, respectively, and the film resistance, R , can also be expressed in terms of the geometry of the sensor,

$$R = \frac{\rho l}{wt} \quad (3.15)$$

where t is the thickness of the film sensor sitting above the substrate layer, and ρ is the resistivity of the material used as the resistance thermometer. By combining Equations (3.14) and (3.15) with Equation (3.13), important criteria regarding the physical design of the active film sensor can be obtained,

$$\frac{\Delta V}{\Delta T} = \left(\frac{\rho}{t} \right)^{1/2} \alpha l q_d^{1/2} \quad (3.16)$$

Equation (3.16) can be examined to see what sensor properties would maximize temperature measurement sensitivity. Clearly, a long, thin sensor would be the best physical design. Note that the sensor width does not appear in the above equation. Thus, sensor geometry should be chosen to maximize the overall length of the active sensor. The most significant constraint on this length would be the area available for the sensor, based on the number of gauges required on a single rotor blade for spatial heat flux resolution. A long, thin, and narrow serpentine pattern was chosen in an effort to maximize measurement sensitivity. The requirement for a narrow (small w) sensor piece was due to the limited area that the serpentine pattern could occupy, rather than any effect of the sensor width on sensitivity. The details of the actual design and fabrication of the serpentine pattern used for the sensors will be elaborated upon in later sections.

Equation (3.16) also exposes $\alpha\sqrt{\rho}$ as a material parameter that can be increased to maximize the sensitivity of resistance thermometers. Previously compiled bulk material properties were used to assure that the selected sensor material was justified. This data is included below.

Table 3.1: Bulk Material Properties of Various Film Thermometer Materials [6]

Metal	Resistivity, ρ , ($\mu\Omega$ cm)	Temperature Coefficient of Resistivity, α $\times 10^3$, ($^{\circ}\text{C}^{-1}$)	Sensitivity, $\alpha\rho^{1/2} \times 10^3$, ($\mu\Omega^{1/2}\text{cm}^{1/2}\text{C}^{-1}$)	Rank
Zirconium	40.0	4.4	27.8	1
Iron	9.71	6.51	20.2	2
Nickel	6.84	6.9	18.0	3
Tin	11.0	4.7	15.5	4
Tantalum	12.45	3.83	13.5	5
Platinum	10.6	3.927	12.7	6
Gold	2.24	8.3	12.4	7
Palladium	10.54	3.74	12.1	8
Cadmium	6.83	4.2	10.9	9
Chromium	12.9	3.0	10.7	10
Zinc	5.916	4.19	10.1	11
Copper	1.678	6.8	8.8	12
Aluminum	2.6548	4.29	6.9	13

From the above list, nickel was selected as the material for the film temperature sensors. Nickel clearly has very good intrinsic properties for temperature measurement sensitivity. Nickel was also chosen because of its proven performance in thin film chemical deposition processes and applications using polyimide film [8].

3.4 Gauge Fabrication

The remaining obstacle in successfully producing multi-layer, thin-film heat transfer gauges was to develop new fabrication techniques that would facilitate relatively simple and reliable construction based on knowledge gathered from the gauge model. The fabrication techniques were chosen such that they were compatible with the design choices of substrate material, sensor material, and sensor geometry. Guenette [8] employed sputtering and lift-off photolithography practices to produce similar heat flux gauges. These methods were not very reliable, often resulting in very low yield rates of

successfully finished gauges. An effort was made to experiment with new methods of bonding nickel to the polyimide substrate and of creating the intricate film sensor structure desired based on gauge theory. The following sections give a detailed description of the techniques developed to accomplish each of the required steps in gauge fabrication.

3.4.1 Nickel Deposition on Insulating Substrate

The first step in fabricating multi-layer, thin-film heat flux gauges involves bonding a layer of pure nickel onto either side of the substrate (25 μm thick polyimide film in this case). The method of deposition by sputtering under pressure that was previously used was not considered due to documented difficulties with high batch to batch variations in surface coating and the apparent presence of high residual stresses, which cause cracks in the nickel layers. In an effort to resolve these problems, Guenette carried out a follow-on investigation involving electroless physical-chemical deposition of nickel on polyimide film. Unfortunately, this work was not documented in detail, but it did serve as the basis for the methods developed and used here. The electroless deposition of nickel on polyimide film consists of two broad sub-processes. These involve cleaning the substrate samples, and then the actual plating of nickel onto the substrate. The final procedure for each of these sub-processes was a result of several iterations and adaptations to the basic methods recorded in previous work. Many of these adaptations were a result of trial and error investigation aimed at eliminating various difficulties encountered.

3.4.1.1 Cleaning of Substrate Material

The polyimide film must first be properly cleaned in preparation for the subsequent plating process. The detailed procedure of the cleaning process can be found in Appendix A. A piece of 25 μm thick polyimide film, approximately 7.5 in. long and 5.5 in. wide, was mounted in a plexiglass frame prior to being cleaned.

In order for the signals from the bottom side temperature sensor to be read once the gauge is glued in place, small puncture holes were made in the substrate piece prior to cleaning and plating. These holes were made by hand using a very fine scalpel blade. In order to align the holes with the sensor leads, the plexiglass frame was mounted over a metal base jig that had the positions of the through holes marked. A total of 16 gauges were made on a single piece of substrate and, thus, 32 holes were required. The same metal block later served as the base unit for aligning the plated substrate ready for the sensor geometry to be fashioned.

Once the through-holes had been made, the procedure for cleaning the sample was carried out. Several chemicals were required for the cleaning process. A list of the chemicals, as well as their compositions is also included in Appendix A. The cleaning process consists of several wash cycles using a concentrated cleaner/conditioner solution followed by a distilled water rinse. The Shipley Cleaner/Conditioner 1110A solution is an acidic soak cleaner that is intended to remove oils and other contaminants, and to condition the substrate to ensure complete metallic coverage during the electroless plating procedure to follow [22]. Gentle agitation of the cleaner solution was employed to avoid the concentration of foreign matter or soils. Another important step in the cleaning process was a soak in a potassium hydroxide, KOH, and ethanol wet-chemical etching solution. Etching of the substrate is a very important step in the pre-treatment cleaning process. The goal of the etching is to destroy some of the intermolecular forces that attract separate polymer chains to one and other. These intermolecular forces, also known as van der Waals forces, are much weaker than the chemical bonds existing within the individual polymer molecules. As a result, the etch will only destroy the cross-linkages that exist between the macromolecular polymer chains, and not the intramolecular bonds within the chains. Some literature states that the pre-treatment of polyimide films for electroless metal plating does not actually cause surface roughening, but rather it results in preparation of the surface for chemical forces to be invoked. Unlike with other plastic materials such as acrylonitrile butadiene styrene (ABS), metal adhesion to polyimide is a result of chemical forces rather than mechanical adhesion effects [26]. The choice of an etchant is driven by the properties of the substrate. As stated earlier, polyimides are known for their excellent resistance to chemical attack.

However, polyimide materials will soften when subject to attack by strong alkalis. Potassium is an extremely fast-diffusing alkali metal ion and is thus used as the basis of etching solution for polyimide. Alkali metal hydroxides, like KOH, can be combined with organic solvents, ethanol for these purposes, to form the etch solution. Care must be exercised in handling these solutions due to their corrosive nature. An oven drying at low temperature was used to ensure that no impurities would accumulate on the wet samples following the cleaning process.

During the development of the procedure for cleaning the substrate several difficulties were encountered, some of which are worthy of note. In early experimentation involving the KOH etch solution, a white film appeared on some samples of the polyimide film. Several stock rolls of DuPont's Kapton[®] polyimide were being used for the substrate. Investigation revealed that two different types of Dupont polyimide film were unknowingly being used. Kapton[®] Type HN film is an aromatic polyimide, one containing a benzene ring, whose structure is shown in Figure 3.3. Type HN film is well suited for use with KOH etch solution, producing no undesirable side effects when the proper procedure is employed. The other stock roll of Kapton[®] polyimide film was Type FN film, which is actually a composite polymer material combining Type HN polyimide with tetrafluoroethylene (Teflon[®]-DuPont commercial designation) [7]. When used in the etching process, the existence of the Teflon[®] caused a white precipitate to contaminate the etch solution. Care was subsequently taken to ensure that only Type HN polyimide film was used to avoid this problem. The choice to implement the use of a plexiglass frame to hold the substrate during the cleaning process was also a result of experimental difficulties. Without the frame, the substrate would fold onto itself during the running water rinse steps involving the use of a hose. This would not allow for the samples to be completely cleaned free of chemicals and contaminants. The frame also made the addition of through-holes much easier.

3.4.1.2 Electroless Nickel Plating

Following the initial cleaning of the polyimide substrate pieces, additional pre-treatment and subsequent nickel plating steps were required. A detailed procedure and

chemical composition list for the electroless plating process are also included in Appendix A. For this process, the samples were removed from the plexiglass frame used during cleaning, and cut into to separate pieces that contained 16 gauges each. Each cleaned sample would thus yield two pieces to be plated separately. Having the polyimide pieces not confined by the plexiglass frame provided much better plating results. However, as a result, no running water rinse steps were included during the plating process. Static bath rinses were employed exclusively here.

Prior to the actual plating step, pre-conditioning of the samples was required. Etched plastics are electrical insulators and are not immediately compatible with electroless nickel deposition. In order to rectify this problem, the surface of the plastic substrate must first be activated with the application of catalyst nuclei, which are most often noble metals, such as palladium. The electroless deposition of metal will initiate on these metal particles that have been introduced to the surface of the substrate [17]. Shipley Catalyst 9F solution is a palladium-based catalyst that seeds the non-conductive plastic surfaces with catalytic nuclei. Following exposure to the catalyst, the substrate has been activated, whereby the small catalyst particles help ensure the initiation of the metal deposition, as well as a uniform coverage during plating [21]. Following the application of the catalyst, the samples were rinsed and then treated by an accelerator solution. Shipley Accelerator 19 solution was used to activate the catalyst particles and ensure rapid and uniform coverage of nickel during the subsequent plating step. The accelerator also prevents the catalyst on the substrate surface from later escaping into the plating bath, thus minimizing contamination of the nickel source [20].

Because the substrate used is non-conducting, an electroless metal deposition technique must be employed. More conventional electrochemical plating procedures cannot be used unless an initial conductive metal coating is adhered to the sample surface. Shipley Electroless Nickel PM-980 solution provides for deposition of an adherent conductive coating onto the pre-treated substrate surface. If desired, such a coating can serve as the basis for subsequent electroplating processes [23]. The electrodeposition of metal from solution requires a source of electrons for the reduction of the metal ions in solution to the parent metal at the substrate, which is known as the cathode in such a process. In conventional electrolytic deposition, the electrons are

provided by an external current source. However, electroless deposition does not use an external current, but rather the electrons are produced by a chemical reaction in solution. As a result, electroless metal deposition is also referred to as chemical metal deposition. The electrons needed to discharge the metal ions in solution during such a process are provided by reducing agents in the solution, which themselves are oxidized and thus surrender electrons for use in reactions at the substrate. This basic process can be described by the following electrochemical reactions involving a metal, M, and a reducing agent, R,



The reducing agent must provide exactly z electrons for each metal ion, which is the valence number for that metal. Nickel has a valence of +2, meaning that it requires two electrons to transition from a cation, Ni^{2+} , to a pure metal, Ni. The Shipley PM-980 plating solution is an alkaline bath containing both nickel ions, from a soluble nickel salt, and a reducing agent. These components are in stable equilibrium such that they will not react under storage conditions. The plated layer is not actually pure metal alone, but also includes some derivatives of the reducing agent used. The high solubility of reducing agents in alkaline solution greatly reduces the need for any additional agents in basic plating solutions. Alkaline solutions are also effective and desirable for use in low-temperature electroless plating applications, such as the deposition of metal films on polymeric materials, including polyimide.

The electroless deposition of metal is very closely related to the pH and temperature of the plating bath. These two parameters affect the rate of deposition, and the amount of reducing agent derivatives in the plating layer, which both in turn affect several other coating properties. For this reason, ammonium hydroxide, NH_4OH , was carefully added as a buffer to control the pH of the plating solution, and the temperature of the plating solution was maintained at the appropriate level. Experimental trials revealed that these two factors can indeed have significant negative influences on the

finished product if not closely controlled. The pH of the PM-980 solution was maintained in the range of 8.3-8.4, and the temperature was kept at 25 °C.

The reduction and deposition of metal ions will only initially occur on a catalytically active surface, hence the cleaning and pre-treatment processes. Once the initial plating takes place onto the palladium catalytic metal, further deposition can still continue because the nickel itself is a catalyst for the electroless process. This is the mechanism that allows for a variable layer thickness of nickel, depending on the length of time that samples are left in the plating bath. The layer of nickel deposited to either side of the substrate via the procedure used with these gauges is on the order of 0.1 μm . Because the electroless plating solution is the source of the components consumed during deposition, it is important to ensure that these chemicals are replenished to maintain the quality of the plated product. The PM-980 solution was replaced with a freshly made plating bath on a regular basis [17].

Experimental efforts concerning the electroless plating of nickel onto polyimide film resulted in some important observations that were taken into consideration in the final procedure for this process. Frequently during early plating processes, large variations in plating finishes would result from identical plating procedures and techniques. It was concluded that these batch to batch variations were merely a result of cleanliness and contamination issues throughout the process. This underscores the importance of delicate and sterile handling and techniques throughout cleaning, pre-treatment, and plating processes. Certain additional steps were taken to mitigate contamination of the substrate samples. Process results were on average much more successful when a fresh Cleaner/Conditioner 1110A solution was used. As a result, a new cleaner solution was prepared each day that the cleaning process was performed. Another source of contamination was the transfer of some chemicals into others throughout the process. The Catalyst 9F solution was particularly notorious for this, as some of the chemical tended to remain pooled behind the tweezers used to hold the polyimide film in the chemical baths, even following two static rinses. To avoid this problem, the position of the tweezers was changed between the first and second static rinse baths. This worked well to eliminate any excess Catalyst 9F that might otherwise affect subsequent plating. A point that must be stressed is that general substrate and

reagent cleanliness and care proved paramount to the success of this electroless metal deposition scheme.

3.4.2 Implementing Gauge Geometry and Detail

Once a uniform layer of nickel was deposited on the polyimide samples, a method to selectively remove the nickel from the substrate sheet was required. A technique was sought that would:

- 1) Be capable of removing nickel from a single side of the polyimide film without affecting the film itself or the nickel plating on the reverse side
- 2) Be capable of shaping gauge sensor geometry with a spatial resolution on the order of several thousandths of an inch
- 3) Be capable of aligning multiple sets of gauge sensors and conductive leads on both sides very accurately with one and other, and with plated through holes on the substrate
- 4) Impose as little contamination and physical stress risks to the sample pieces as possible
- 5) Be very reliable and easily repeatable

A photomachining process using a 248 nm krypton fluoride, KrF, excimer laser system was selected for use in forming the gauge active sensors and leads.¹ Ablation using this laser can be limited to a depth of approximately 1 μm , depending on the material being removed, so single-sided patterning without deterioration of polyimide did not pose a concern. Such a device is capable of consistently resolving line widths of approximately 25 μm , which was a consideration in final gauge sensor design. The heat flux gauges had to be fashioned in two separate steps using the excimer laser. The fine details of the sensor head itself required the fabrication and use of a mask, and the remaining leads were machined using an automated moving table. The capabilities of this system along with gauge design criteria were factors influencing the final design of

¹ A commercial vendor with such a system was located, Photomachining Incorporated, Pelham, NH, USA.

the heat flux gauges. Consistent with Equation (3.16), a long, thin, and narrow band of nickel in the shape of a square serpentine gauge sensor pattern was chosen. An identical sensor pattern was used for both the top and bottom side of the heat flux gauge. A detailed view of the sensor pattern used is shown below in Figure 3.4.

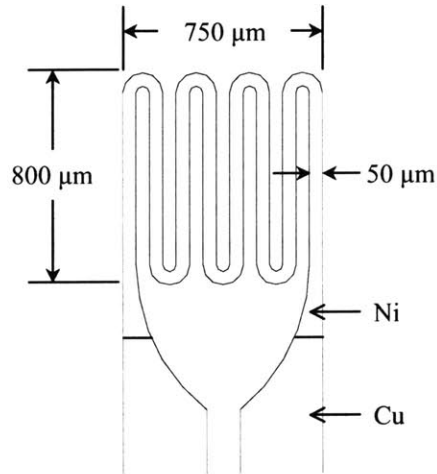


Figure 3.4: Detailed Schematic of Gauge Sensor Geometry

Conductive leads were also required in order to read the signals measured by these sensor heads. Because the signals would only be taken from the top side of the gauge for both top and bottom sensors, a different configuration for the leads was required for each side of the gauges. Figure 3.5 shows a view of an entire single top and bottom side gauge.

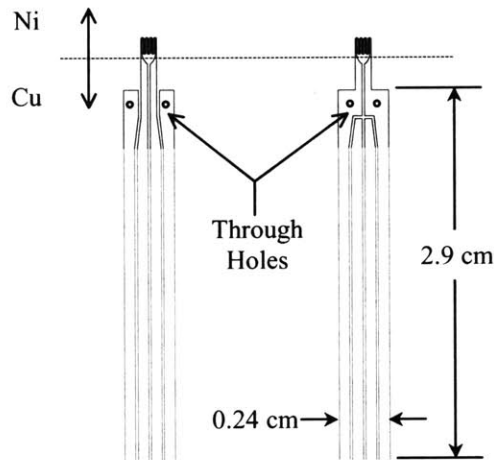


Figure 3.5: Schematic of Top (left) and Bottom (right) Side of a Single Heat Flux Gauge

The fabrication scheme developed was intended to produce a total of sixteen two-sided heat transfer gauges, like the individual gauges shown above, on each sample piece of the substrate material.

The procedure to process these sheets of gauges using the excimer laser required a considerable amount of care and attention to detail. One key point is that the patterns on the two separate sides of the sheets needed to lie directly over one and other. This was essential to ensuring accurate heat transfer measurements for all modes of operation. A mask with a pair of sensors having the sensor geometry was commercially fabricated in order to easily ablate several sensor heads on each substrate sample. To ensure that the through holes would lie in the centre of the proper lead, the sensors were machined with reference to the pre-cut holes in the polyimide samples. In order to ensure that the patterns on the bottom of the gauge would overlap on those on the top, a two-piece aluminum frame and block was used. The block was aligned with and bolted to the movable machining table, and polyimide samples were placed in a frame that could sit top-side up or down on this block. This apparatus allowed any feature on a substrate sample to be located and used as a physical reference feature, regardless of which side of the heat transfer gauge was being machined, allowing successful overlapping of gauge patterns.

3.4.3 Electrolytic Copper Plating of Gauge Leads

Because heat transfer gauges used in these applications are intended to measure the heat flux to relatively small areas, it is beneficial to isolate the active sensor head as the only portion of the gauge that will undergo a large change in resistance with changes in temperature. Thus, the gauge leads must not be allowed to significantly contribute to the measured resistance, or change in resistance, of the heat flux gauges. Equation (3.16) describes temperature measurement sensitivity to a specific input heat load as a function of geometry and material properties. The geometry of the gauge leads is fixed in order to have a certain number of gauges fit on a single polyimide sheet. However, modification of the material property $\alpha\sqrt{\rho}$ can be used to alter the sensitivity of certain portions of the heat transfer gauges. From Table 3.1 it can be seen that copper has a very low

sensitivity parameter, $\alpha\sqrt{\rho}$, compared to other materials examined. Because the nickel-plated polyimide film is a conducting surface, more conventional electrolytic copper plating techniques could be employed to create the desired low resistance leads.

Unlike electroless metal deposition, electroplating uses electrons from by an externally driven current to provide for the reduction of metal ions, which was described by Equation (3.18). The process of electrolysis is most often carried out in a water solution, or bath, of salts and ions. Copper pyrophosphate plating solutions are commonly used in industry for the deposition of copper on circuitry with through holes. Such a bath is desirable for applications involving plastics with a conductive surface, including nickel-plated polyimide, due to its non-corrosive and non-toxic nature [13]. The complete procedure used in the electrolytic plating of copper onto machined heat flux gauges is included in Appendix A. Lowenheim [13] suggests bath composition and operating conditions for such a process. A solution of 30 g/L copper (II) sulphate pentahydrate, $\text{CuSO}_4 \cdot 5\text{H}_2\text{O}$, 120 g/L sodium pyrophosphate decahydrate, $\text{Na}_4\text{P}_2\text{O}_7 \cdot 10\text{H}_2\text{O}$, and 36 g/L disodium hydrogen phosphate, Na_2HPO_4 , was used for plating. A simple copper anode was used with this solution. An anode to cathode area ratio of 1.5 was used. After some experimentation and consultations with Sadoway [18], successful plating was consistently achieved with a cathode current density of 15 mA/in.^2 applied for a time of 220 s using an external DC power source. Gentle agitation of the plating solution was also implemented in an attempt to replenish ions in the vicinity of the cathode. Symmetrical dispersion of the anodes was also used to help provide both sides of the nickel-plated substrate with metal ions for reduction. Once the copper coating was in place, heat flux gauges produced by this method consistently displayed resistance values of approximately 1000Ω .

One important step during the development of the copper plating process involved determining a technique to isolate the active sensor serpentine to prevent them from being plated. A method to physically cover the sensor serpentine while in the plating bath, thus electrically isolating them, was required. However, any treatment would have to be easily reversed without harming the delicate sensor structure. Removal of this protective covering would have to involve as little physical manipulation as possible. The use of liquid photoresist was selected for this operation. Shipley 1805 Photoresist

could be strategically and delicately applied to the machined substrate piece to ensure selective copper plating. Once oven baked at low temperature, the resist was resistant to the electrolytic solution, but could be very easily removed by a gentle ethanol rinse.

Many modifications to the copper electroplating process were made during experimental development. Significant difficulty was experienced in producing an even, flawless, and adhesive copper coating on the nickel deposit. These difficulties were rectified by performing experiments using variable current densities and plating times. Sadoway [18] suggested that peeling of the copper plating was due to residual stresses arising during the process. Plating at lower current densities, for long plating times, was used to combat this. Physical deformation, or bending, of the samples during plating were also a sign of these residual stresses. Mechanical agitation and dispersion of the anodes were other techniques employed to help avoid this problem.

3.5 Summary

New practices to fabricate multi-layer, thin-film, heat flux gauges have been developed. The fabrication employs electroless nickel deposition, photomachining using an excimer laser, and electrolytic copper plating. These methods are an improvement on those previously used to produce similar gauges. The gauges and the techniques used to produce them were designed based on gauge model theory presented and discussed in the previous sections. Following calibration and mounting on rotor blade surfaces, these gauges are ready for use in the MIT Blowdown Turbine Facility.

Chapter 4: Flow Angle Probe

4.1 Introduction

The measurement of flow characteristics is extremely valuable to any turbomachinery research effort. A significant portion of recent research work at the MIT Blowdown Facility was focused on obtaining an accurate assessment of the pitchwise flow angle downstream of the turbine rotor. The difficulty in accurately modeling flows in such devices emphasizes the value of these types of experimental investigations. The measurement of flow angle was accomplished with the design, development, fabrication, calibration, and implementation of a three-hole, hemispherical-nose, multi pressure sensor, flow angle probe (FAP). The following sections describe the process by which the FAP was developed and incorporated into the current test facility.

4.2 Flow Angle Probe Design

The complexity associated with the quantitative experimental measurement of fluid flow characteristics requires that significant thought be put into the design of any instrumentation. Design of instrumentation for these purposes will be influenced by several factors including spatial resolution, temperature sensitivity, ease of introduction to casing, and desired frequency response to name a few. Due to the large number of factors that influence probe design, each unique instrument will also require a calibration before being implemented for its intended use. It was determined that a multi-port pressure probe intended for use in measuring flow angle downstream of the rotor must:

- 1) Offer minimal disturbance to the natural flow patterns in the test stage

- 2) Be robust enough to operate accurately in the test environment
- 3) Have sufficiently rapid response to resolve certain unsteady characteristics
- 4) Make all measurements close to a single point to enable spatial resolution in the flow field
- 5) Be compatible with the existing facility structure, and relatively easily to install and access for inspection and minor modification
- 6) Be relatively easy to manufacture
- 7) Allow for easy calibration in a separate wind tunnel

Pressure probes exhibit several advantages over other mechanical devices of measuring flow angle such as streamers and vanes. The measurements taken from pressure probes can be more easily related to a single point, and they tend to offer less disruption to the flow than alternative methods. Pressure probes are also not affected by inertial and gravitational effects than can influence measurements taken by mechanical devices [3].

All pressure probes used to measure flow quantities exploit the distribution of pressure that results around the surface of a body when it is immersed in a moving test fluid. This distribution of pressure can be measured using any number of pressure transducers that sample at different locations on the surface of the probe head. However, as will be discussed later, the sensors need not necessarily be mounted directly on the probe surface itself. The indicated pressure at each location on the probe head, or the fraction of free stream dynamic pressure recovered at each transducer location, will be dependent on the corresponding incident flow angle to the probe head [15]. The particular size and geometry selected for a pressure probe will be dependent on its particular intended use. Clearly, the physical dimensions of the pressure probe will limit the spatial resolution in measurements that can be obtained, not to mention the impact of probe size on flow disturbance. The complexity, including number of pressure tappings, of the probe will be dependent on the number of flow quantities, including flow angles, to be measured. Several pressure sensors can be mounted to quantify both pitchwise and spanwise flow angles, however, this can have a considerable effect on probe size, thus adversely affecting spatial resolution, as mentioned. This is a particular concern in

conditions such as traversing wakes experienced downstream of the rotor. As a result, it is often preferred to focus solely on pitchwise flow angle measurements, thus requiring three-hole pressure probes instead of a larger, more complex five-hole probe [24].

In the development of the probe to be used with the MIT Blowdown Facility, the radial flow angle measurement was sacrificed in order to allow for a smaller and less complex probe design. This led to a requirement for only three pressure measurement holes, which are spaced in the circumferential direction of the turbine stage when the probe is installed. Accommodations in the method of mounting the FAP in the test section were made in order to vary the radial location of the probe and obtain a measure of radial variations in the rotor exit flow angle. The mounting of the probe in the wind tunnel test section will be addressed in subsequent sections. The probe itself is illustrated in Figure 4.1 with an end view of the pressure holes on the probe nose surface also included. The pressure measurements taken from the three holes were labeled P_L , P_C , and P_R for the left, center, and right holes, respectively, as viewed from behind the probe facing into the oncoming flow. The pressure sensing holes shown in Figure 4.1 are labeled accordingly. Both the probe tube and stem were manufactured using 17-4 PH Stainless Steel. The diameter of the three pressure measurement holes is 0.036 in. each.

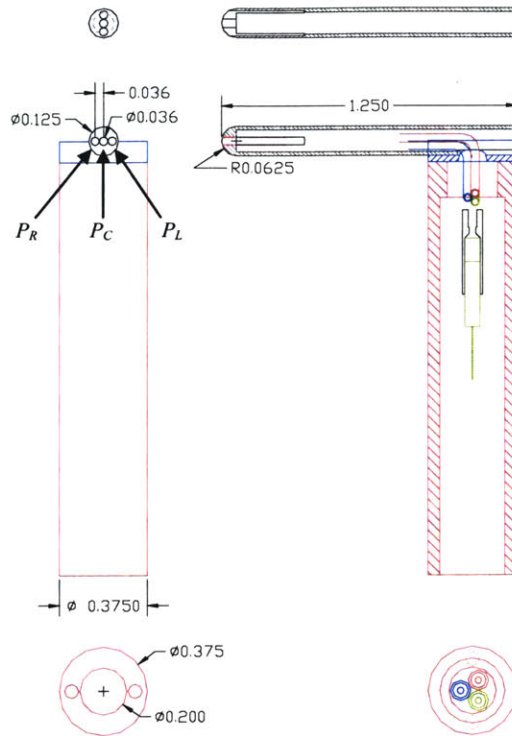


Figure 4.1: Front (left) and Side (right) Views of Flow Angle Probe Tube and Stem

As can be seen in Figure 4.1, the FAP consists of a cylindrical stem and a perpendicular tube for measurement. The axis of this tube lies perpendicular to the radial axis of the test section, and the head of the tube faces in the upstream direction during tests. An important design consideration is the shape of the head of this tube. The shape of the head of the probe must be such that it disturbs the flow as little as possible. A hemispherical end was selected for use with the FAP. The pressures resulting over the forward half of a sphere when inserted into a flow can be predicted with reasonable accuracy by simple potential flow theory [3]. Theoretical flow models were used as the basis for determining data reduction techniques to be described in further sections. A more detailed view of the probe tube itself is shown in Figure 4.2. An advantage of using a hemispherical probe head is that the shape allows for less restrictive internal leads for the pressure measurements. Cross-sections of the three internal leads can be seen in Figure 4.2. The reduction in restriction of internal leads results in less lag of the pressure signal in these leads and a simpler internal design [14].

The shape of the probe nose was to be as close to hemispherical as possible. The diameter of the nose was machined to be 0.125 in. Care was taken to ensure smoothness in contour and surface finish. It was also extremely important to ensure that the edges of the surface holes were free of burrs, which would affect the flow around the surface. Erroneous pressure results would be obtained if the air were deflected appreciably. In any event, calibration of the probe was used to account for any prevailing imperfections in its manufacture. Discrepancies such as burrs pose the largest concern because their form can be altered following the calibration of the probe during experimental testing, rendering the calibrations inaccurate.

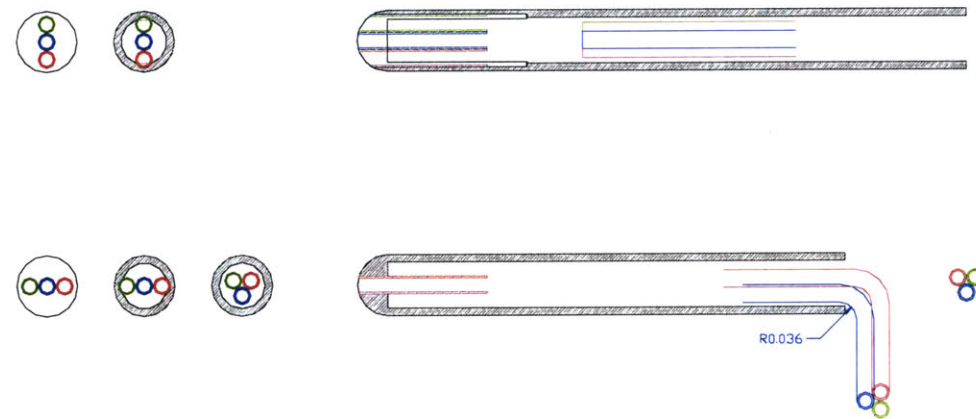


Figure 4.2: Side (below) and Top (above) Views of Flow Angle Probe Tube, with Internal Leads

As mentioned earlier, flow direction is determined by measuring the pressure at ports placed on either side of a probe. The differential pressure between two ports can be calibrated as a function of incident flow angle. The pressure holes on the FAP nose were drilled parallel to the axis of the cylindrical probe tube, as is illustrated in Figure 4.2. The sensitivity of a flow angle measuring device is a performance parameter that is related to the change in measured pressure differential between surface locations with a change in the incident flow direction. The sensitivity of hemispherical-ended probes is a function of the offset angle, δ , of the pressure measurement holes. The highest sensitivity for a probe with this profile is obtained with pressure holes having an offset angle of 45° [3].

Since the pressure measurement holes for the FAP were not drilled to a specific offset angle, only an approximation of the angle was obtained from calibration. The effective offset angle of the hole on the FAP was determined to be approximately 38° , which is quite close to the ideal theoretical value. The details of this approximation will be given with those of the probe calibration in later sections.

Another factor that can affect the pressure distribution about the head of the probe is the position of the probe stem. The stem for the FAP is shown in Figure 4.1, and its axis is perpendicular to the direction of flow. In the flow, the stem will produce a pressure at points on the probe tube upstream of itself, which can affect the measurement of pressure at the three surface locations. Thus, the position of the pressure measurement holes relative the probe stem is an important design consideration, which is determined by the length of the probe cylindrical tube. The maximum possible distance from the probe stem to the measuring plane would be ideal, however the rigidity of the probe will limit this distance. Vibrations in the FAP, which can result in erroneous flow angle readings, may occur due to the flow around the probe. In order to avoid overall vibrations, the stem of the probe is thicker, with a diameter of 0.250 in., than the probe tube. Previous research in the field of hemispherical pressure probes has shown that pressure measurements made at a distance of eight probe diameters upstream of the stem will be unaffected by the presence of the stem for subsonic flows [14]. Figure 4.1 shows that the FAP design allows for 1.00 in. between the tip of the nose and the beginning of the stem, which corresponds to eight times the probe diameter of 0.125 in.

The spatial resolution of a device measuring fluid flow will also be affected by the manner in which the pressure transducers are housed in the probe. The size of the probe head will determine the effective spatial resolution of flow measurements. In addition to the number of pressure measurement holes on the probe, the location of the transducers will have a significant influence on the size of the probe's nose. One way to maintain small probe geometry with a number of sensor holes is to move the pressure transducers away from the surface pressure holes and mount them remotely in the probe's body or stem. Sub-surface mounting of the pressure sensors also provides them with better protection against mechanical damage and temperature changes in short duration facilities. However, the benefits of situating the transducers internally do not come

without drawbacks. Moving the pressure transducers away from the probe's surface reduces the maximum frequency response capability of the transducers. The use of tubing to transmit the pressure signals from the probe head to the sensors will result in a damping effect that reduces the frequency response of the measurement system. The simplest evaluation of the resonance frequency of the tubing system is obtained from the organ-pipe model or a Helmholtz generator [24]. A tubing arrangement was designed for the FAP in which short lengths, approximately 1.250 in., of 0.028 in. inner diameter stainless steel tubing were braised to each of the three pressure holes on the probes surface. Using identical geometry for the internal leads ensured similar pressure response for each pressure measurement. As can be seen in Figure 4.1, the three tubes pass the length of the probe tube and are bent into the stem section. Wells to house the fast response pressure transducer are braised to the terminating end of the pressure transmission tubes. The wells used to mate the internal tubing and the pressure transducers are shown in Figure 4.3. The pressure transducers were epoxied snugly into these wells.

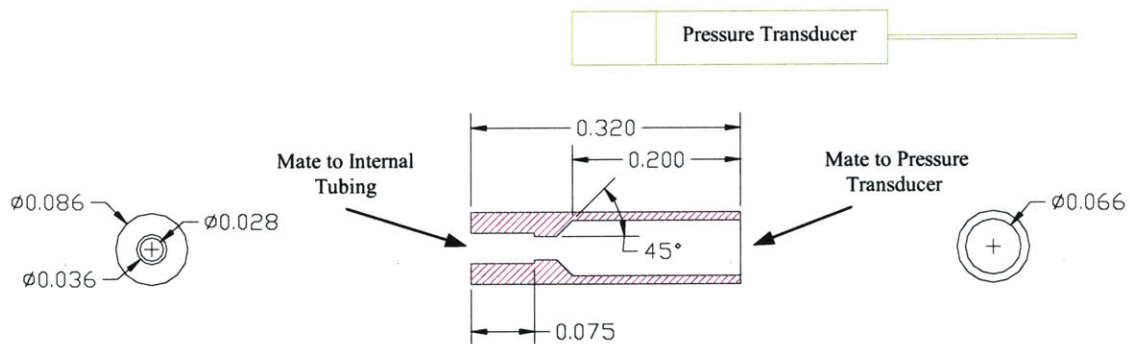


Figure 4.3: Flow Angle Probe Pressure Transducer Wells

Pressure transducers used in such a device have their own frequency response. The tubing arrangement reduces the available upper limit of this response, but not beyond the point where the effects of nozzle guide vane (NGV) wake passing can be resolved, which will become evident when discussing the reduction of experimental data. During the

design of the internal leads of the FAP, it was necessary to establish a viable trade-off between time resolution and spatial resolution of the pressure measurements.

4.3 Pressure Transducers

The sensors used to measure the pressure being transmitted from each surface location on the probe head were Kulite XCQ-062-50D miniature, silicon-bonded, high frequency, differential pressure transducers. These Kulite transducers are among the smallest available, with an inner diaphragm diameter of 0.064 in. The transducers measure the pressure differential between the FAP internal lines and backpressure reference tubes. Small pieces of Tygon tubing, with an inside diameter of 0.010 in., were used to connect the transducer backpressure tubes to the reference pressure line of the probe assembly. As detailed in Chapter 2, these transducers were calibrated during the course of a test run.

The normal frequency response range of these high frequency Kulite pressure transducers is DC to more than 100 kHz [27]. However, as mentioned previously, the use of internal tubing reduces the upper limit of this range. The estimated frequency response of the FAP is on the order of 1 kHz. As is shown in Figure 4.3, the inside diameter of the wells to house the transducers was machined to 0.066 in. so that the transducers could be tightly secured and bonded with epoxy.

Pressure transducers of the type used in this research effort can be sensitive to changes in temperature. Changes in the offset and sensitivity of the transducer can occur with temperature changes, leading to erroneous readings of the actual pressure. However, this is much more of a prevalent problem in steady state testing than in transient experiments, where time scales of tests are too small to allow significant temperature changes in the vicinity of the pressure transducers. Nevertheless, the pressure transducers used employ temperature compensators to adjust the bridge output via external compensation resistors to account for any thermal fluctuations [24].

4.4 Flow Angle Probe Installation

Once details of the FAP design was addressed, the instrument needed to be incorporated into the test section of the experimental facility. This was, of course, following calibration of the instrument, which will be discussed in detail in the following chapter. The FAP was mounted in an existing instrument port, which had previously been used to house a total temperature rake, on the translator downstream of the turbine rotor. The use of this port was attractive from the perspective of minimizing modifications to the facility because of the availability of pre-existing electrical wiring infrastructure running from the test section to the data acquisition system. The downstream translator employs standard Bendix-type electrical ports for the instrument socket and test section output. The use of familiar wiring junctions allowed the electrical connections to the pressure transducers to be made with ease. This type of connector can also accommodate reference backpressure lines from the pressure transducers. Figure 4.4 shows the FAP assembly in a housing that mates to the connector port on the downstream translator. A view of the FAP installed in the downstream translator of the test apparatus is shown in Figure 4.5.

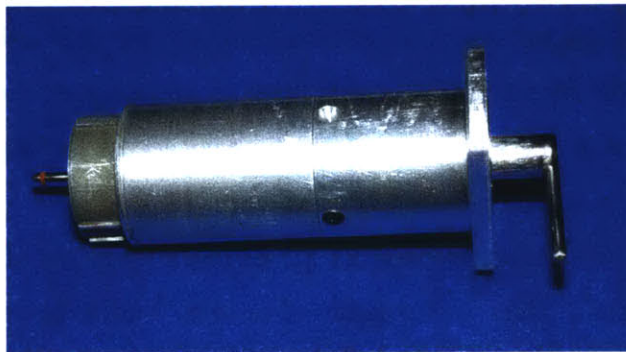


Figure 4.4: Flow Angle Probe Complete Assembly

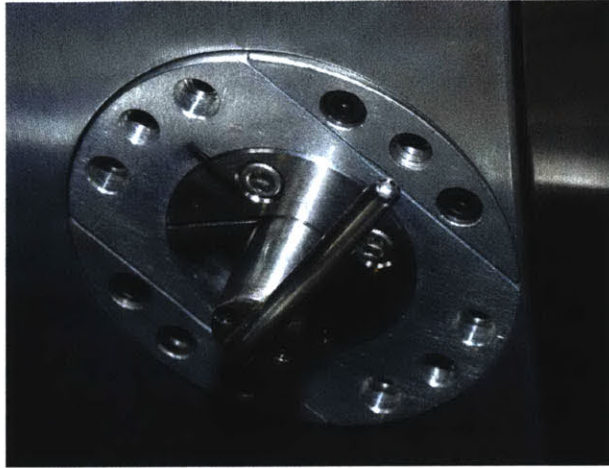


Figure 4.5: Flow Angle Probe Installed in Blowdown Test Section

An important characteristic of the design of the FAP assembly is that it allows adjustment of the probe's position and orientation. Tests were to be conducted with the FAP at varying radial distances between the hub and tip of the flow annulus. There was also a requirement to be able to adjust the alignment of the probe's head in the tangential plane with respect to the axial direction of the test section. This will be discussed in the following chapter. Both of these requirements were met with the use of a collar around the stem of the probe, which can be seen in Figure 4.5. When the collar's set screws are loosened, the probe is free to rotate and traverse in its housing. Once the desired position is achieved, the screws are tightened. A small amount of excess length was left in the FAP wiring to allow for the radial travel. Removal of a metal plate covering the window to the test section at the probe's location allows for easy access to the probe without dismantling the entire test section.

As mentioned, the ability to rotate the probe in the plane about its stem was an important design capability during assembly and testing. The reason for this was that the probe needed to be aligned in the same general direction as the flow so that the most accurate measurement results could be obtained. Based on a general three-dimensional computational fluid dynamic (CFD) model of the test stage provided by the sponsor, the probe was to be installed at an angle of 25° to the left, when viewed facing upstream in the flow, from the longitudinal axis of the test section. Deviations of the flow angle relative to this position of the FAP were expected to be measurable with more certainty. These points will be elaborated upon in further sections. In order to align the FAP at this

25° angle, an aluminum block was machined to offer the correct angle with respect to the test section. The FAP was aligned flush with the block before tightening the collar around its stem.

4.5 Summary

A review of the design, fabrication, and installation of the FAP has been presented. Several factors were considered and weighed in the selection of design criteria. As is often the case with experimental instrumentation, certain design trade-offs were required to tailor the performance of the device to research requirements. These included the competing issues of spatial and time resolution of measurements. A detailed calibration of the instrument was also required, which will be the focus of the next chapter.

Chapter 5: Flow Angle Probe Calibration

5.1 Introduction

Prior to utilizing an instrument such as the flow angle probe (FAP) for the purpose of collecting experimental data, a calibration must be performed. The need for a calibration arises from the fact that the performance of such devices can only be approximated by theory. This is due to the variety of factors that influence variations in probe behaviour, which were discussed in the previous chapter. A description of the calibration procedure implemented and associated details regarding error analysis and propagation are included herein.

5.2 Motivation

The requirement to calibrate the flow angle measuring device stems from the selected mode of operation of the instrument in this experiment. This is because pressure probe flow direction instruments can be operated in two distinct ways. Both methods can be employed using similar probe designs with symmetrically distributed pressure sensing holes, as is the case with the FAP.

The first of these is known as the alignment or null-reading method. In this method of operation the probe is orientated such that equal pressure measurements are obtained in symmetrically oriented pairs of holes, P_L and P_R in the case of the FAP being used to measure the pitchwise flow angle. Once equivalent pressure readings are obtained, the probe is essentially aligned with the direction of the flow, and the geometry of the probe relative to the test section gives the flow angle. The null-reading method of operation requires a minimum amount of calibration, however, it also requires longer

running times and more complex and bulky probe housing and rotating mechanisms [15]. As a result, it is not a viable option for use in a short-duration experimental facility such as the MIT Blowdown Facility.

The alternative method of operation involves fixing the position of the probe and measuring pressure differences between symmetrically opposed holes. The flow direction can be related to these pressure differences by way of a prior calibration, obtained by orienting the probe, known flow. Ideally, a probe to be used in this manner should be arranged such that the angle between the probe's axis and the incident flow are related linearly to the difference in pressure to be measured [3,14]. References show that the approximate range of $\pm 15^\circ$ between the probe and incident flow will offer such a linear relationship between pressure difference and flow angle for multi-port probe heads [3]. It was for this reason that the FAP was oriented at a 25° angle with respect to the test section longitudinal axis when the probe was installed for testing, as mentioned in the previous chapter. An additional benefit to roughly aligning the probe with the flow is that it will interfere less with the natural flow tendencies in the test section.

The latter of the two methods outlined above was selected for use with the FAP. As a result, an in-depth calibration of the probe under steady conditions was required. The calibration was carried out over a wide range of incident flow angles and flow Mach numbers.

5.3 Calibration Procedure

The calibration of pressure probes intended to measure flow orientation is generally carried out by measuring pressure differences measured between sensing holes with varying incident stream directions. In actuality, the ideal scenario for calibration of such an instrument is to find non-dimensional variables based on pressure readings, which are only sensitive to the flow parameter being investigated. The specific choice of non-dimensional parameter relating to circumferential flow angle will be discussed in subsequent sections. Regardless of the selected non-dimensional variable to be used in the data analysis, the basis of the calibration is to obtain readings from each of the three

pressure measurement locations on the probe's surface under steady-state flow conditions. Additional variables that can affect the performance of a pressure probe are the Reynolds number and the Mach number of the flow. Thus calibrations should include flows with varying Mach number and Reynolds number to determine whether or not these will be significant factors in the flow around the probe being calibrated. However, these parameters could not be varied independent of one and other since only a constant inlet total pressure was available. Ideally, one could determine a Mach number above which the influence of these parameters on probe performance is negligible.

The FAP calibration was carried out in a 7 in. x 7 in. plexiglass test section mounted to a De-Laval compressor. The turbomachinery of the De-Laval compressor is used to induce the required flow through the test section, and a suitable range of flow Mach numbers can be obtained by varying the compressor speed. The FAP was mounted through a window in the test section as is shown in Figure 5.1.

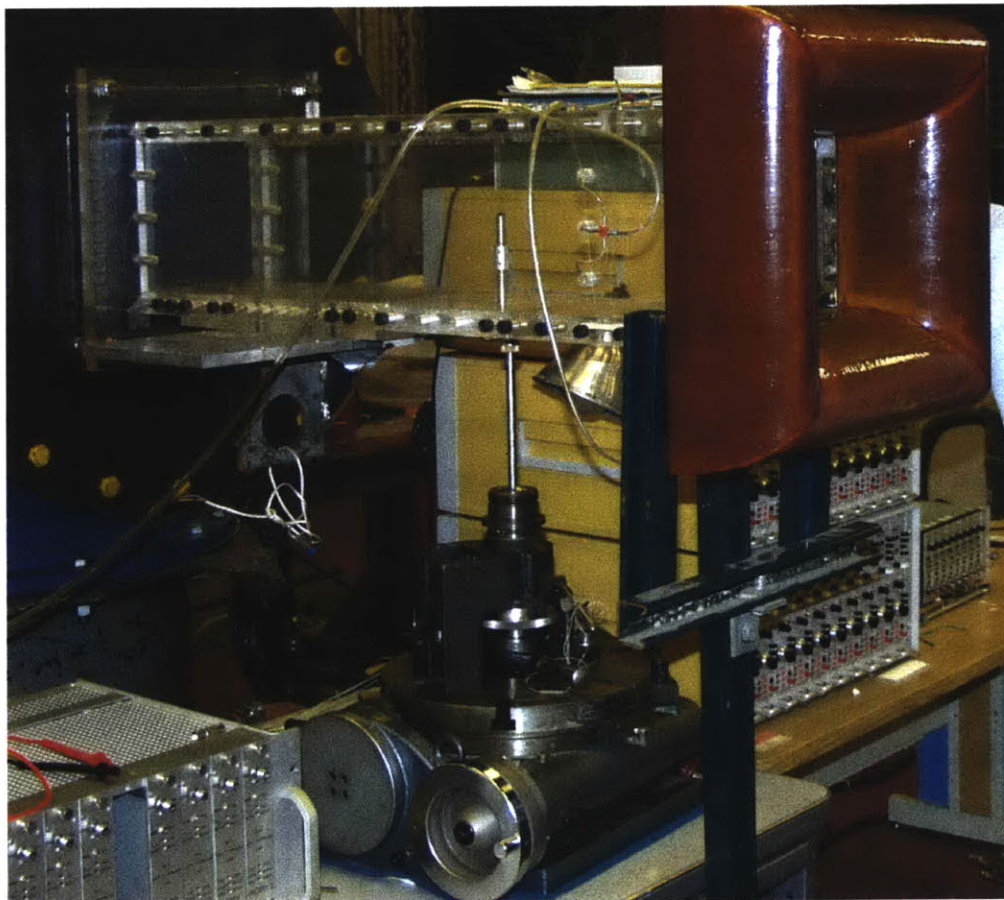


Figure 5.1: Calibration Arrangement for Flow Angle Probe

A cylindrical stem extension including a collar allowed the FAP to be attached to a precise rotary table that was used to yaw the probe with respect to the inlet flow. The probe was initially centred using a null-reading type method where the probe was rotated until the P_L and P_R pressure readings were balanced during steady flow through the test section. A total of five different flow Mach numbers were used during the calibration. At each of these inlet flow Mach numbers, the FAP was positioned at angles ranging from -55° to 55° in increments of 5° , with additional increments of 1° in the range of yaw angles from -5° to 5° . An arbitrary decision was made to define a positive flow angle as being incident on the left side of the probe head when viewed from above. The convention for describing flow angles for the FAP is included below in Figure 5.2.

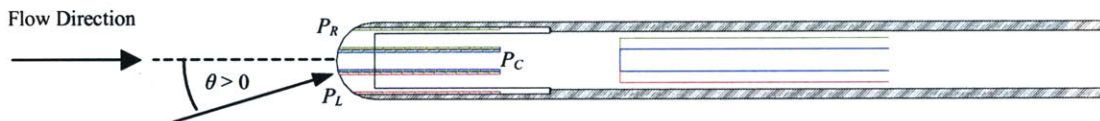


Figure 5.2: Flow Angle Convention for Flow Angle Probe (viewed from above)

Measurements from the Kulite pressure transducers were taken through the same data acquisition (DAQ) system to be used with the actual Blowdown Facility experiments. A separate LabView program was written to average the steady state pressure readings at each incident flow angle and inlet flow condition. In addition to the three FAP surface pressure measurements, the ambient and inlet wall static pressure were also recorded using a Setra Model 370 Digital Pressure Gage. These measurements provided for the calculation of the free stream Mach number in the test section for each different compressor speed setting.

5.4 Calibration Results

5.4.1 Surface Pressure Measurements

The actual measurements made during the calibration of the FAP were the variations in the three surface pressures with changes in the incident flow angle. A sample of the measurements made at a single inlet flow condition during the calibration is included in Figure 5.3.

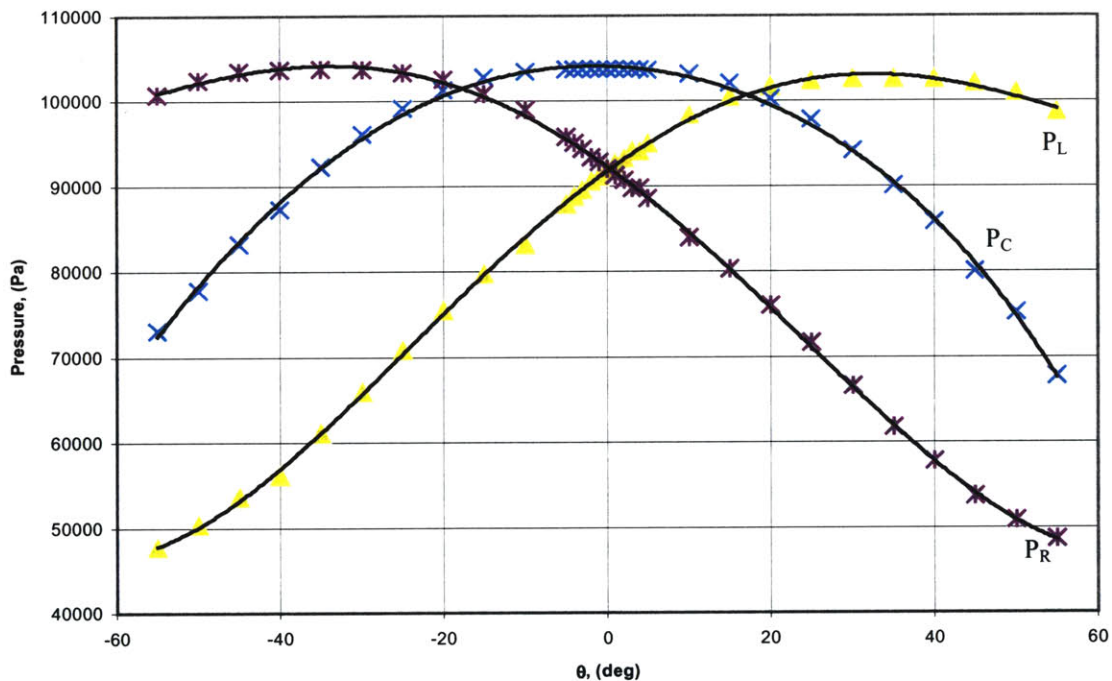


Figure 5.3: Flow Angle Probe Surface Pressure Measurements with Incident Flow Angle, $M=0.57$

The general shape of this plot is also representative of those derived from conditions involving the five different inlet flow Mach numbers examined. The calibration plot shows how the pressure recovery at each measurement location varies as the probe is rotated about its stem. A smooth polynomial fit of fifth order is used to allow for interpolation between the raw pressure measurements plotted in Figure 5.3. Each surface hole is seen to have a maximum reading, located by a horizontal tangential slope to the curve, which corresponds to the angle of the FAP at which the flow is aligned with that

particular hole. The fact that the maximum value of P_C occurs at 0° would imply that the probe's initial alignment with the flow direction during the calibration sequence using the 'null-reading' method was sufficiently accurate. As mentioned earlier, the holes drilled on the FAP have an associated offset angle, δ , which is difficult to physically measure. However, Figure 5.3 gives an indication of the approximate effective offset angle, which can be a result of machining inaccuracies causing flow disruption in and around the measurement holes. Figure 5.3 shows that the maximum pressure recovery for P_L and P_R occurs at approximately 38° . This, and the fact that the curves for P_L and P_R cross each other at nearly 0° would imply that the FAP is symmetrical in its physical geometry.

5.4.2 Dimensionless Pressure Parameter for Tangential Flow Angle

In order to render the calibration measurements useful and applicable to characterizing the flow during actual facility test runs, the data must be modified for the particular flow characteristic being sought. As mentioned earlier, data is normally manipulated to form a non-dimensional parameter, often based on pressure differences, that reacts linearly to the flow parameter under investigation over the range of interest. The objective here is to be able to predict the tangential flow angle, θ , from the measured pressures P_L , P_C , and P_R . Insight into the selection of an appropriate non-dimensional parameter was obtained by examining the expression for surface pressure in inviscid potential flow around a sphere given by Anderson [1]. The surface pressure at each of the measurement locations, as shown in Figure 5.3, on the FAP in potential flow is

$$P_L = P_0 - \frac{9}{4}Q \sin^2(\theta - \delta) = P_0 - \frac{9}{4} \left(\frac{1}{2} \rho (\gamma RT) M^2 \right) \sin^2(\theta - \delta) \quad (5.1)$$

$$P_C = P_0 - \frac{9}{4}Q \sin^2(\theta) = P_0 - \frac{9}{4} \left(\frac{1}{2} \rho (\gamma RT) M^2 \right) \sin^2(\theta) \quad (5.2)$$

$$P_R = P_0 - \frac{9}{4}Q \sin^2(\theta + \delta) = P_0 - \frac{9}{4} \left(\frac{1}{2} \rho (\gamma RT) M^2 \right) \sin^2(\theta + \delta) \quad (5.3)$$

In the above expressions, P_0 is the total pressure, Q is the dynamic pressure, and $\sqrt{\gamma RT}$ is the speed of sound of the flow being investigated. We wish to find a dimensionless variable that is independent of both P_0 and Q since these are unknown quantities in the actual facility. It is important to remember that the dynamic pressure is proportional to the square of the flow Mach number for incompressible flow, as is shown in the equations above. The dimensionless variable should be a function only of measured quantities in order to avoid the need for iterative steps in the analysis scheme. The variable must also be monotonic with respect to the flow attribute being measured. This ensures that only a single value of the non-dimensional variable exists for each value of the flow parameter. It can be seen that both the total and dynamic pressures will be removed from any expression involving the quotient of two differential pressure terms. The total pressure is removed when the mathematical difference is taken between any pair of Equations (5.1), (5.2), and (5.3). The dynamic pressure is then withdrawn when any two terms without the total pressure variable form a quotient. Previous flow characterization efforts [16] were the basis of the selection of the following non-dimensional pressure parameter for measuring the tangential flow angle,

$$\psi(\theta) = \frac{P_L - P_R}{(P_C - P_L) + (P_C - P_R)} = \frac{P_L - P_R}{2P_C - P_L - P_R} \quad (5.4)$$

The numerator of Equation (5.4) is the pressure difference between P_L and P_R , which is quite sensitive to the pitchwise flow angle. This difference is normalized by an approximation to the flow total pressure, ($2P_C - P_L - P_R \approx 2Q$). The parameter $\psi(\theta)$ was expected to display very little variation with flow Mach number and radial flow angle. The extent to which this expectation was applicable to our calibration was determined by plotting the dimensionless pressure parameter versus a range of tangential flow angles for Mach numbers of 0.57, 0.53, 0.47, 0.40, and 0.34 as shown in Figure 5.4.

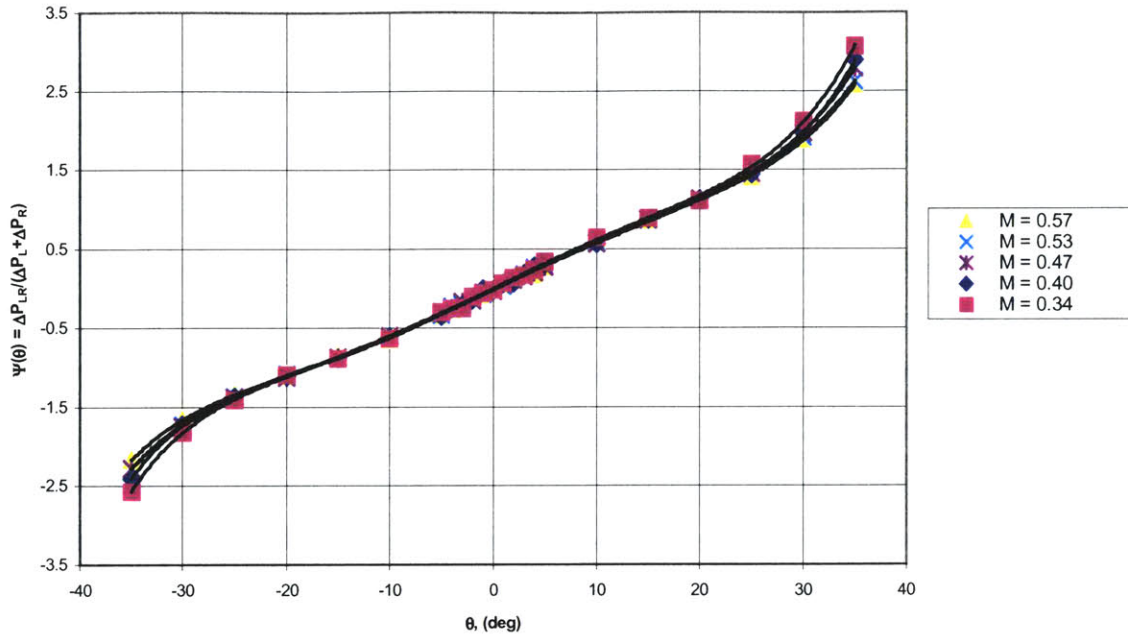


Figure 5.4: Flow Angle Probe Dimensionless Pressure Parameter with Incident Flow Angle

The range of inlet tangential flow angles used for Figure 5.4 was limited to -35° to 35° because all values diverge significantly beyond those limits. Once again, a smooth polynomial fit of fifth order is used to allow for a more accurate comparison between the different Mach number runs of the calibration. Figure 5.4 shows that the data points for the three fastest inlet Mach numbers (0.57, 0.53, and 0.47) lie close together over the entire range. Over a reasonable range of Mach numbers, there is very little variation in the relationship between tangential flow angle and the dimensionless flow angle chosen. The range of these three Mach numbers encompasses the estimated rotor absolute exit Mach number as determined from data provided by the manufacturer. The dimensionless values for the remaining two Mach numbers (0.40, and 0.34) diverge somewhat from the mean, especially at extremes of the incident flow angles included in Figure 5.4. It is also important to note that the three higher Mach number flows seem to give a linear relationship between the non-dimensional flow parameter and the flow angle on the range of -20° to 20° . This was encouraging considering that, as mentioned earlier, literature suggests that an ideal scenario is to have a linear relationship between the flow variable and the dimensionless parameter.

5.4.3 Tangential Flow Angle Calibration Curve

In order to apply the calibration data to facility test data, a calibration curve of the tangential flow angle with dimensionless pressure parameter must be created. A calibration curve was created based on the data shown in Figure 5.4. A modified calibration data set was generated by averaging the values of $\psi(\theta)$ from the three highest Mach number calibration runs over the range of flow angles from -20° to 20° . Figure 5.5 shows the first order linear regression that was used to fit the tangential flow angle versus the selected non-dimensional pressure parameter.

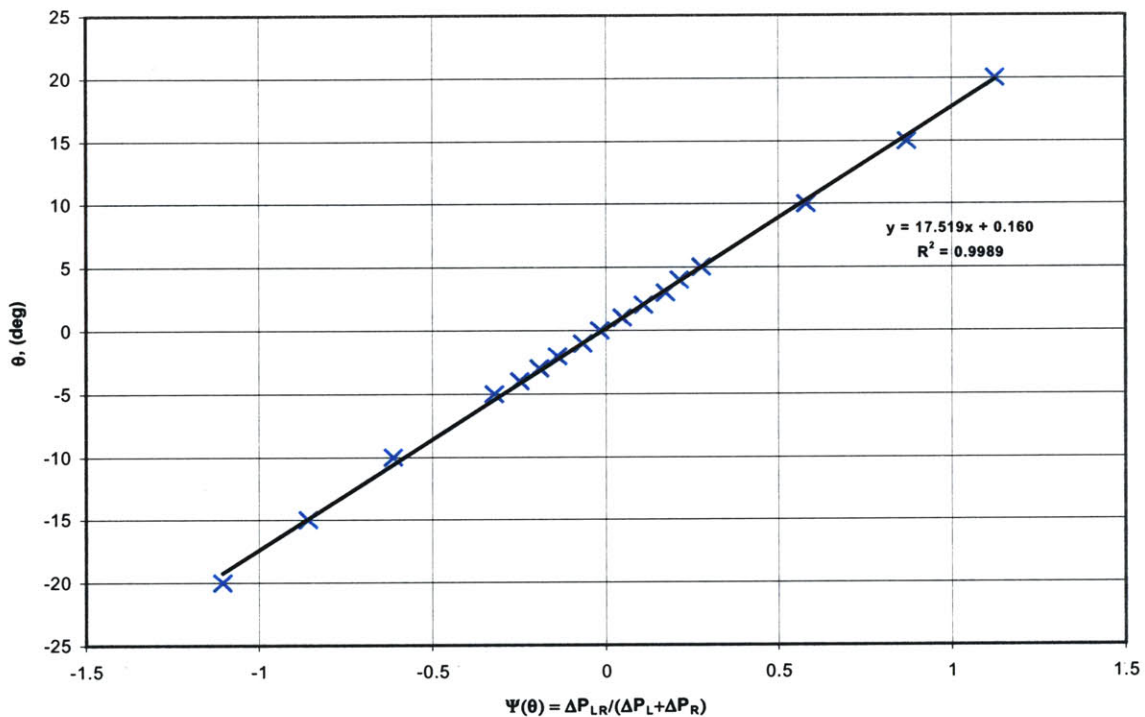


Figure 5.5: Flow Angle Probe Incident Flow Angle with Experimental Averaged Dimensionless Pressure Parameter (for Mach 0.57, 0.53, 0.47)

The equation for the first order line of best fit for the data is included in Figure 5.5. The curve is seen to be a good fit to the data pairs as is shown by the R^2 value of 0.9989. The coefficient of determination, R^2 , is the proportion of the total variability explained by the regression model, or put simply the overall adequacy of the model [29]. A value of the coefficient very close to unity implies that the linear model chosen suits the data points

very well, and that the relationship shown can be used with confidence over the intended range of variables.

The equation for the relationship depicted in Figure 5.5, where the flow angle is represented in degrees, is shown to be $\theta(\psi) = 0.160(\psi) + 17.519$, as determined by the method of least squares. With this equation the incident tangential flow angle can be determined from an experimental value of the non-dimensional pressure parameter measured with the FAP. However, one important additional point that must be considered is the error associated with the use of this calibration curve. This will be the focus of the following section.

5.5 Calibration Error Analysis

As with any procedure involving measurements taken from an experimental apparatus, a calibration of the sort carried out for the FAP has a certain degree of error associated with it, which cannot be ignored in a rigorous analysis. The regression model will have an associated uncertainty, which stems from the uncertainty in the measured variables that create the data pairs. Ideally, one would like to incorporate the uncertainties in the measurements taken to create the calibration curve to give an uncertainty in the coefficients of the regression curve representing the relationship shown in Figure 5.5. If the uncertainty in the fit coefficients were known, then they could be propagated through to the final calculated results during the reduction of experimental test data.

Often times in experimental activities the uncertainty in the original measured data are not included in further analysis and use of models. These models cannot predict the true performance of a piece of equipment under study because uncertainties are neglected. Uncertainty in the regression model is required to provide an interval within which the instrument actually performs as it is expected to. Coleman and Steele [5] present a comprehensive approach to linear regression uncertainty. In the method of least squares, the first order linear regression coefficients for the slope, m , and intercept, c , can be considered functions of the N data pairs, (ψ_i, θ_i) used to create the calibration. The

reference material gives expressions for incorporating the absolute random uncertainty, U_{θ_i} and U_{ψ_i} , in both of the measured variables to give the uncertainty in the slope as

$$U_m^2 = \sum_{i=1}^N \left(\frac{\partial m}{\partial \theta_i} \right)^2 U_{\theta_i}^2 + \sum_{i=1}^N \left(\frac{\partial m}{\partial \psi_i} \right)^2 U_{\psi_i}^2 \quad (5.5)$$

Similarly for the intercept,

$$U_c^2 = \sum_{i=1}^N \left(\frac{\partial c}{\partial \theta_i} \right)^2 U_{\theta_i}^2 + \sum_{i=1}^N \left(\frac{\partial c}{\partial \psi_i} \right)^2 U_{\psi_i}^2 \quad (5.6)$$

The partial derivatives represented in the equations above need not be determined analytically, instead they can be evaluated numerically. The following expression was used to approximate the partial derivatives

$$\left. \frac{\partial r}{\partial X_i} \right|_{X_2, \dots, X_N = \text{const}} \approx \frac{\Delta r}{\Delta X_i} \quad (5.7)$$

The remaining inputs that need to be determined in order to evaluate Equations (5.5) and (5.6) are the absolute random uncertainty, U_{θ_i} and U_{ψ_i} , in both of the measured variables. An estimate for U_{θ} of 0.02° was made for the rotary table used to set the incident flow angles. The determination of U_{ψ} for each point in the calibration data set was slightly more complicated since these values are unique for each point in the data set and they arise from a calculation involving the measured pressures from the Kulite pressure transducers. The reference [5] describes a general uncertainty analysis that can be employed to propagate random errors through mathematical equations. For the case of an experimental result, r , which is a function of J measure variables, X_i , the relative uncertainty is described by

$$\frac{U_r^2}{r^2} = \left(\frac{X_1}{r} \frac{\partial r}{\partial X_1} \right)^2 \left(\frac{U_{X_1}}{X_1} \right)^2 + \left(\frac{X_2}{r} \frac{\partial r}{\partial X_2} \right)^2 \left(\frac{U_{X_2}}{X_2} \right)^2 + \dots + \left(\frac{X_J}{r} \frac{\partial r}{\partial X_J} \right)^2 \left(\frac{U_{X_J}}{X_J} \right)^2 \quad (5.8)$$

This general uncertainty expression can be applied to Equation (5.4) for the non-dimensional pressure parameter to give the relative random uncertainty in each calculated value of the parameter,

$$\begin{aligned} \frac{U_\psi^2}{\psi^2} = & \left(\frac{2(P_C - P_R)}{(P_L - P_R)(2P_C - P_L - P_R)} \right)^2 U_{P_L}^2 + \left(\frac{-2(P_C - P_L)}{(P_L - P_R)(2P_C - P_L - P_R)} \right)^2 U_{P_L}^2 \\ & + \left(\frac{-2P_C}{(2P_C - P_L - P_R)} \right)^2 \left(\frac{U_{P_C}}{P_C} \right)^2 \end{aligned} \quad (5.9)$$

The value of the relative random uncertainty in the Kulite pressure transducers, U_{P_L}/P_L , U_{P_R}/P_R , and U_{P_C}/P_C , was obtained by analyzing the pressure transducer calibrations performed in a single run. The difference in the scale and zero values for the postfill and posttest calibrations against a known pressure value offer insight into the error in these values. The value of the relative random error for each transducer was determined to be 0.25 %. It is also important to remember that the dimensionless pressure parameter used in creating the calibration plot was an average of three different values each from a different Mach number trial. Thus, Equation 5.8 must also be employed to accrue the absolute random uncertainty in each dimensionless pressure parameter measurement used for the average value,

$$U_\psi^2 = \left(\frac{U_{\psi_{M_1}}}{3} \right)^2 + \left(\frac{U_{\psi_{M_2}}}{3} \right)^2 + \left(\frac{U_{\psi_{M_3}}}{3} \right)^2 \quad (5.10)$$

Once all components of the regression error analysis had been accounted for, the error in the slope and intercept of the first order linear fit were calculated using Equations (5.5) and (5.6). Incorporating the error analysis as described above the slope was

determined to be $0.160 \pm 0.059^\circ$, and the intercept was $17.519 \pm 0.151^\circ$. The error analysis in the calibration of the FAP is the last step required to allow for experimental measurements with uncertainty to be made using this instrument. The values for the calibration coefficients will allow for the errors associated in the calibration process to be carried through in subsequent analysis.

5.6 Summary

A detailed description of the calibration used with the FAP has been discussed. The rationale for such a procedure was included, as were the procedure followed and the results of the calibration. The important issue of uncertainty analysis and propagation in the calibration was also included. This will allow for a realistic estimate of the uncertainty in the final measured values to be made. The application of the results of the calibration of the FAP will become evident in subsequent sections involving the analysis and discussion of experimental results.

Chapter 6: Flow Angle Probe Experimental Results

6.1 Introduction

The flow field under investigation in this experimental study is extremely complex. The flow angle probe (FAP) is being used in a three-dimensional, unsteady flow, which is also influenced by the nearby passing turbine rotor blades. In order to gain insight into the flow characteristics in a full-sized engine, the FAP was mounted on a translator downstream of the rotor in a fully-scaled, film-cooled turbine test section, which itself was described in detail in Chapter 2. The preceding calibration of the FAP was used as the fundamental basis for determining the tangential flow angle, as well as associated uncertainty, during the experimental test runs. Using the translator, tangential flow angle measurements were taken across a portion of the circumference of the rotor exit in hopes of observing fluctuations while passing through nozzle guide vane (NGV) wakes. These measurements were taken for different FAP radial positions and engine operating points. The basis for varying the operating point will be discussed prior to presenting and analyzing data. A test matrix will also be presented to ease in the comparison of data taken from various test runs. The results of this initial experiment lead to a brief discussion comparing spatially-resolved and spatially-averaged tangential flow angle data taken from various test runs.

6.2 Turbine Operating Point

6.2.1 Turbine Stage Operating Point Map

As mentioned earlier, several non-dimensional engine parameters must be matched in order to ensure test similarity and applicability of the test results. Because the Reynolds number and ratio of specific heats are both kept within an acceptable range throughout the test runs, the turbine operating point will be defined by the pressure ratio and corrected speed. A turbine stage operating map with pressure ratio versus corrected speed can be constructed to give a visual representation of the operating point with test time. An example of an operating point map is included below in Figure 6.1.

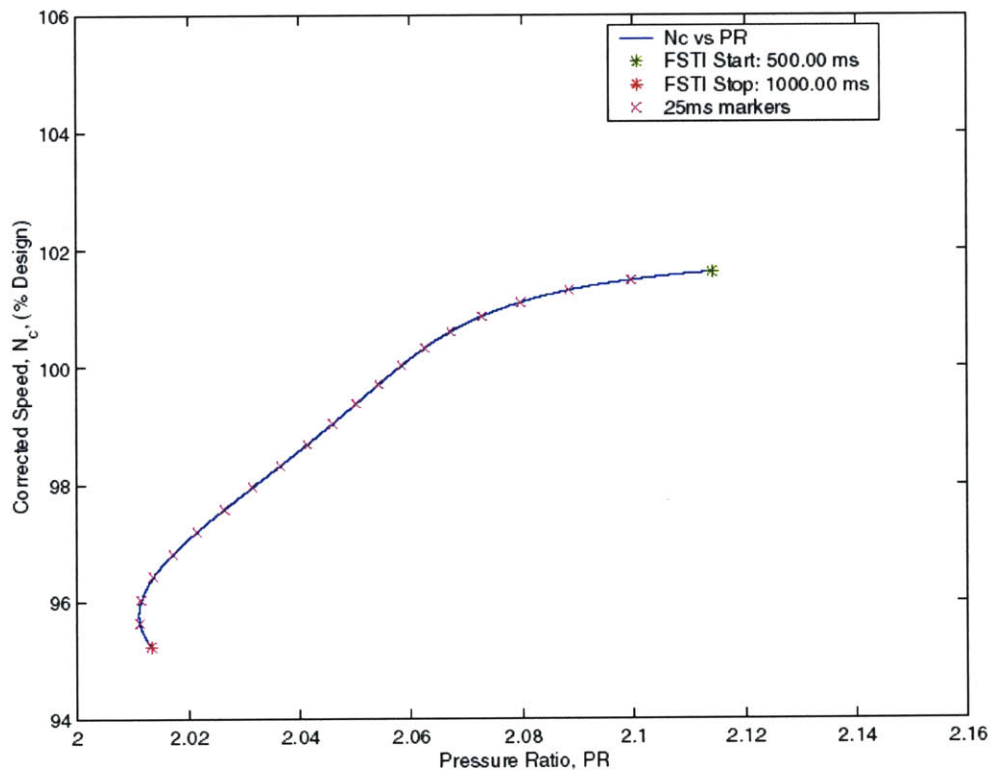


Figure 6.1: Turbine Stage Operating Point Map, T222

Markers for the operating point are included every 25 ms between selected time intervals. Note that a single complete revolution of the rotor occurs approximately every 10 ms, so the operating point markers shown can be thought of as representing quasi-steady points of the turbine operating point. The choice of the interval to be used in test comparison will be addressed in the next section. These stage operating maps serve as the basis for determining the suitability of comparisons between various experimental test runs.

6.2.2 Flow Similarity Time Interval

With an unsteady experimental apparatus, like the MIT Blowdown Facility, it is important to remember that an initial transient startup period exists, which will not yield useful data. As a result, data analysis must be confined to a defined time interval where the flow is appropriately scaled. This period is termed the flow similarity time interval (FSTI). For the results to be presented here, the FSTI begins at 500 ms and ends at 1000 ms after the beginning of the test run. The FSTI was selected based on the analysis of previous experimental results at the MIT Blowdown Facility [28]. The FSTI will be used for all analysis, including the turbine stage operating maps as shown in Figure 6.1.

6.3 Development of Test Conditions

The FAP was implemented in the experimental engine apparatus in order to spatially-resolve measured tangential flow angles at various radial locations between the rotor exit hub and tip at different engine operating points. As mentioned earlier, this spatial-resolution of flow angle was provided by the use circumferentially traversing downstream translator, on which the FAP was mounted. A total of six different FAP radial positions were included in the tests. The combination of the use of the translator and variations in probe radial position was intended to provide a useful map of the flow angle across NGV wakes that would be encountered by the translating FAP. Increasing the corrected speed from the design point at most of the radial probe positions was used to change the operating point. The design point was taken from experimental tests

carried out by Van Poppel [28]. A summary of the turbine test runs is included below in Table 6.1.

Table 6.1: Flow Angle Probe Test Run Summary

Test Number	FAP Centreline from Translator-Ring, (in.)	Rotor Corrected Speed, N_c	FAP Offset Angle (from test section longitudinal axis)
T221	0.54	Low	25° left
T222	0.54	Design	25° left
T223	0.35	Design	25° left
T224	0.35	Design	25° left
T225	0.15	Design	25° left
T226	0.15	High	25° left
T227	0.75	Design	25° left
T228	0.75	High	25° left
T229	0.94	Design	25° left
T230	0.94	High	25° left
T231	1.075	Design	0°
T232	1.075	High	0°

The radial position of the probe was measured from the surface of the translator to the center of the middle hole of the probe tube. Varying the eddy current brake excitation voltage changed the corrected speed.

6.4 Approach to Experimental Results

During the actual experimental engine tests, the FAP measured the surface pressure at the three sensing locations. The measurements were taken by the data acquisition (DAQ) system at a rate of 1 kHz, which was sufficient to resolve NGV wake passing phenomena. When examining spatially-resolved data, fluctuations in the experimental measurements will always be present. Some of these fluctuations may be attributed to actual physical phenomena occurring in the turbine, but others may simply be noise carried through the DAQ system. In order to remove some of the high frequency noise, the raw data can be processed using a low-pass filter in the initial stages of data reduction. This will more easily allow for identification of NGV wake passing phenomena in the processed data. An example of the filtered pressure measurements taken at the three sensing locations on the FAP while it was moving circumferentially on

the translator is included in Figure 6.2. These pressure measurements were taken over the entire run and a time transient period can clearly be seen prior to the beginning of the FSTI at 500 ms.

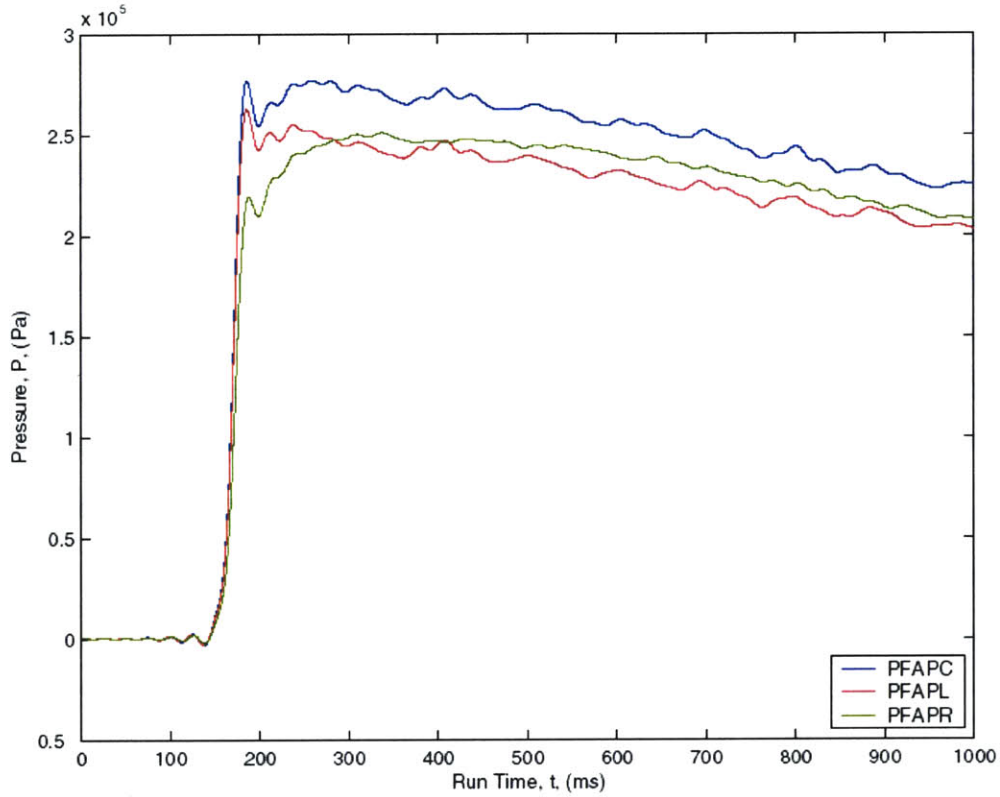


Figure 6.2: Filtered Flow Angle Probe Pressure Measurements with Run Time, T222

The filtered pressure measurements taken by the FAP were used to infer the tangential flow angle in the local flow field at the rotor blade exit in the turbine test section. This was done by evaluating the dimensionless pressure parameter, ψ , which was defined earlier as

$$\psi = \frac{P_L - P_R}{(P_C - P_L) + (P_C - P_R)} = \frac{P_L - P_R}{2P_C - P_L - P_R} \quad (6.1)$$

The non-dimensional parameter was then used in conjunction with the FAP tangential flow angle calibration curve, Figure 5.5, to determine the flow angle as follows,

$$\theta_{rel}(\psi) = m \cdot \psi + c \quad (6.2)$$

The values for the slope, m , and intercept, c , of the calibration curve are 0.160° and 17.519° , respectively. Recall that the calibration fit was performed on data in the range of -20° to 20° with respect to the probe head, and thus is only valid on that range. Data for test runs T231 and T232 did not meet this angle range requirement, and thus cannot be used in conjunction with the calibration fit described in the previous chapter. Both of these runs resulted in calculated flow angles greater than 30° , which is outside the useful range of the FAP calibration, and thus will not be included in subsequent analysis. It is important to note that the calibration will provide the flow angle with respect to the probe, $\theta_{rel}(\psi)$, which itself is installed with an offset with respect to the longitudinal axis of the test section. The FAP offset angle, θ_{offset} , for each test run is included in Table 6.1. This situation is illustrated below in Figure 6.3.

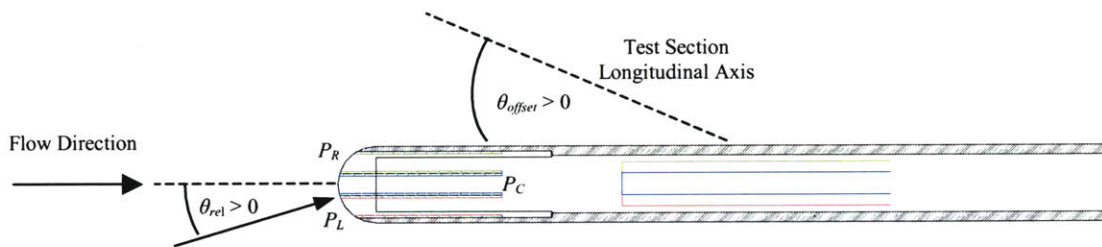


Figure 6.3: Flow Angle Convention with Offset for Flow Angle Probe

This offset angle must be added to the flow angle determined using Equation (6.2) in order to give the correct tangential flow angle in the test section. This can be expressed simply by

$$\theta = \theta_{rel} + \theta_{offset} \quad (6.3)$$

The use of Equation (6.2) and Equation (6.3) will have an impact of the propagation of uncertainties beyond those of the calibration that have already been presented.

Provisions for uncertainty analysis in the data reduction scheme will be discussed in the following section. As discussed above, the filtered, spatially-resolved measurements from the FAP combined with calibration data and plots will result in a plot of measured tangential flow angle with run time over the FSTI. An example of the measured spatially-resolved flow angle is included in Figure 6.4 below.

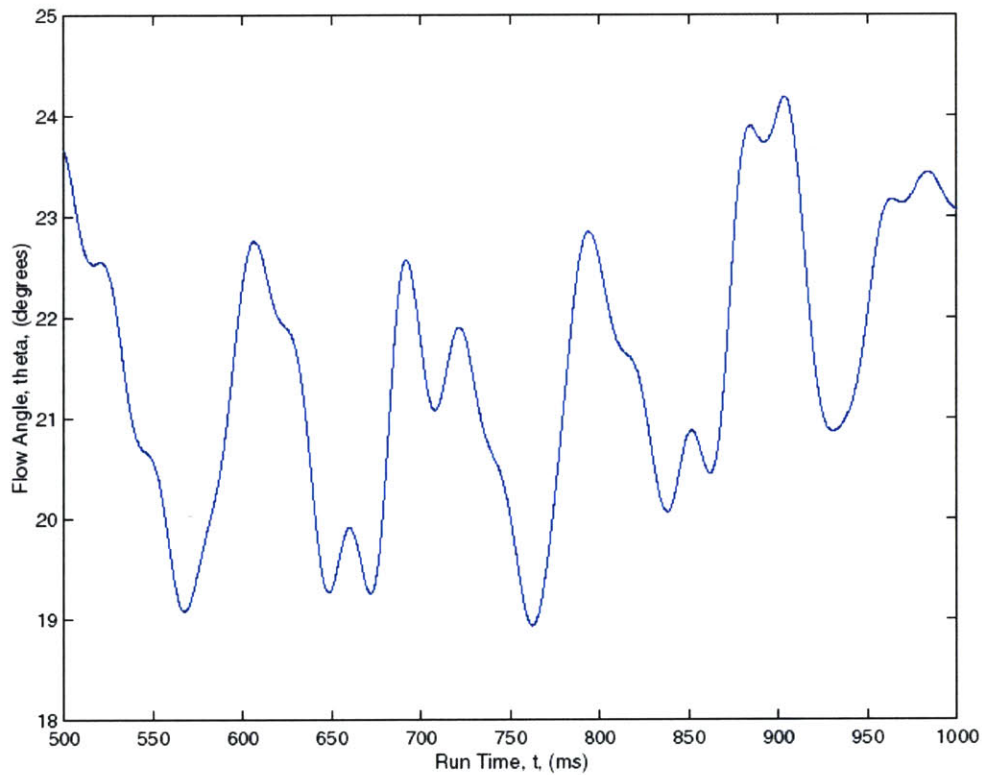


Figure 6.4: Flow Angle Measurement with Run Time, T222

The results included in Figure 6.4 do not include the appropriate error bounds associated with the analysis. Details of the uncertainty will be included in subsequent plots.

Figure 6.4 shows the rotor exit flow angle distribution along the circumference of the rotor. These variations are due to changes in pressure associated with NGV wakes, through which the FAP passes during the test. The next task in the data processing scheme is to determine an appropriate method of averaging the flow angle data.

It is desirable to obtain DC levels of the flow angle over a valid stage steady state time interval in order to provide useful averaged flow angle data for easy comparison between different test runs. When choosing an appropriate time interval, one must realize that the operating point of the turbine stage is continuously changing. The selected time interval should be short enough so that the operating point can be considered quasi-static. The operating point maps of the test runs, shown together in Figure 6.5, were examined to give an initial estimate of a suitable averaging and comparison window for the flow angle measurements.

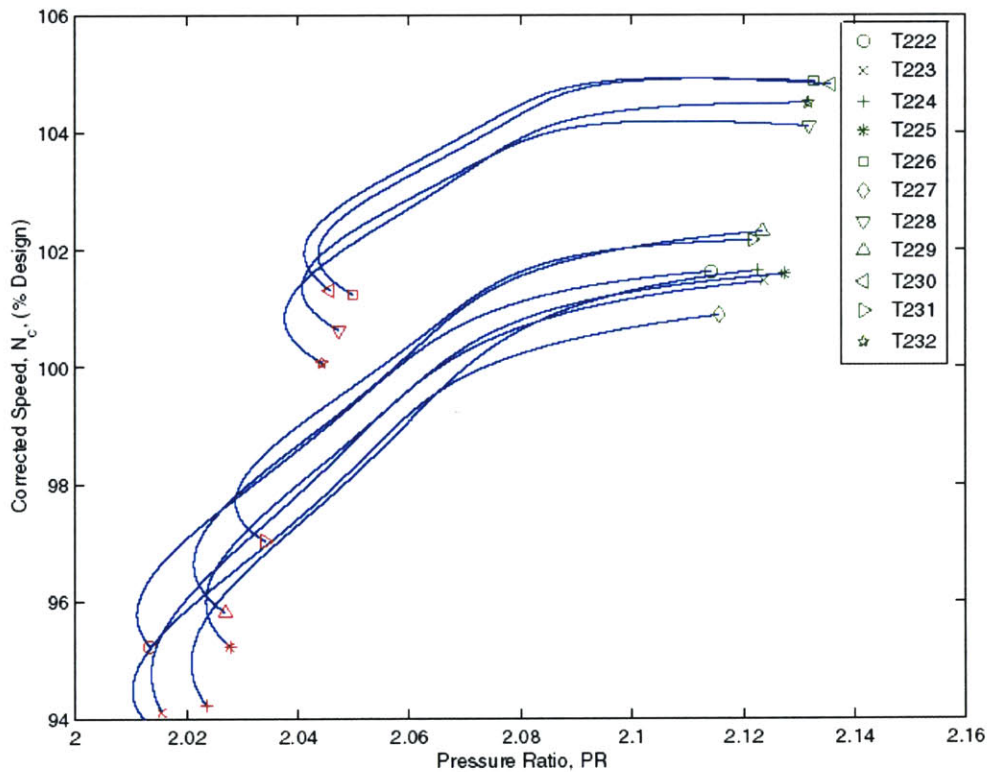


Figure 6.5: Turbine Test Run Operating Point Maps

In addition to examining the operating point maps of the test runs, a continuous sliding average over the FSTI of the measured tangential flow angle shown in Figure 6.4 was used to determine a suitable data-averaging window for the FAP. The sliding average was intended to compute the average flow angle based on a number of data points on either side of the time point for which the average was being calculated. The spatially-resolved flow angle distribution shown in Figure 6.4 shows a periodic response with fluctuations in the measured flow angle. Ideally, the averaging technique should take this into account and ensure that only one cycle is included in each average. This would mean that an average is taken over a time period corresponding to a single NGV pitch passing, which offers the effects of only a single wake. In order to do so, the time period of the FAP passing one of these NGV wake fluctuations must be known. The spatially-resolved data must be averaged using a time period because raw data is presented with respect to run time, rather than with respect to circumferential FAP position. Data for each test run, similar to that shown in Figure 6.4, was analyzed with an automated computer function that estimates the power spectral density (PSD) of a time signal. Peaks in the PSD correspond to frequencies prevalent in the data. General trends in the flow angle data were removed prior to performing the PSD estimate so that peaks at extremely low frequencies would not be dominant. A sample of the PSD of the flow angle data in Figure 6.4 is included below in Figure 6.6.

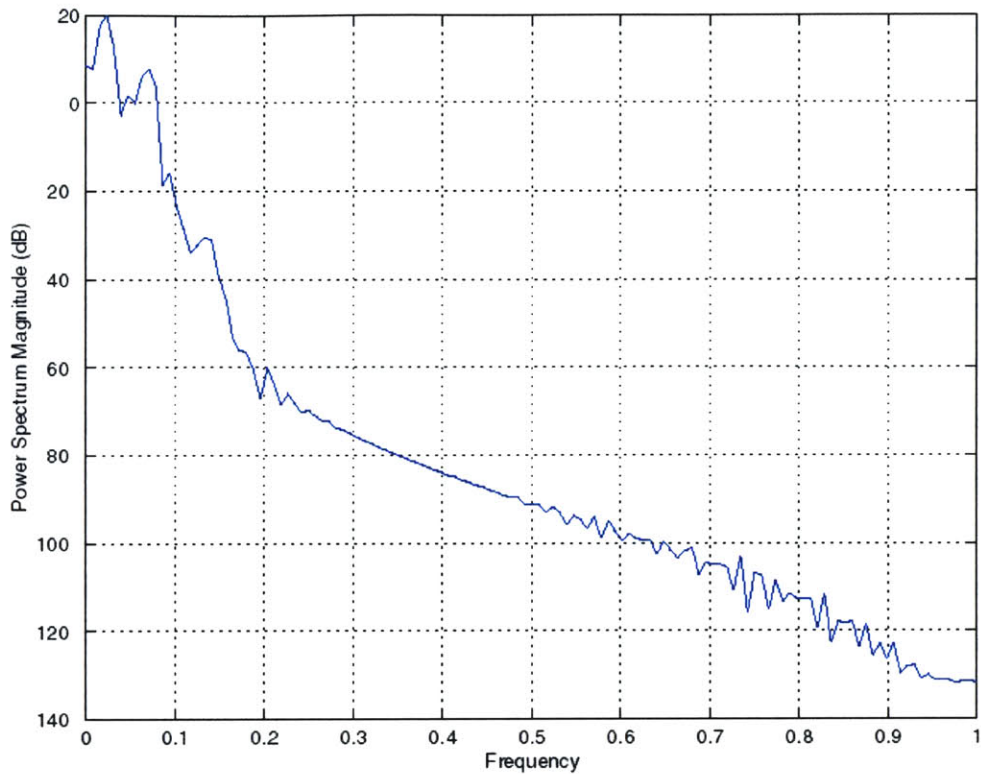


Figure 6.6: Measured Flow Angle Power Spectral Density, T222

The PSD shown in Figure 6.6 is representative of each test run. All show a clear peak at a frequency value of approximately 0.0234. It is important to note that the frequencies quoted on the abscissa are actually fractions of the Nyquist frequency, which is one-half of the data sampling frequency. The sampling frequency for these experiments is 1 kHz, giving a corresponding Nyquist frequency of 500 Hz. Thus, the frequency of the repeating fluctuations observed in the measured flow angle data is approximately 11 Hz. As a result, a time period of 90 ms was used in computing the sliding average of the data. The significance of the frequency peak of 11 Hz that can be observed in the PSD plot of the measured data with respect to NGV wakes will be discussed further in subsequent sections. Figure 6.7 shows the spatially-averaged flow angle data computed using a sliding average of the data in Figure 6.4. Also included in Figure 6.7 are the polynomial fits of corrected speed, N_c , and pressure ratio, PR, over the FSTI.

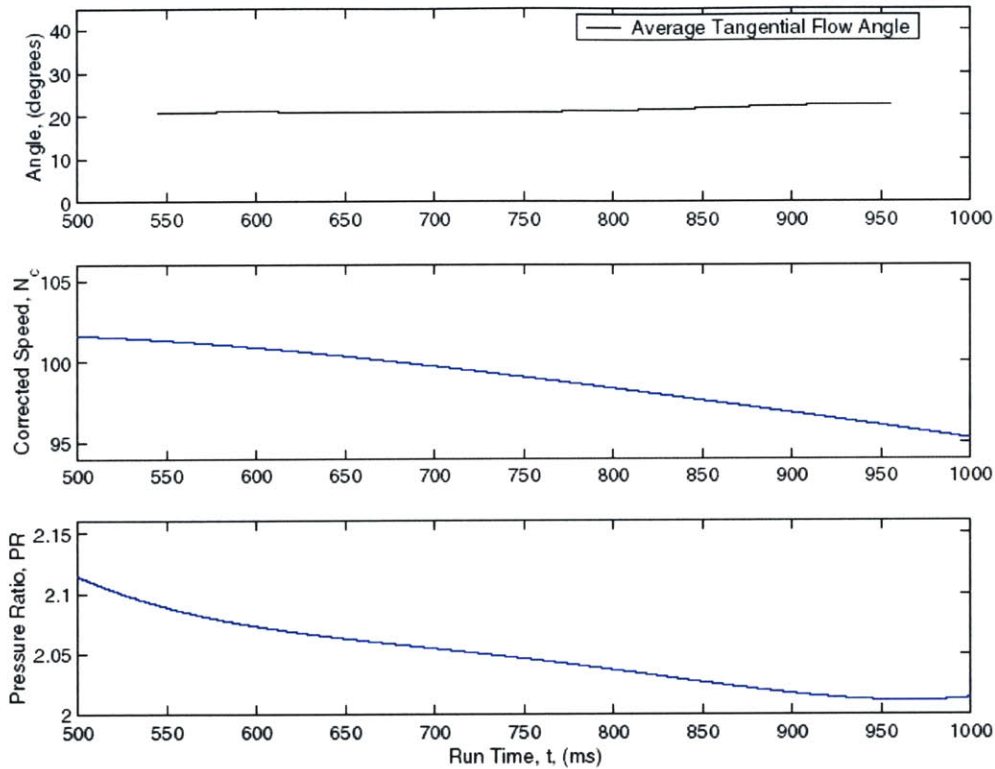


Figure 6.7: Spatially-Averaged Flow Angle, Stage Corrected Speed, and Stage Pressure Ratio with Run Time over FSTI, T222

Once again, the plots shown in Figure 6.7 are representative of those for each test run. The spatially-average flow angle values are relatively constant, especially in the earlier stages of the FSTI. For the experimental runs conducted, the time period that was chosen to give a suitable data-averaging window was 600-650 ms, which falls within the FSTI. DC values for the experimental measured flow angle values will be quoted over this interval, as will corresponding averaged values of turbine stage corrected speed and pressure ratio. It is important to include these turbine operating point parameters in any averaged analysis in order to determine how consistent the turbine operating point was kept between runs. The choice of a suitable data-averaging window allows both spatially-resolved and spatially-averaged tangential flow angle data to be presented and discussed in subsequent sections on experimental results.

One important point of note with respect to the average flow angle data presented above is with reference to useful turbine performance measurements. Perhaps the most

significant performance quantity that could be derived from an instrument such as the FAP is the angular momentum flux of the flow leaving the rotor. However, one must realize that the spatially-averaged flow angle measured is not directly representative of an average of the momentum flux because of the changes in flow velocity through the NGV wakes. Thus, in order to calculate a similar average of the momentum flux one would also require accurate spatially-resolved flow velocity values.

6.5 Experimental Error Analysis

Results derived from data collected from experimental activities are not complete unless the uncertainty in quoted values is also included. A realistic uncertainty calculation is required to validate experimental results. The propagation of error through the calibration of the FAP has already been discussed in the previous chapter, ultimately resulting in uncertainty bounds on the calibration coefficients. These errors must also be carried through to the final result in the data reduction schemes used on experimental measurements. The procedure by which the remainder of the uncertainty propagation is carried out is discussed here.

The error in the tangential flow angle measured by the FAP can be determined by incorporating the general uncertainty propagation techniques previously outlined in Equation (5.8). The absolute random uncertainty in the flow angle with respect to the FAP as calculated using Equation (6.2) is given by

$$U_{\theta_{rel}}^2 = m^2 U_{\psi}^2 + \psi^2 U_m^2 + U_c^2 \quad (6.4)$$

An expression to account for the uncertainty in the offset angle used when the mounting of the FAP, θ_{offset} , must also be included. The final equation employed in data reduction to determine the tangential flow angle accounting for the FAP offset is Equation (6.3). The following expression allows the absolute uncertainty in the FAP offset, $U_{\theta_{offset}}$, to be included in the error for the final calculated flow angle value,

$$U_{\theta}^2 = U_{\theta_{rel}}^2 + U_{\theta_{offset}}^2 \quad (6.5)$$

The value for the uncertainty in the offset angle in the FAP mounting, θ_{offset} , used in the analysis of test data was 0.2° , which stems from the estimated error in the manufacturing of the aluminum alignment block used.

The propagation of uncertainty discussed in Chapter 5 and above culminates in error bounds being applied to the measured spatially-resolved tangential flow angle data as previously shown in Figure 6.4. The uncertainty in the measured flow angle will be slightly different for each data point because the error is dependant on the absolute pressure measurements taken, which are constantly changing. Spatially-averaged flow angle data will also have an associated uncertainty value. A reasonable value can be obtained by examining the spatially-resolved uncertainty calculated using the methods above. After reviewing the data from all of the test runs, a reasonable estimate of the absolute random uncertainty in the calculated spatially-averaged flow angle data is approximately $\pm 0.25^{\circ}$, which is the same order of magnitude as the absolute random uncertainty of each flow angle measurement.

6.6 Design Operating Point Results

6.6.1 Measurement Repeatability

In experimental investigations, measurement repeatability is always of paramount importance. The ability to reproduce the results obtained under a specific set of test conditions gives added confidence to the methods employed in research of this nature. Two of the test runs carried out in this investigation, T223 and T224, were intended to have identical test conditions, both being carried out at the turbine design corrected speed and at a FAP radial position of 0.35 in. from the translator ring. These tests would be expected to have almost identical operating point conditions and yield very similar

measured results. The operating point maps of the two test runs over the FSTI are overlaid and included below for comparison of test conditions.

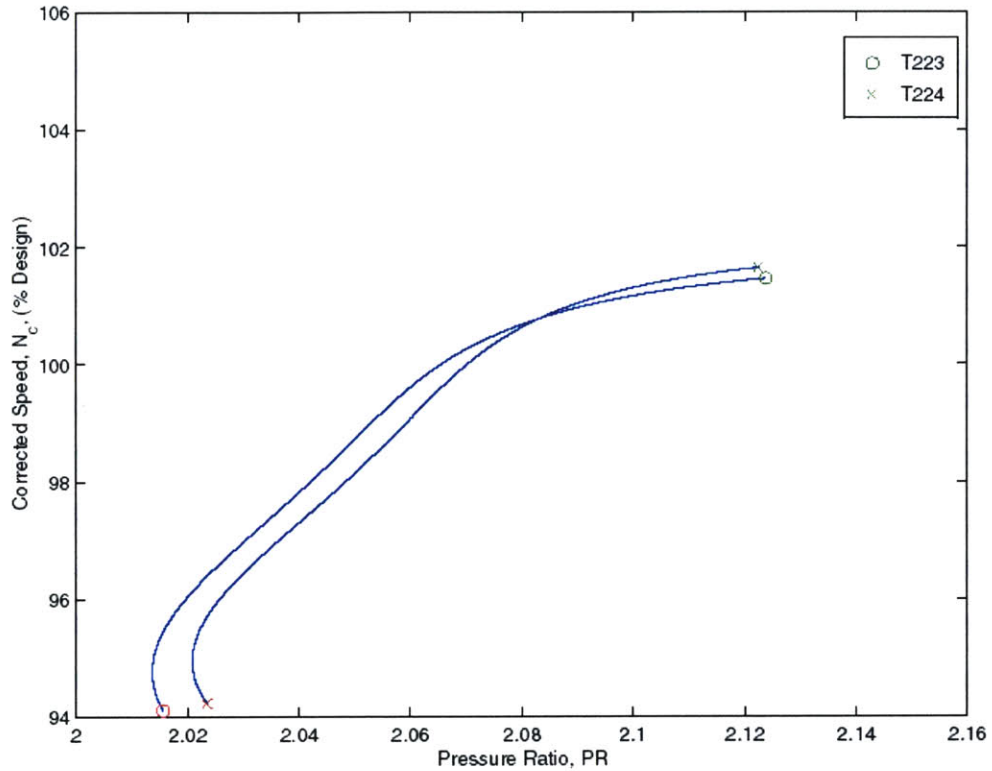


Figure 6.8: Stage Operating Point Maps, T223 and T224

Figure 6.8 shows the close similarity that exists between the two operating point maps. This is important because there can often be significant discrepancies between intended and actual test variables, which would cause variability in results. The spatially-resolved tangential flow angle measurements for these two runs are included in Figure 6.9 and Figure 6.10.

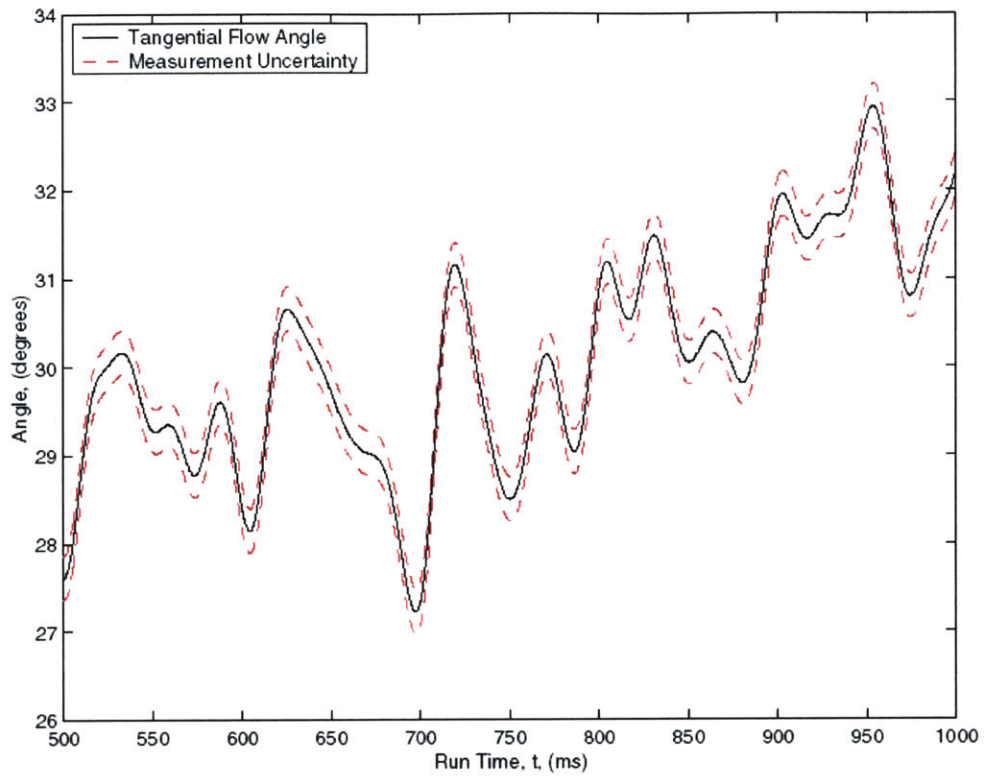


Figure 6.9: Flow Angle Measurement and Uncertainty Bounds with Run Time, T223

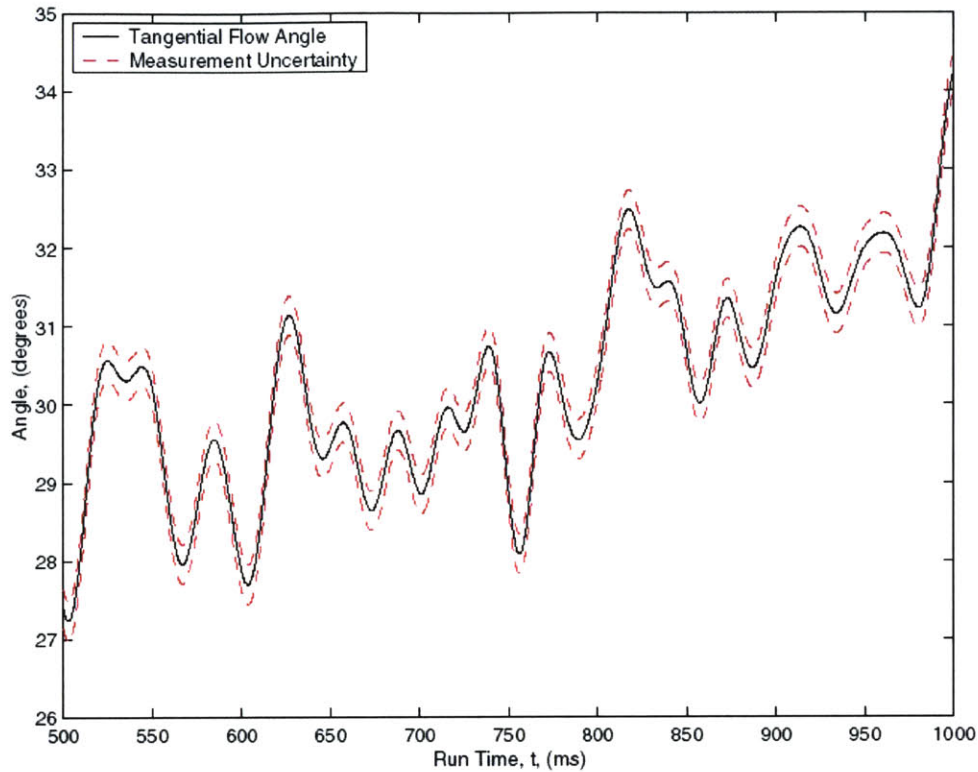


Figure 6.10: Flow Angle Measurement and Uncertainty Bounds with Run Time, T224

These two plots show that the spatially-resolved flow angle measurements of the two test runs follow the same general pattern. Similar periodic fluctuating trends due to NGV wake passing are seen to exist in both of the data sets. However, the degree of similarity between the two sets of results is somewhat difficult to assess from these plots alone.

Spatially-averaged data provides for an easier comparison of the two identical test runs at a glance. The sliding average performed on the measured flow angle is presented in Figure 6.11 and Figure 6.12. The plots also include the stage corrected speed and stage pressure ratio with run time over the FSTI.

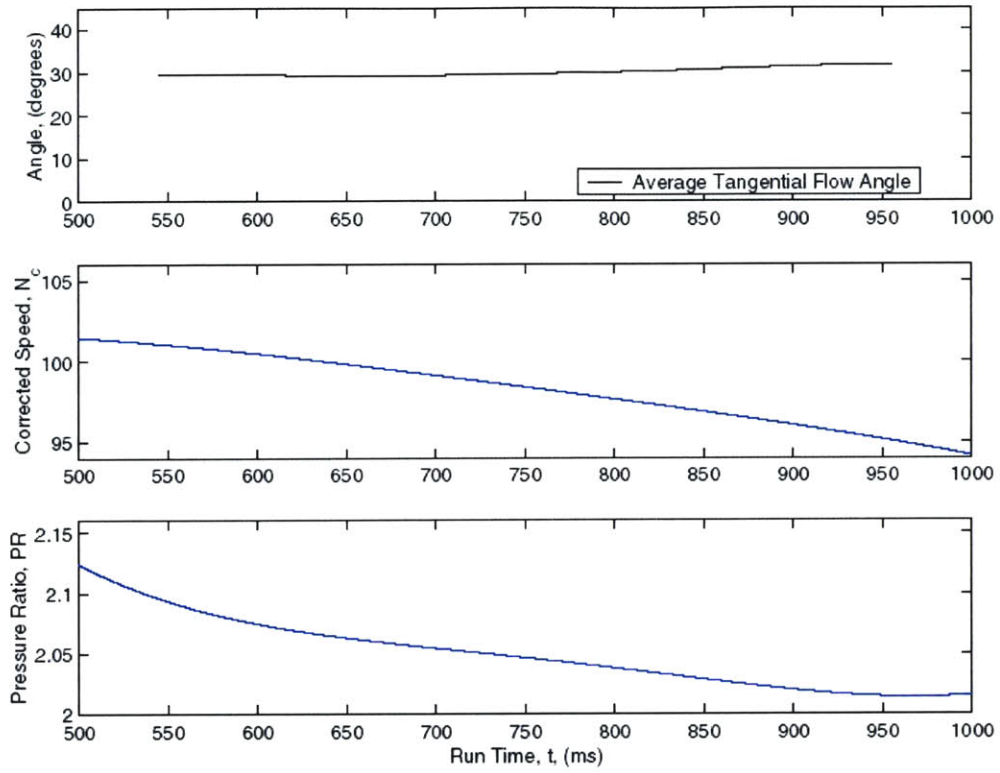


Figure 6.11: Spatially-Averaged Flow Angle, Stage Corrected Speed, and Stage Pressure Ratio with Run Time over FSTI, T223

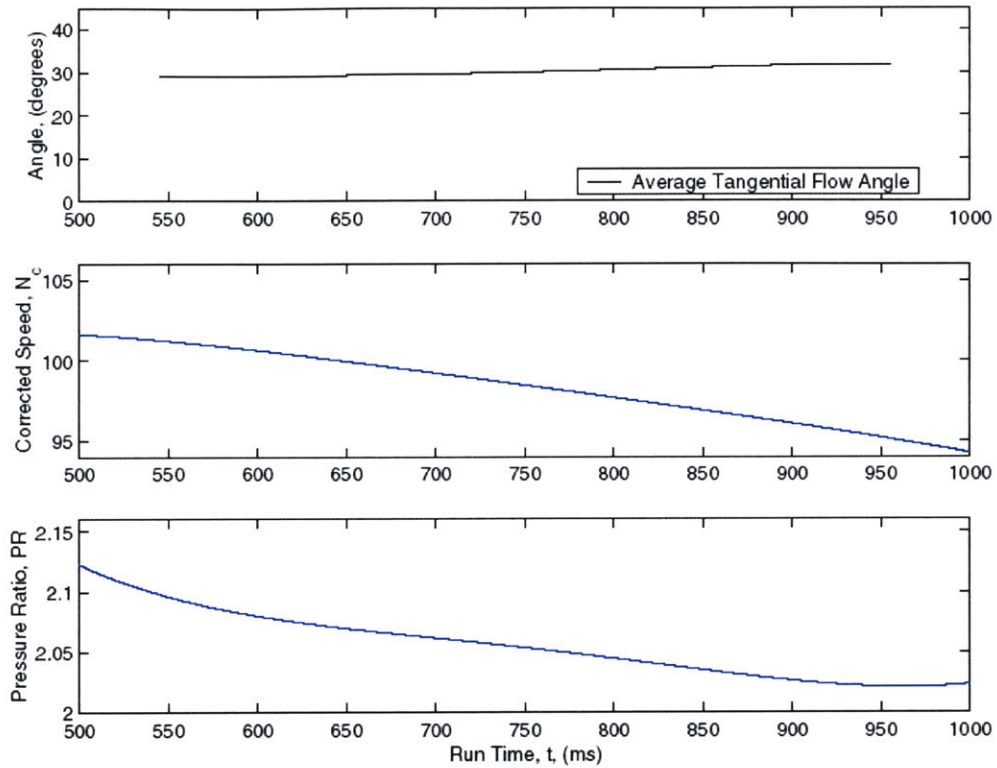


Figure 6.12: Spatially-Averaged Flow Angle, Stage Corrected Speed, and Stage Pressure Ratio with Run Time over FSTI, T224

The two plots of spatially-averaged flow angle above show extremely similar values and trends in the data over the FSTI. Also, the plots of stage corrected speed and stage pressure ratio show again the consistency that was obtained between the operating point variables. Spatially-averaged values for the tangential flow angle as well as the operating point variables over the time period of 600-650 ms are summarized in the following table.

Table 6.2: Measurement Repeatability Test Matrix

Test Number	FAP Radial Position from Translator Ring, (in.)	Average N_c , [% of design], (over t = 600-650 ms)	Average PR, (over t = 600-650 ms)	Average Measured Flow Angle, (over t = 600-650 ms)
T223	0.35	100.14	2.07	29.47
T224	0.35	100.29	2.07	29.35

The spatially-averaged data presented in Table 6.2 gives a much better representation of the repeatability of run conditions and results in tests T223 and T224. During the data-averaging period, the corrected speed was maintained within 0.30 % of the design point for the two tests. The average flow angles obtained over the time period being investigated were almost identical, especially when considering the reasonable estimate of uncertainty in the averaged measurements, which was estimated as $\pm 0.25^\circ$. This combined with the fact that the corrected speed and pressure ratio have been very closely reproduced lend a good deal of confidence to the experimental results as a whole.

6.6.2 Spatially-Resolved Measurements

The spatially-resolved data from design point runs can be examined to discuss the phenomena that result in observed fluctuations in the measured results. Test runs performed at five different radial locations in the turbine exit flow annulus and at design point corrected speed provide useful information for discussion. The operating point maps of the test runs, which were plotted together in Figure 6.5, allow for a comparison of the turbine operating point over the FSTI for these runs. A plot of spatially-resolved tangential flow angle with uncertainty bounds is included below for each of these five tests. Note that the figures are included in order of ascending radial position rather than test number, and that only one of the repeated tests discussed in the previous section is included.

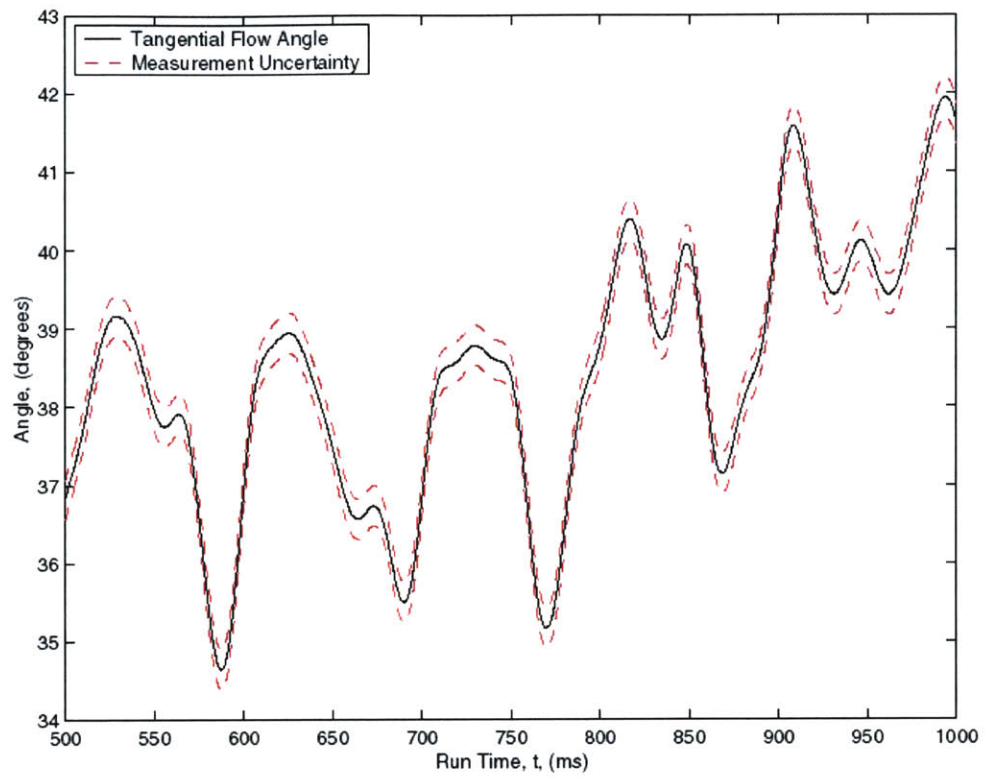


Figure 6.13: Flow Angle Measurement and Uncertainty Bounds with Run Time, R=0.15 in., T225

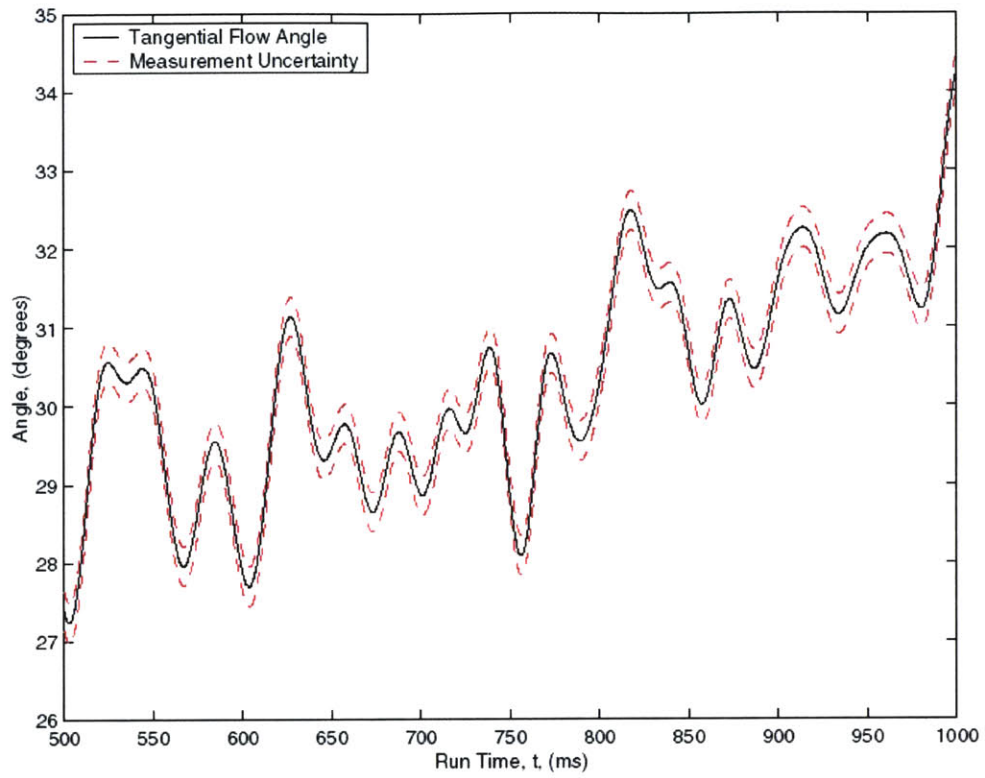


Figure 6.14: Flow Angle Measurement and Uncertainty Bounds with Run Time, R=0.35 in., T224

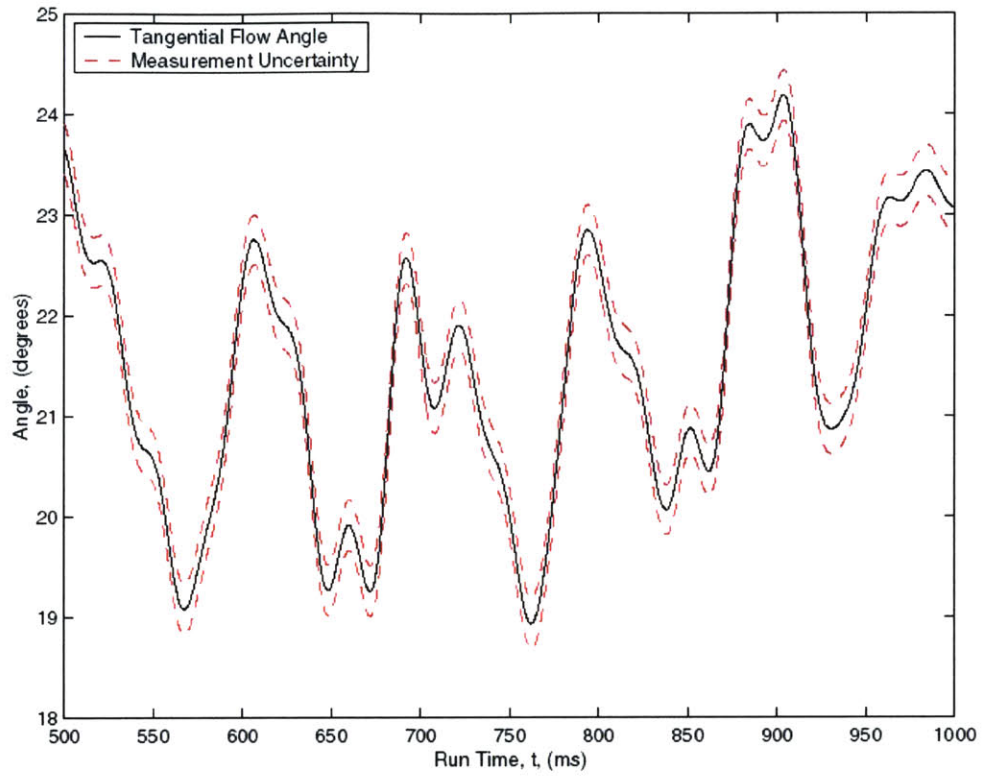


Figure 6.15: Flow Angle Measurement and Uncertainty Bounds with Run Time, R=0.54 in., T222

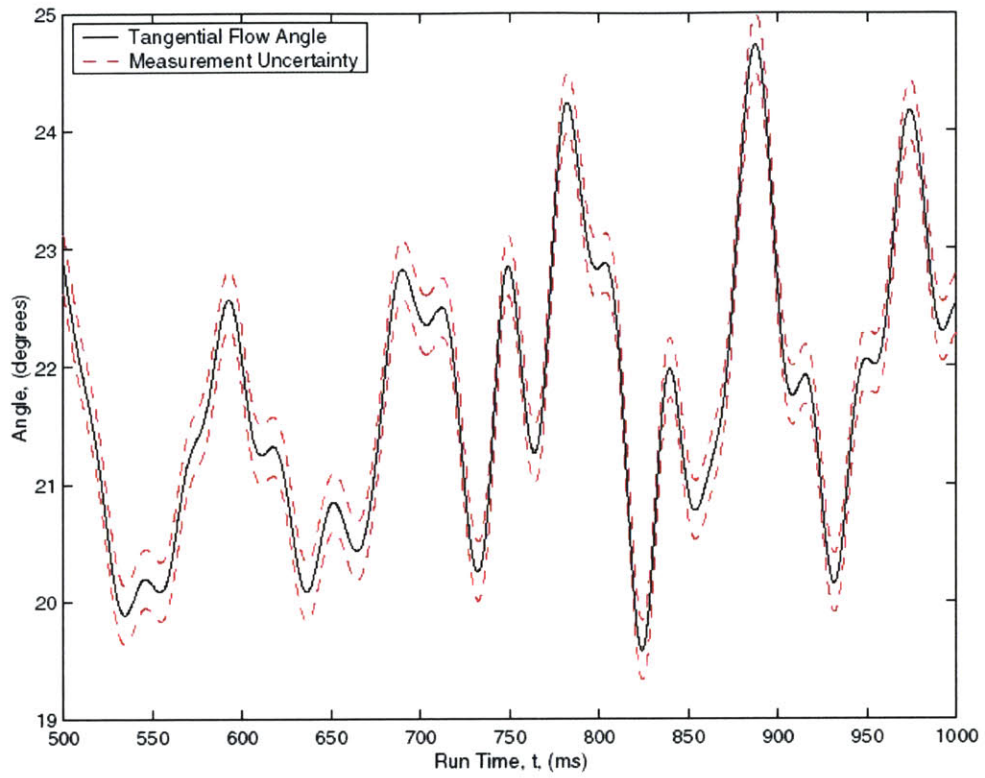


Figure 6.16: Flow Angle Measurement and Uncertainty Bounds with Run Time, R=0.75 in., T227

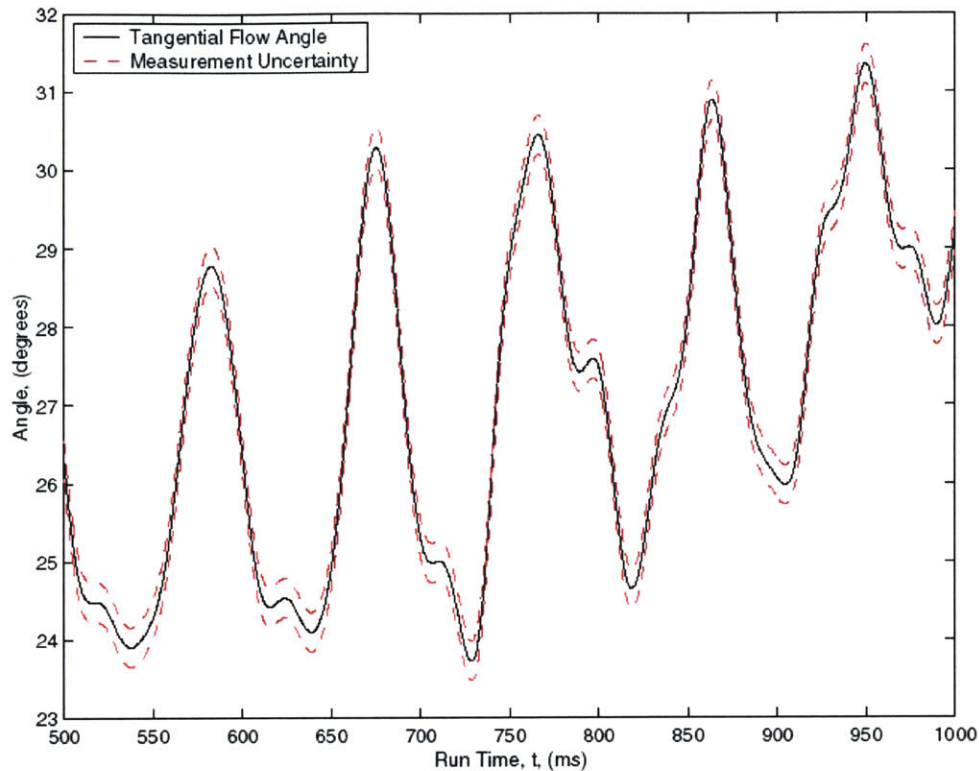


Figure 6.17: Flow Angle Measurement and Uncertainty Bounds with Run Time, R=0.94 in., T229

All of the plots included above appear to have some common characteristics. Although the absolute values of the flow angles in each plot are distinct, Figure 6.13 through Figure 6.17 all display a low frequency oscillatory response in the measured tangential flow angle. All of the plots also seem to show a slight trend of increasing flow angle over the FSTI. This trend can be attributed to the slight reduction in corrected speed during the runs, as seen from the operating point maps in Figure 6.5. An explanation of why the flow angle would change in this manner with corrected speed will be given when discussing the off design corrected speed runs later in this chapter. The uncertainty bounds on each of the plots varies slightly, but all have values of approximately $\pm 0.25^\circ$ about the calculated flow angle values throughout the FSTI.

Of all the characteristics mentioned above, that of the periodic fluctuations in the measured flow angle is most worthy of note here. When discussing the operation of the downstream translator in previous chapters, the existence of circumferential flow field

non-uniformities due to NGV wakes was identified. By rotating circumferentially behind the turbine stage, the translator allows for spatial resolution of the flow field through these wakes. There are a total of 44 nozzle guide vanes in the turbine stage and the downstream translator rotates at a constant speed of nearly 0.25 rps. Thus, during the FSTI from 500-1000 ms, any instrumentation mounted on the rotating translator will pass through 5.5 nozzle waves. This corresponds to a probe wake passing frequency of approximately 11 Hz [9].

The PSD plots for Figure 6.13 through Figure 6.17 each resemble that shown earlier in Figure 6.6. As mentioned earlier, the PSD function performed on the previously filtered flow angle data yields a low frequency peak corresponding to approximately 11 Hz. This is the same frequency at which the FAP is traversing through the nozzle wakes while the downstream translator rotates circumferentially during the test. Incidentally, one can also examine the flow angle plots above to see that approximately 5.5 total cycles can be seen during the FSTI. This is evident in Figure 6.17, where the cycles can clearly be seen. Each of these cycles corresponds to the translator moving the FAP through a complete NGV wake downstream of the rotor. The choice of data sampling by the DAQ was indeed sufficient to resolve the passing of the FAP through the nozzle wakes.

The circumferential non-uniformities in the measured flow angle behind the turbine are a result of flow field variations. The flow velocity in the absolute reference frame leaving a NGV and entering a turbine will be different inside and outside of the nozzle wakes. This will in turn result in different rotor-relative inlet velocities depending on the circumferential position with respect to the wakes. Different velocities entering the rotor will result in variable flow turning through the rotor and in turn several distinct exit flow angles in both the absolute and rotor-relative reference frames. It is this circumferential variation in rotor exit tangential flow angle that is seen in the spatially-resolved FAP data presented above. The fact that these fluctuations in measured flow angle can be seen on the plots above is a testament to the need for a device such as the translator when making aerodynamic measurements downstream of the turbine.

6.6.3 Spatially-Averaged Measurements

In order to map the tangential flow angle with radial position it is best to examine spatially-averaged run data for the design point corrected speed runs. Recall that five different FAP radial positions were successfully employed at the design point corrected speed. The sliding average performed on the data allows for the removal of the periodic fluctuations that were discussed in the previous section. This enables an easier comparison of data between test runs. The average tangential flow angle along with stage corrected speed and stage pressure ratio are plotted below over the FSTI. Once again, the tests are ordered by radial position from the translator ring as opposed to test number.

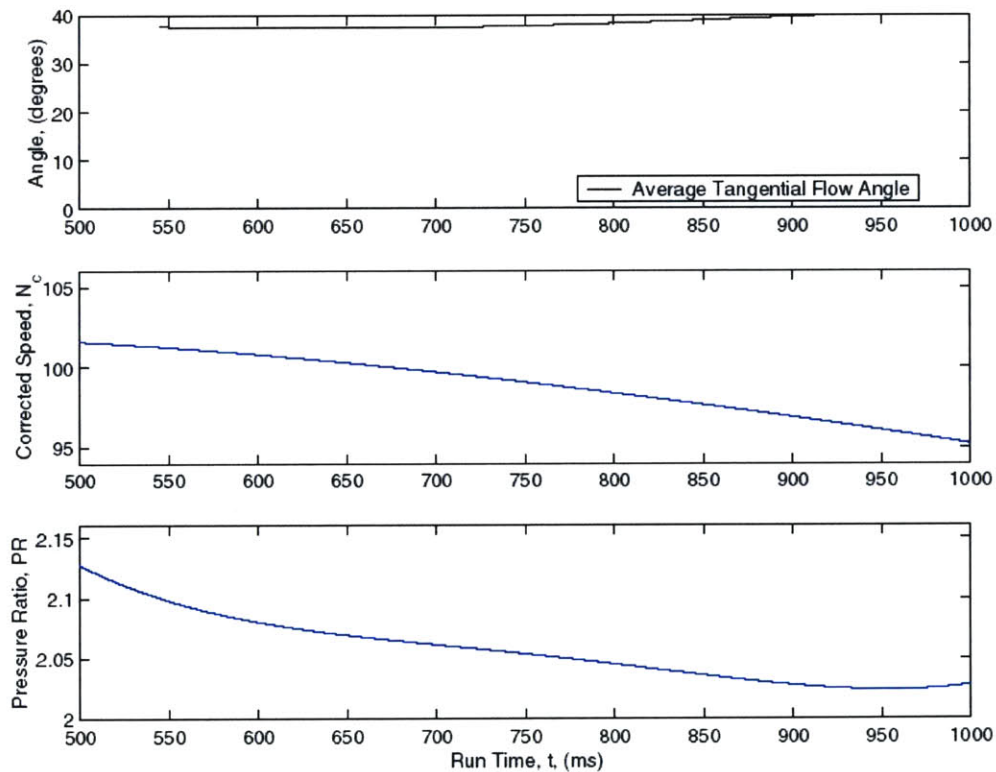


Figure 6.18: Spatially-Averaged Flow Angle, Stage Corrected Speed, and Stage Pressure Ratio with Run Time over FSTI, R=0.15 in., T225

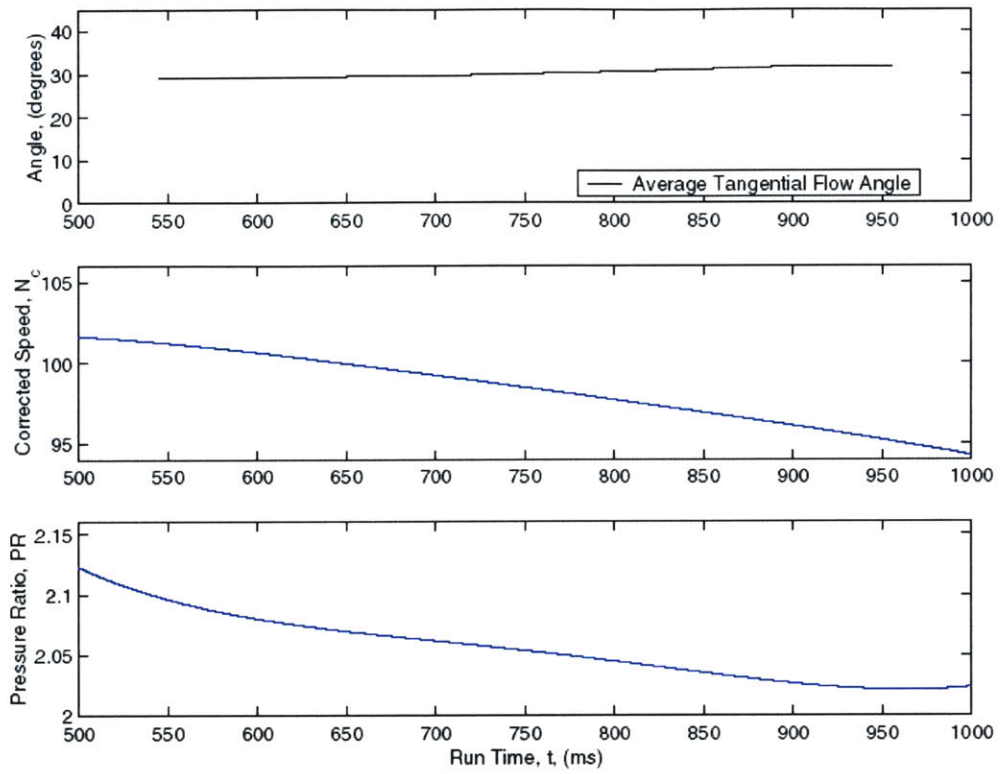


Figure 6.19: Spatially-Averaged Flow Angle, Stage Corrected Speed, and Stage Pressure Ratio with Run Time over FSTI, R=0.35 in., T224

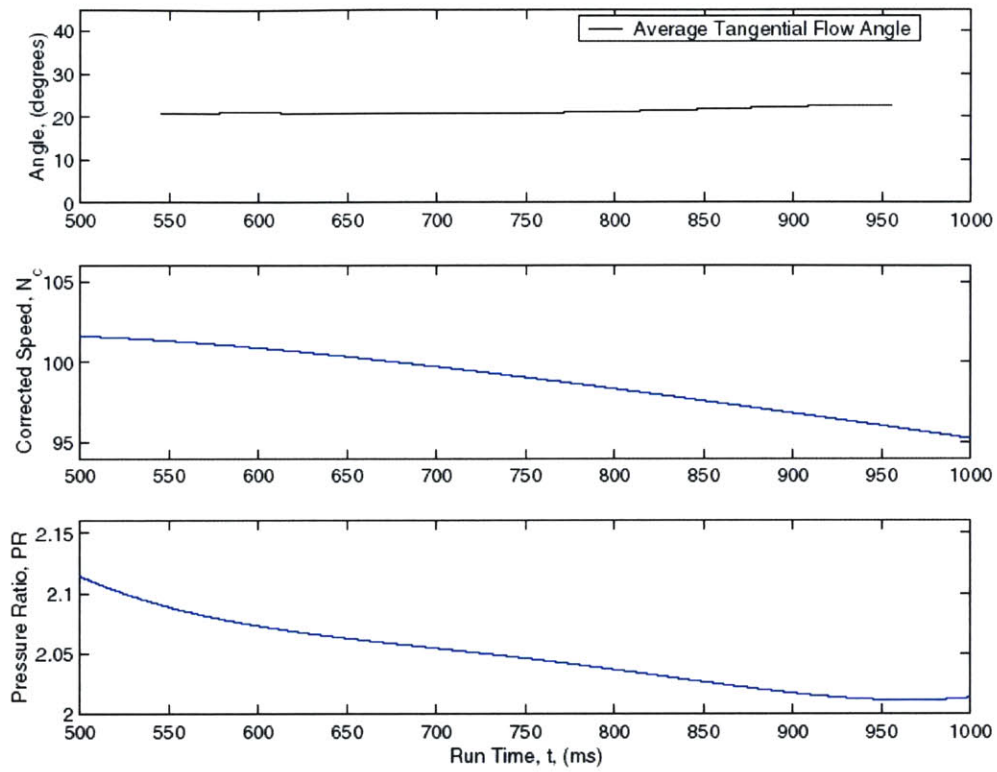


Figure 6.20: Spatially-Averaged Flow Angle, Stage Corrected Speed, and Stage Pressure Ratio with Run Time over FSTI, R=0.54 in., T222

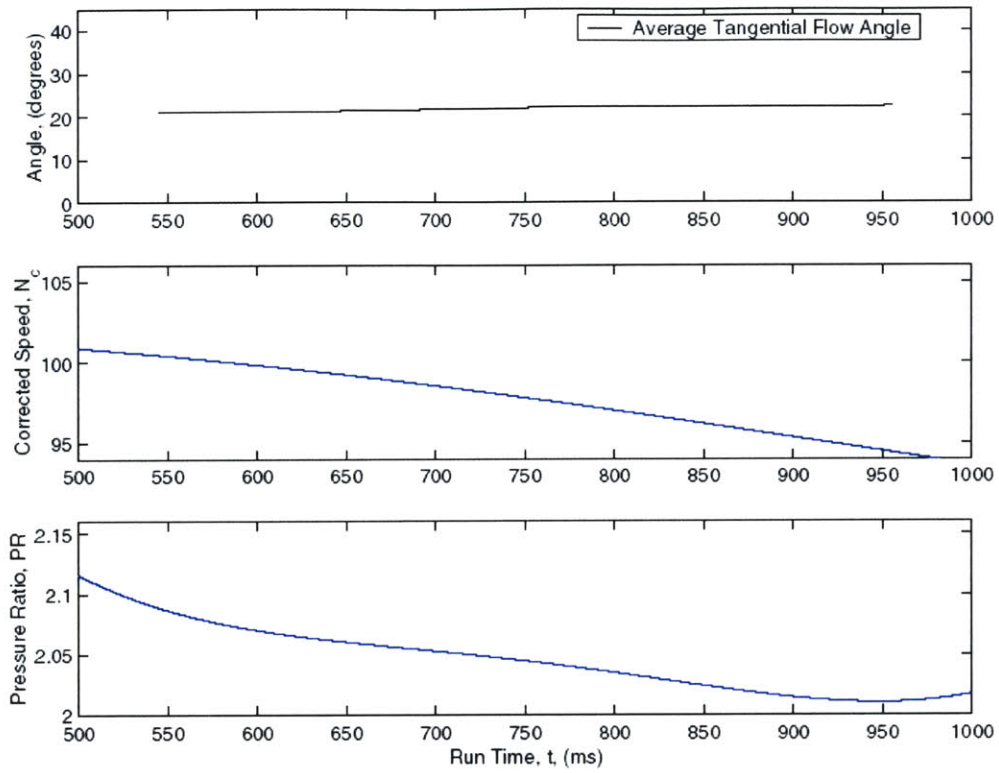


Figure 6.21: Spatially-Averaged Flow Angle, Stage Corrected Speed, and Stage Pressure Ratio with Run Time over FSTI, R=0.75 in., T227

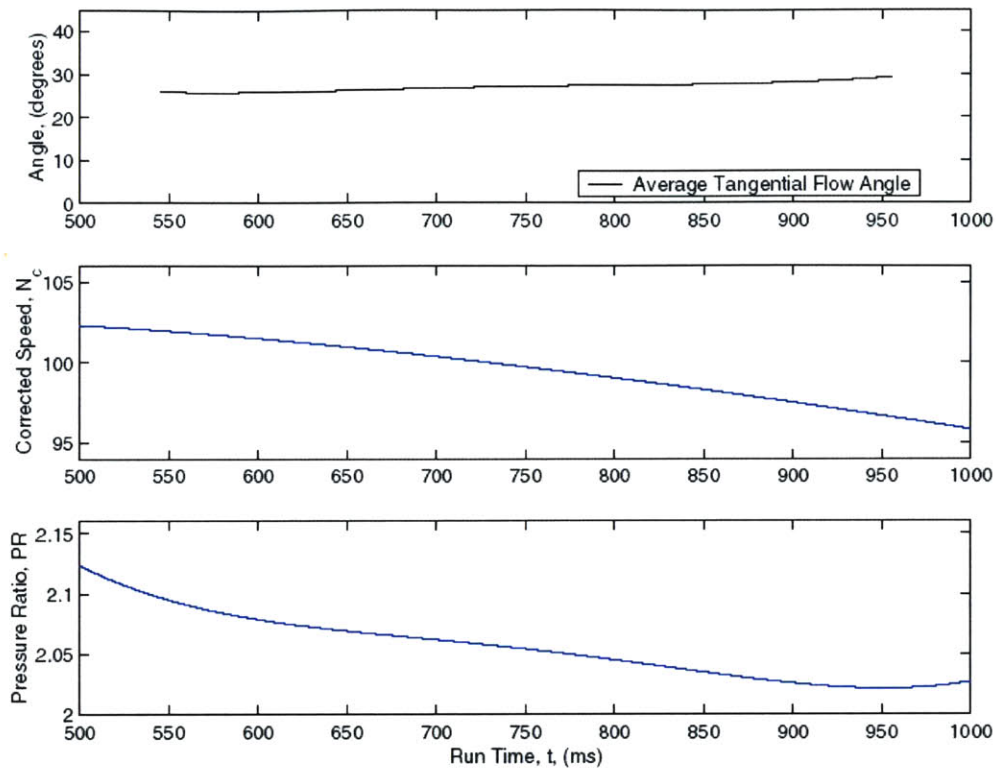


Figure 6.22: Spatially-Averaged Flow Angle, Stage Corrected Speed, and Stage Pressure Ratio with Run Time over FSTI, R=0.94 in., T229

Figure 6.18 through Figure 6.22 allow for a more direct comparison of average flow angle and operating point characteristics over the FSTI. Note the very consistent average flow angle measurements, showing only a slight increasing trend with test time, as was mentioned previously. The choice of the sliding average time period seems to adequately remove the periodic fluctuations, due to nozzle wakes, which were visible in the spatially-resolved data. The spatially-averaged data is best presented in tabular format over the pre-selected data-averaging window from 600-650 ms.

Table 6.3: Design Operating Point Test Matrix

Test Number	FAP Radial Position from Translator Ring, (in.)	Average N_c, [% of design], (over t = 600-650 ms)	Average PR, (over t = 600-650 ms)	Average Measured Flow Angle, (over t = 600-650 ms)
T225	0.15	100.55	2.07	37.45
T224	0.35	100.29	2.07	29.35
T222	0.54	100.61	2.07	20.89
T227	0.75	99.53	2.06	21.14
T229	0.94	101.23	2.07	26.06

Variations in average tangential flow angle with FAP radial position are clearly visible in Table 6.3. The differences in the flow angles for the runs shown are significant in comparison to the random uncertainty previously estimated for these spatially-averaged values. The data presented in the table can be compared to one and other because of the very small differences in the actual corrected speed and pressure ratio during the data-averaging window used.

In order to show how the average turbine exit tangential flow angle varies with annular radial position a plot can be constructed from the data in Table 6.3. Figure 6.23 is a plot of the average flow angle values with normalized radial position of the FAP. The radial positions quoted in the table have been normalized by the height of the annulus, 1.176 in., as determined from facility drawings. An additional point at a FAP radial position of 1.075 in. from the translator ring is also included with relatively large error bounds, and is denoted by a different symbol. This supplementary data point is from the data of test T231, which as mentioned earlier could not be considered as reliable as the other runs because the data exceeded the range over which the calibration of the FAP had been performed. However, the point is included to offer a rough estimation of where the average flow angle value might lie at this extreme radial position.

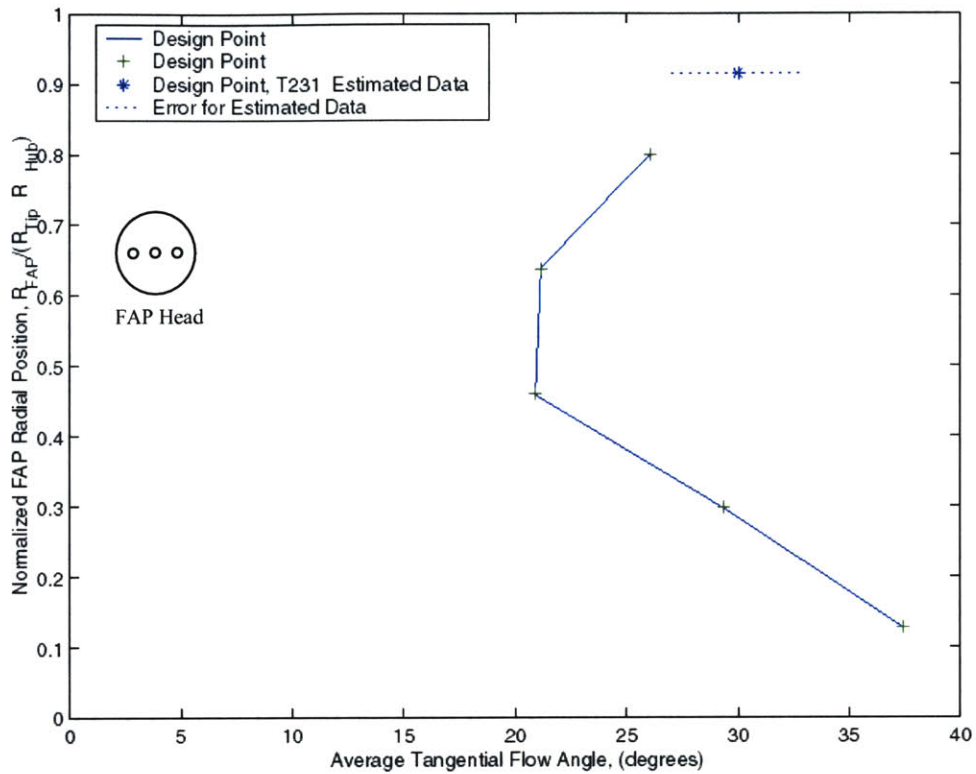


Figure 6.23: Average Turbine Tangential Flow Angle with Normalized Flow Angle Probe Radial Position at Design Operating Point, ($t = 600-650$ ms)

A scaled schematic of the end of the FAP head is also included in Figure 6.23 above. This offers an appreciation of the size of the instrument with respect to the annular height at the turbine exit. Flow angle data closer to the tip region would be useful in giving a complete picture of the physical situation. However, difficulties are expected as the probe is moved closer to the tip of the annulus because the probe head will likely pose more interference to the unique flow phenomena that occur in the tip region. Spatially-averaged flow angle data from the design point condition has offered insight into the spatial variations of the exit flow field in the test apparatus.

6.7 High Corrected Speed Results

Off-design operating point flow angle measurements were also obtained in this test series by running some tests at high corrected speed settings. Tests at three of the FAP radial positions used were carried out again with corrected speeds intended to be close to 105 %. For these tests, the pressure ratio was to remain constant at the design point value. Examining these turbine test runs can give insight into how the flow angle changes with corrected speed.

6.7.1 Spatially-Resolved Measurements

The spatially-resolved data from the high corrected speed test runs can be presented in the same fashion as for the design point runs. The operating point maps for each of these runs over the FSTI are included in Figure 6.5. A general comparison of the similarity of the test conditions for each of the runs can be made from this plot. Spatially-resolved flow angle data with uncertainty bounds over the FSTI are included below in Figure 6.24 through Figure 6.26. The data is presented in order of FAP radial position. Note that only three of the five radial positions that were presented in the previous section are included here at the high corrected speed condition.

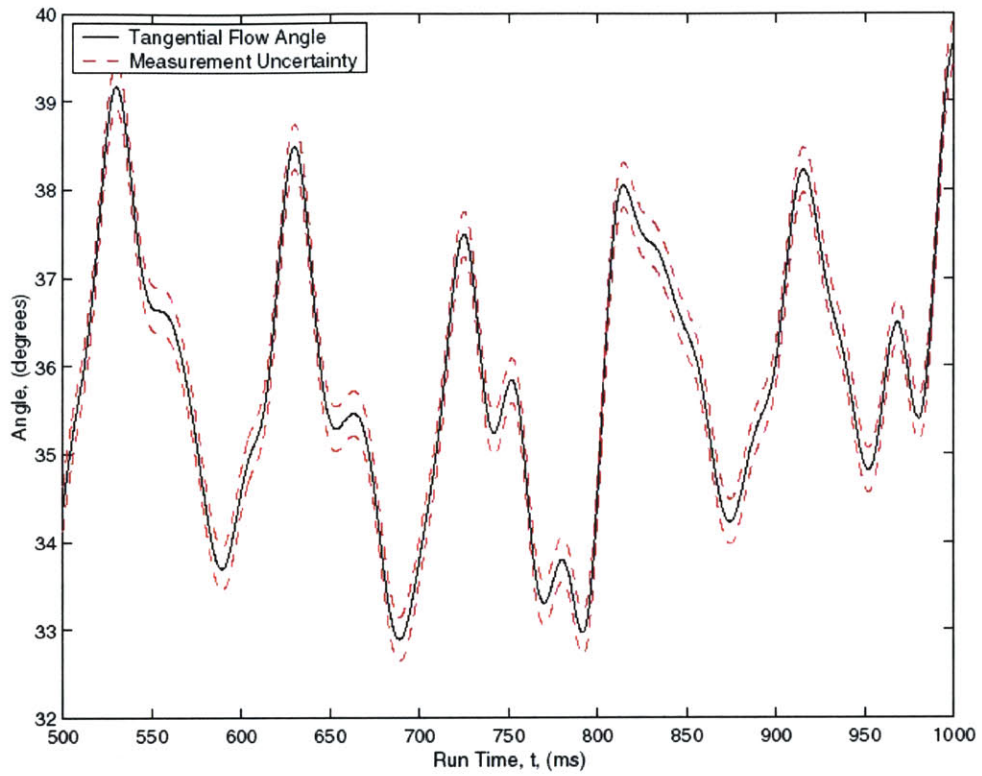


Figure 6.24: Flow Angle Measurement and Uncertainty Bounds with Run Time, R=0.15 in., T226

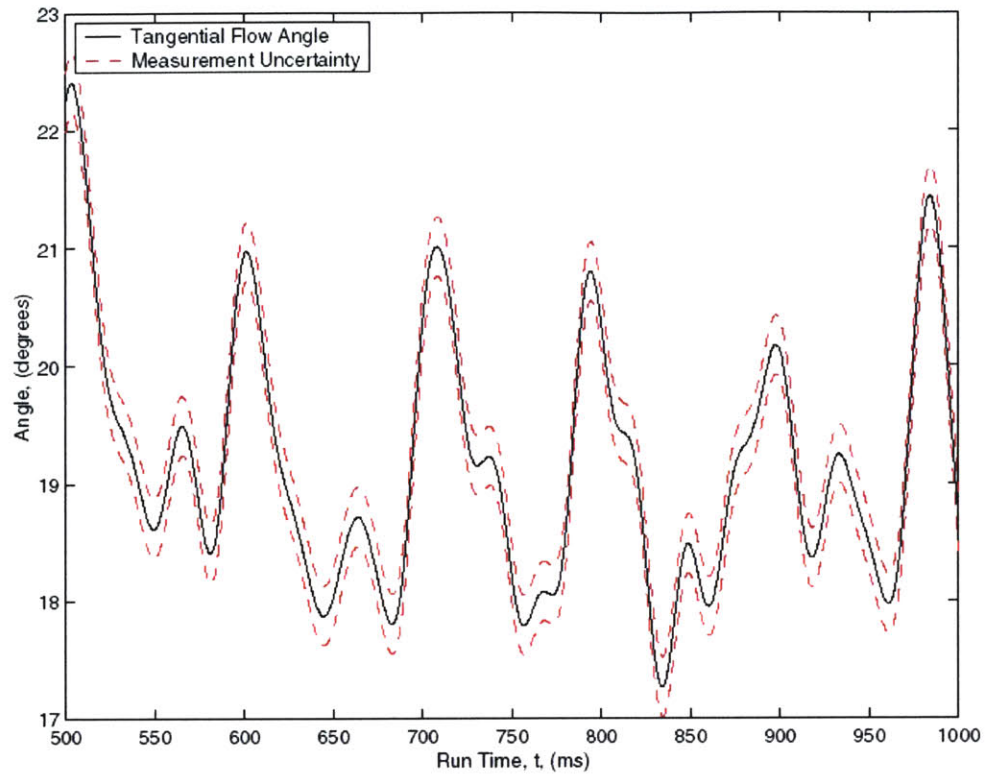


Figure 6.25: Flow Angle Measurement and Uncertainty Bounds with Run Time, R=0.75 in., T228

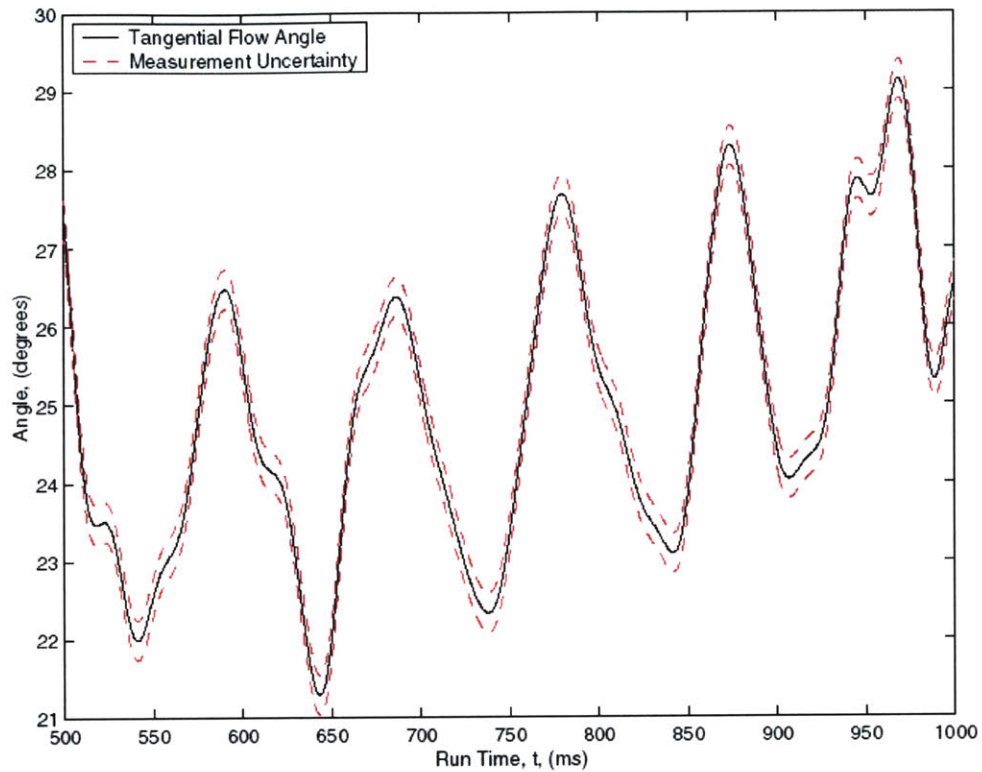


Figure 6.26: Flow Angle Measurement and Uncertainty Bounds with Run Time, R=0.94 in., T230

All of the spatially-resolved data plots included above have similar characteristics to those presented earlier for the design operating point runs. The periodic fluctuations at approximately 11 Hz are clearly visible. This is the most important feature that was evident in the spatially-resolved data presented. If these plots are compared to those created for their counterparts with identical FAP radial positions, a common discrepancy also begins to be revealed. After examining the spatially-resolved data shown here, the high corrected speed runs seem to consistently have a slightly lower average flow angle value than the design operating point runs. It will be much easier to see this trend when examining and comparing spatially-averaged data in the next section. The rationale behind this occurring during these tests will also be addressed in subsequent sections.

6.7.2 Spatially-Averaged Measurements

In order to better grasp trends in the experimental data that occur at high corrected speed settings, spatially-averaged data can be examined. Plots of the average tangential flow angle and stage operating characteristics over the FSTI are included below, as Figure 6.27 through Figure 6.29, for each of the three radial positions examined.

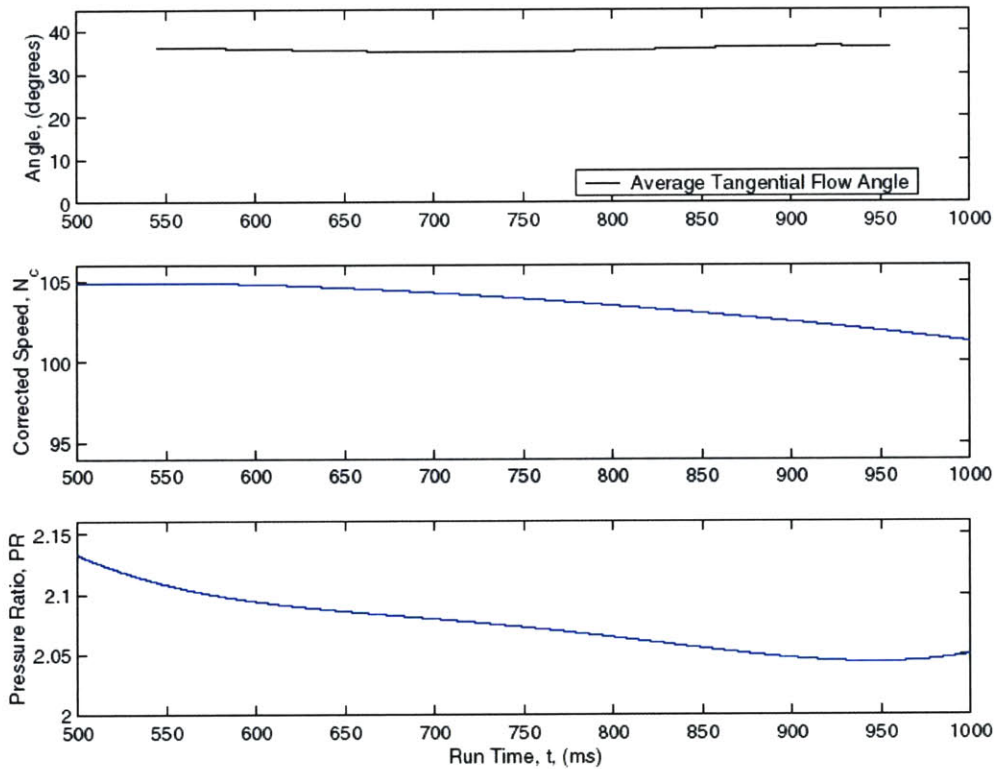


Figure 6.27: Spatially-Averaged Flow Angle, Stage Corrected Speed, and Stage Pressure Ratio with Run Time over FSTI, R=0.15 in., T226

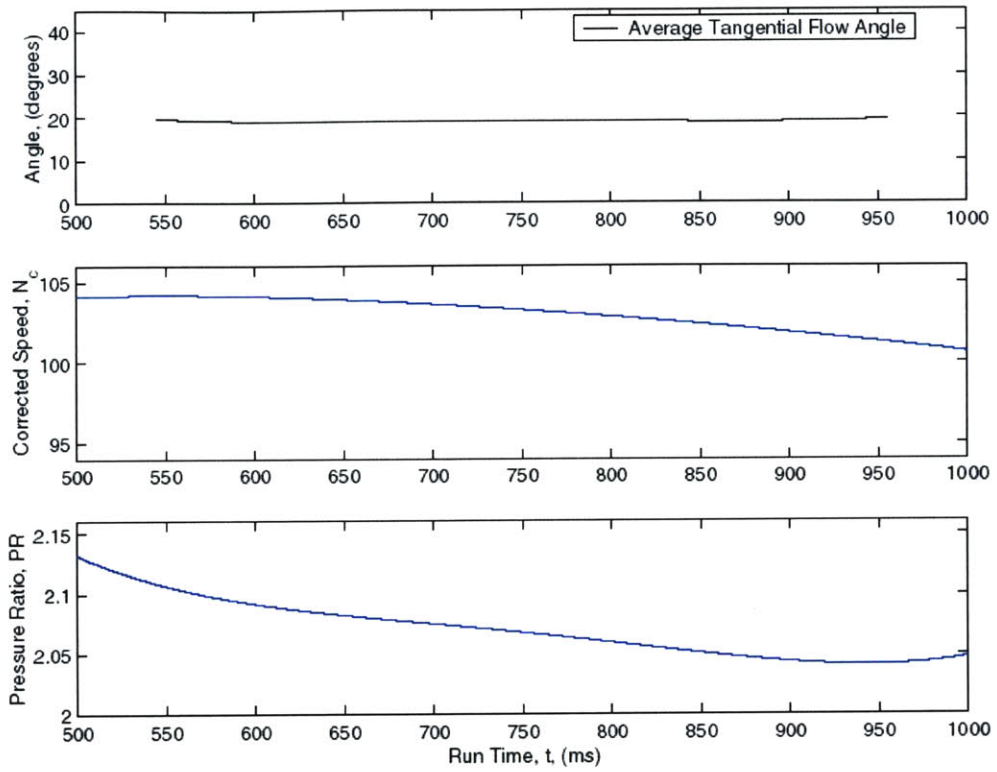


Figure 6.28: Spatially-Averaged Flow Angle, Stage Corrected Speed, and Stage Pressure Ratio with Run Time over FSTI, R=0.75 in., T228

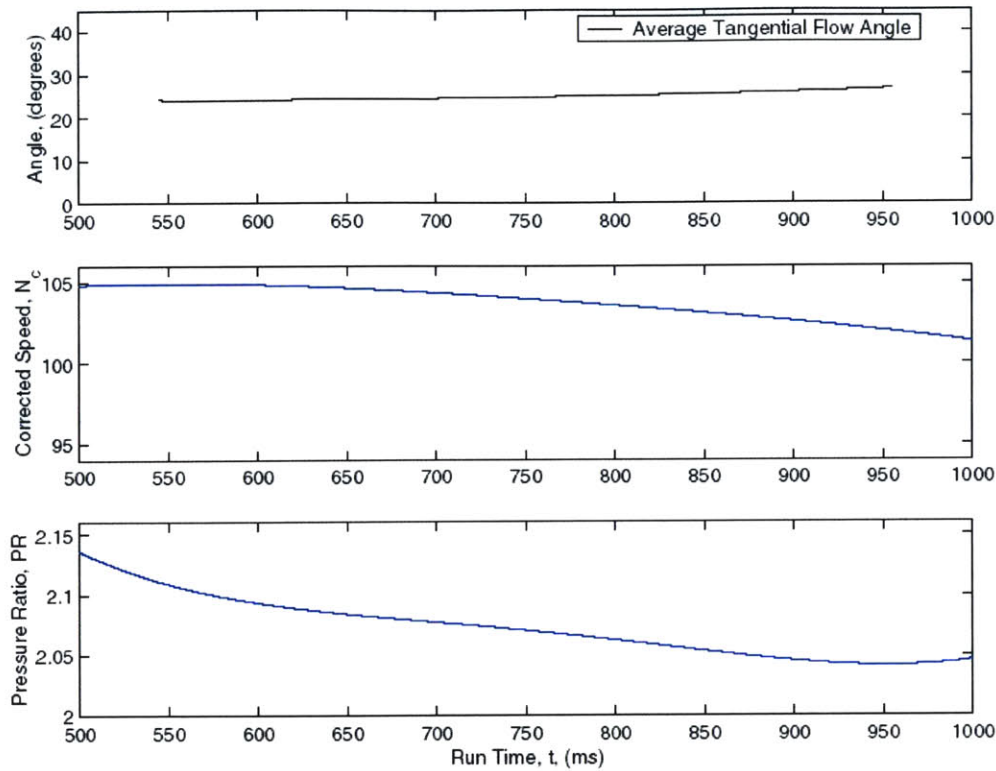


Figure 6.29: Spatially-Averaged Flow Angle, Stage Corrected Speed, and Stage Pressure Ratio with Run Time over FSTI, R=0.94 in., T230

As was noted with the spatially-resolved data, these tests tend to have a slightly lower average flow angle as compared to those carried out at the design operating point settings. In order to gain a better appreciation of this, a table of this data over the averaging window of 600-650 ms is included below.

Table 6.4: High Corrected Speed Operating Point Test Matrix

Test Number	FAP Radial Position from Translator Ring, (in.)	Average N _c , [% of design], (over t = 600-650 ms)	Average PR, (over t = 600-650 ms)	Average Measured Flow Angle, (over t = 600-650 ms)
T226	0.15	104.69	2.09	35.70
T228	0.75	104.01	2.09	19.02
T230	0.94	104.74	2.09	24.10

The data listed above shows that all of the three runs were carried out at nearly identical operating point conditions. The intended corrected speed setting was 105 %, which was very closely met for each test. The spatially-averaged data displayed in Table 6.4 can be

compared to that included in Table 6.3 to see that each of the high corrected speed tests gives an average measured tangential flow angle that is approximately 2° less than its design point counter part. This difference is indeed significant when compared to estimated random uncertainty of $\pm 0.25^\circ$ in the average flow angle values.

The difference in average flow angle between the design and high corrected speed runs can be explained by examining the velocity triangles at the rotor exit. An increase in the corrected speed of the stage results in an increased rotor mechanical speed, represented by (ωr) . The two schematics included in Figure 6.30 show how an increase in mechanical rotor speed from $(\omega r)_{Design}$ to $(\omega r)_{High}$ affects the relative and absolute tangential exit flow angles, θ and θ' respectively, from the rotor.

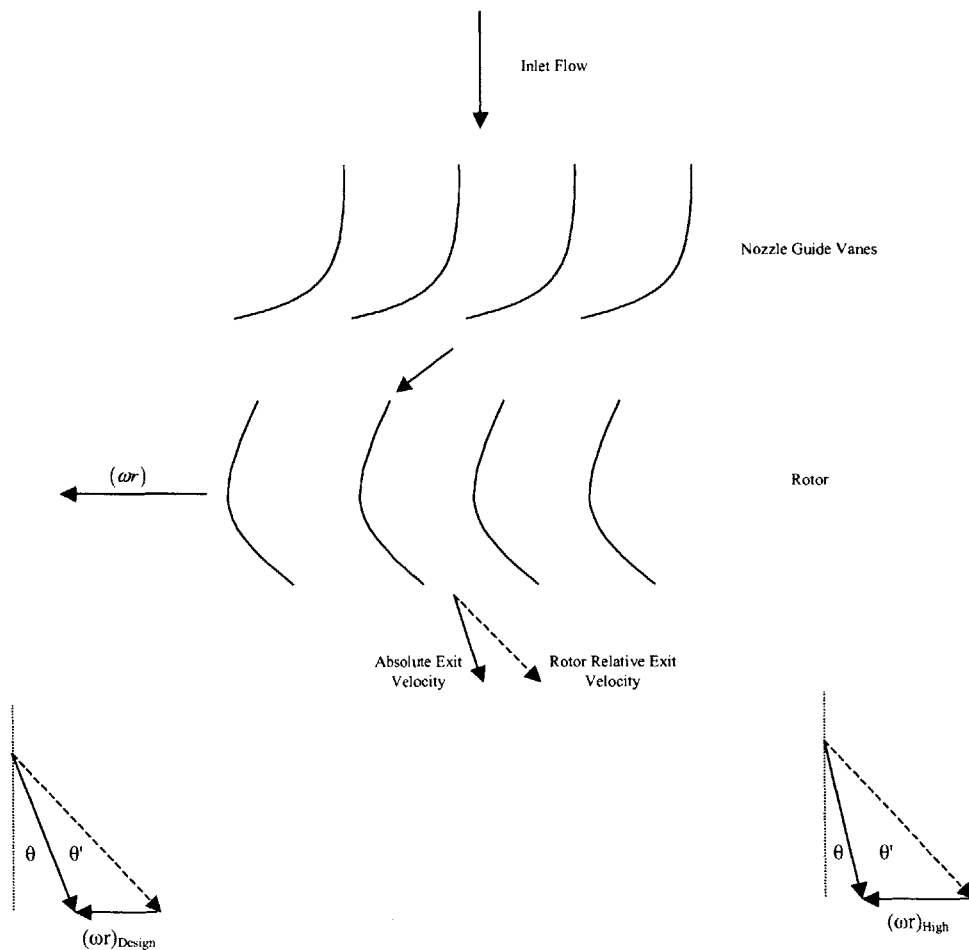


Figure 6.30: Rotor Exit Velocity Triangles for Design (left) and High (right) Mechanical Speed

It is clear that increasing the rotor mechanical speed serves to shallow the exit flow angle in both the absolute and relative frames of reference. This serves to explain the trend observed in the experimental results above. The schematic shown above also explains why a general increasing trend in flow angle was observed over all test runs as mentioned earlier. As the corrected speed decreases slightly over the FSTI, the flow angle will increase slightly.

Because only three FAP radial positions were included in the high corrected speed runs a complete radial map of the average flow angle cannot be made. However, the data that is available can be added to that displayed in Figure 6.23 to create a second such plot showing both the design and high corrected speed runs together in Figure 6.31. Once again, an additional data point for the radial location at 1.075 in. from the translator ring is included. This data comes from test T232, which is complimentary to test T231 included in Figure 6.23 as a supplementary data point. Once again, these extra points are only included to offer a rough estimation of the average flow angle at this location.

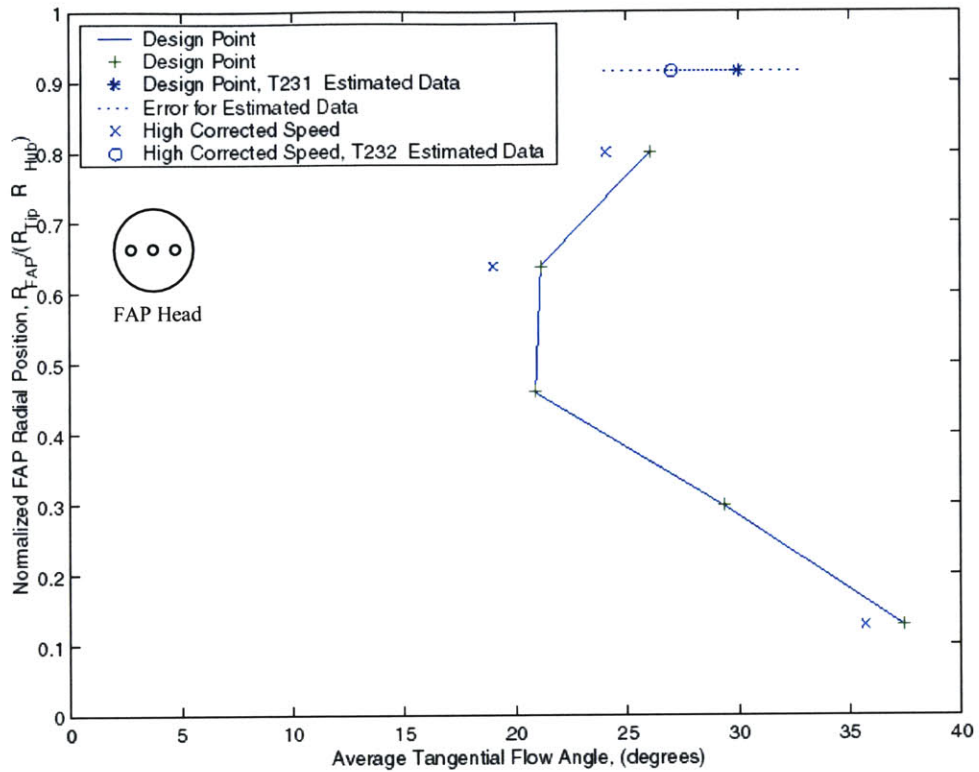


Figure 6.31: Average Turbine Tangential Flow Angle with Normalized Flow Angle Probe Radial Position at Design Operating Point and High Corrected Speed, ($t = 600-650$ ms)

Figure 6.31 illustrates that the high corrected speed average flow angle data lags that of the design point slightly. This is also the case for the additional test runs closest to the tip radius, which can only be displayed with estimated values of flow angle and random uncertainty. The plot suggests that the observed trend may exist over the entire annular height, however further experimental tests would be required to support such a claim.

6.8 Summary

Both spatially-resolved and spatially-averaged turbine exit tangential flow angle results over the FSTI have been presented in this chapter. An uncertainty analysis was also performed to provide error bounds for the measurements taken. Spatially-averaged data was examined and periodic fluctuations due to NGV wake passing were clearly

evident at a frequency of approximately 11 Hz, which is concurrent with the downstream translator operating parameters. Results for tests conducted at the design operating corrected speed and pressure ratio were given for five different FAP radial positions from the translator ring. Using a sliding average based on the observed period fluctuations in the data, spatially-averaged data was produced over the FSTI. The test period of 600-650 ms was chosen as a time comparison window for spatially-averaged data. Plots of flow angle with radial position were created to provide a rough map of the measured quantity. Results of tests conducted a high stage corrected speed were also examined. Increasing the stage corrected speed resulted in a reduction in tangential flow angle, as would be expected from an examination of velocity triangles. Better radial spatial resolution of flow angle data would be useful to augment these efforts.

Chapter 7: Conclusions and Recommendations

7.1 Review of Objectives

As discussed in Chapter 1, the primary objectives of this research effort involved developing instrumentation capable of aerodynamic and thermal performance measurements in a short-duration facility, and collecting experimental data of rotor exit flow angle in the turbine. More specifically, the objectives included:

- 1) The design and fabrication of an instrument capable of measuring the tangential flow angle in a short-duration test facility with adequate sensitivity and frequency response to resolve spatial flow characteristics associated with circumferential surveys
- 2) The calibration of the flow angle measuring device in a separate wind tunnel to allow for the experimental determination of flow angle from raw pressure measurements
- 3) The integration of the flow angle instrument into the existing downstream translator of the turbine test section with the provision varying the radial height of the probe once installed
- 4) The measurement of tangential flow angle downstream of the turbine rotor in the test section
- 5) The design of multi-layer, thin-film heat flux gauges capable of measuring heat transfer rates to turbine blades with sufficient frequency response
- 6) The development of new fabrication techniques for reliably manufacturing multi-layer, thin-film heat flux gauges

7.2 Summary of Work

An experimental study of the rotor exit flow angle of a fully scaled turbine stage was conducted. The flow angle was derived from three surface pressure measurements on a hemispherical-nosed flow angle probe (FAP). In addition to the filtered spatially-resolved data, spatially-averaged flow angle measurements were computed to determine the effect of varying the probe's radial position on the tangential flow angle.

The experimental tests were conducted in the MIT Blowdown Turbine Facility using a film-cooled turbine stage. The facility is a short-duration experimental apparatus capable of testing turbine stages under fully scaled conditions, producing useful data for comparison over a time period of approximately 500 ms for each test run. The FAP was designed to have sufficient frequency response to resolve certain unsteady characteristics in the turbine flow field. Prior to introducing the FAP into the turbine test section, a detailed calibration was carried out in order to relate measured surface static pressures to tangential flow angles via a non-dimensional pressure parameter. A detailed uncertainty analysis of the calibration was the beginning of a comprehensive error propagation procedure employed with test data.

Turbine tests were carried out at several FAP radial positions at the design operating point of the turbine stage. This allowed for radial mapping of the circumferential spatially-averaged flow angle measurements. In addition, some turbine test runs were carried out at high corrected speed operating conditions. Spatially-resolved results were taken to measure flow angle variations through nozzle guide vane (NGV) wakes. Periodic fluctuations observed in the measured flow angle with run time confirmed the expected variations through the NGV wakes. These fluctuations, which were observed to occur with a frequency of approximately 11 Hz, were due to the FAP passing the NGV wakes since the FAP was mounted on a rotating downstream translator for the turbine tests. High corrected speed test runs consistently showed lower spatially-averaged flow angle values than their corresponding design point tests. This is explained by the difference in rotor mechanical speed between these runs.

In addition, the design, development, and fabrication of multi-layer, thin-film heat flux gauges was a portion of this research work. These heat transfer gauges consisted of

thin nickel temperature sensors on either side of 25 μm thick polyimide (Kapton[®]) film. The fabrication of these gauges with the desired gauge geometry and material composition employed techniques including electroless nickel deposition, photomachining using an excimer laser, and electrolytic copper plating.

7.3 Recommendations for Future Studies

Several recommendations can be made to build and improve on the results reported in this thesis. Additional experimental testing can be carried out to duplicate all of the tests performed at the design operating point and at the high corrected speed condition. This would allow one to observe whether the trend of a slightly lower average flow angle with higher corrected speed holds for the remaining radial locations.

It would also be very useful to obtain flow angle data with the probe positioned at several locations close to the tip of the flow annulus. This would help to give a more complete map of the spatially-averaged flow angle with FAP radial position, which makes for easier comparison with theoretical calculations. In the short-term this would require merely running more test at several radial positions, but in the long-term it might require the design and fabrication of an even smaller FAP, if possible.

Additional testing could also be carried out to determine the effect of various other changes in operating conditions on the tangential flow angle at the rotor exit. This could include further varying the stage corrected speed and stage pressure ratio, or even performing experiments with different turbine tip gaps between the rotor and the tip casing.

In terms of the multi-layer, thin-film heat flux gauges, there is still a significant amount of future work to be performed in order to implement them in experimental testing. Practice is required in mounting these gauges to a metal test sample. This could be incorporated in calibrating the gauges with the data acquisition (DAQ) system to be used. The gauges then have to be mounted to the actual test blades prior to testing, including special wiring provisions if rotor blades are to be instrumented.

References

1. J.D. Anderson. Fundamentals of Aerodynamics. McGraw Hill, 1991.
2. ASME/ANSI MFC-7M-1987, *Measurement of Gas Flow by Means of Critical Flow Venturi Nozzles, An American National Standard*. The American Society of Mechanical Engineers, 1987.
3. D.W. Bryer, R.C. Pankhurst. Pressure-Probe Methods for Determining Wind Speed and Flow Direction. Her Majesty's Stationary Office, 1971.
4. Y.Cai. *Aerodynamic Performance Measurements in a Fully Scaled Turbine*. S.M. Thesis, Department of Aeronautics and Astronautics, Massachusetts Institute of Technology, 1998.
5. H.W. Coleman, W.G. Steele. Experimentation and Uncertainty Analysis for Engineers. 2nd Edition. John Wiley and Sons, 1999.
6. Chemical Rubber Company. CRC Handbook of Chemistry and Physics, 77th Edition. CRC Press, 1996.
7. DuPont Films. Material Data Sheet: Kapton[®] Polyimide Film, General Specifications. DuPont, 1997.
8. G.R. Guenette. *A Fully Scaled Short Duration Turbine Experiment*. Sc.D Thesis, Department of Aeronautics and Astronautics, Massachusetts Institute of Technology, 1985.
9. J.J. Jacobs. *Efficiency Measurements of a Single Stage Turbine in a Short Duration Facility*. S.M. Thesis, Department of Aeronautics and Astronautics, Massachusetts Institute of Technology, 1998.
10. R.C. Keogh. *Aerodynamic Performance Measurement of a Film-Cooled Turbine Stage*. Ph.D. Thesis, Department of Aeronautics and Astronautics, Massachusetts Institute of Technology, 2001.
11. D.R. Kirk, G.R. Guenette, S.P. Lukachko, and I.A. Waitz. *Near Wall Reaction Effects on Film-Cooled Flat Plate Heat Transfer*.
12. M. Kohler. Etching in Microsystems Technology. Wiley-VCH, 1999.

13. F.A. Lowenheim. Modern Electroplating. John Wiley and Sons, 1974.
14. E. Ower, R.C. Pankhurst. The Measurement of Air Flow. Pergamon Press, 1977.
15. M. Pianko. *Modern Methods of Testing Rotating Components of Turbomachines (Instrumentation), North Atlantic Treaty Organization (NATO) Advisory Group for Aerospace Research and Development (AGARD)*. Technical Editing and Reproductions Limited, 1975.
16. D.P. Reijnen. *Experimental Study of Boundary Layer Suction in a Transonic Compressor*. Ph.D. Thesis, Department of Aeronautics and Astronautics, Massachusetts Institute of Technology, 1997.
17. W. Riedel. Electroless Nickel Plating. Finishing Publications Limited, 1991.
18. D.R. Sadoway, Personal Communications, Department of Materials Science and Engineering, Massachusetts Institute of Technology, 2001.
19. T. Shang. *Influence of Inlet Temperature Distortion on Turbine Heat Transfer*. Ph.D. Thesis, Department of Aeronautics and Astronautics, Massachusetts Institute of Technology, 1995.
20. Shipley Company. Material Data Sheet: Accelerator 19. Shipley Company, 1978.
21. Shipley Company. Material Data Sheet: Catalyst 9F. Shipley Company, 1983.
22. Shipley Company. Material Data Sheet: Cleaner/Conditioner 1110A. Shipley Company, 1982.
23. Shipley Company. Material Data Sheet: Electroless Nickel PM-980. Shipley Company, 1983.
24. C.H. Sieverding, T. Arts, R. Denos, J.-F. Brouckaert. *Measurement Techniques for Unsteady Flows in Turbomachines*. Experiments in Fluids 28, 285-321, 2000.
25. C.M. Spadaccini. *Aerodynamic Performance Measurements of a Fully Scaled, Film-Cooled, Turbine Stage*. S.M. Thesis, Department of Aeronautics and Astronautics, Massachusetts Institute of Technology, 1999.
26. R. Suchentrunk. Metalizing of Plastics – A Handbook of Theory and Practice. Finishing Publications Limited, 1993.
27. W.T. Thompkins, J.L. Kerrebrock. *Exit Flow from a Transonic Compressor Rotor*. Gas Turbine Laboratory Report 123, Massachusetts Institute of Technology, 1975.

28. B.P. Van Poppel. *Tip Casing Heat Transfer Measurements of a Film-Cooled Turbine Stage in a Short Duration Facility*. S.M. Thesis, Department of Aeronautics and Astronautics, Massachusetts Institute of Technology, 2001.
29. G.G. Vining. Statistical Methods for Engineers. Duxbury Press, 1998.
30. R. Weast, S. Shelby. Handbook of Chemistry and Physics. 63rd Edition. Chemical Rubber Company, 1982.

Appendix A: Heat Flux Gauge Fabrication Procedure

A.1 Cleaning of Substrate Material

- 1) Cut a 7.5 in. by 5.5 in. piece of 25 μm thick Kapton[®] Type HN polyimide film and mount in plexiglass frame.
- 2) Mount plexiglass frame on top of metal jig and carefully cut two sets of 32 through holes in the polyimide film using a fine scalpel blade.
- 3) Running water rinse, 1 min. (with hose).
- 4) Cleaner/Conditioner 1110A solution, 5 min. with agitation ($T_{1110A} = 165\text{-}170\text{ }^{\circ}\text{F}$).
- 5) Running water rinse, 5 min. (with hose).
- 6) Deionized water rinse.
- 7) KOH etch solution, 12 min.
- 8) Running water rinse, 5 min. (with hose).
- 9) Deionized water rinse.
- 10) Cleaner/Conditioner 1110A solution, 5 min. with agitation ($T_{1110A} = 165\text{-}170\text{ }^{\circ}\text{F}$).
- 11) Running water rinse, 5 min. (with hose).
- 12) Deionized water rinse.
- 13) HCl solution, 1 min.
- 14) Two beaker static rinse baths, 2 min. in each beaker.
- 15) Deionized water rinse.
- 16) Oven dry, approximately 140 $^{\circ}\text{F}$ for 60 min.

A.2 Electroless Nickel Plating

- 1) Cut cleaned polyimide sample into two separate pieces, each with 32 through holes.
Mount sample in plastic tweezers.
- 2) Deionized water rinse.
- 3) Cleaner/Conditioner 1110A solution, 5 min. with agitation ($T_{1110A} = 165-170\text{ }^{\circ}\text{F}$).
- 4) Two beaker static rinse baths, 2 min. in each beaker.
- 5) Deionized water rinse.
- 6) HCl solution, 1 min.
- 7) Catalyst-9F solution, 2 min.
- 8) Two beaker static rinse baths, 2 min. in each beaker. Change position of plastic tweezers in between the two rinse steps.
- 9) Deionized water rinse.
- 10) Accelerator-19 solution, 30 sec.
- 11) Single beaker static rinse, 2 min.
- 12) Deionized water rinse.
- 13) PM-980 nickel plating solution, 6 min. ($T_{PM-980} = 25\text{ }^{\circ}\text{C}$, pH = 8.3-8.4). Use NH_4OH to adjust pH to proper level.
- 14) Deionized water rinse.
- 15) Hang from tweezers to dry at room temperature, 2 hours.
- 16) Rinse in ethanol.
- 17) Static soak in deionized water.
- 18) Hang from tweezers to dry at room temperature, 2 hours.

A.3 Electrolytic Plating of Gauge Leads

- 1) Following photomachining, apply small amount Shipley 1805 Photoresist to one side of gauge sensor heads using soft solder piece. Use just enough resist to cover the sensors.
- 2) Oven bake, approximately $115\text{ }^{\circ}\text{F}$ for 60 min.

- 3) Apply small amount of Shipley 1805 Photoresist to gauge sensor heads on reverse side of gauge. Use just enough resist to cover gauge sensors.
- 4) Oven bake, approximately 115 °F for 60 min.
- 5) Mount polyimide sample in small plexiglass frame. Replace copper wire in the groove of the frame. Replace copper tape on other side of frame to complete conductivity.
- 6) Cut two copper anodes, each 0.75 times the surface area of the polyimide sample. Drill small hole in each anode and attach copper wire.
- 7) Suspend sample and anode in plating bath solution and connect external DC power source to copper wires. Pass 15 mA/in.² DC cathode current density for 220 s. Ensure that anodes are evenly spaced from cathode, and agitate solution.
- 8) Remove plated sample from frame and rinse in deionized water.
- 9) Hang from tweezers to dry at room temperature, 2 hours.
- 10) Static soak in ethanol until resist is removed. This step should not require and physical manipulation of the sample.
- 11) Hang from tweezers to dry at room temperature, 2 hours.

A.4 Chemical Compositions

Cleaner/Conditioner 1110A Solution

Deionized Water	95 % by volume
Shipley Cleaner/Conditioner 1110A	5 % by volume

KOH Etch Solution

Deionized Water	17 % by volume
Ethanol	83 % by volume
Potassium Hydroxide, KOH, pellets	56.1 g/L of solution

HCl Solution

Deionized Water	75 % by volume
Hydrochloric Acid	25 % by volume

Catalyst-9F Solution

Deionized Water	40 % by volume
Hydrochloric Acid	40 % by volume
Shipley Catalyst-9F	20 % by volume

Accelerator-19 Solution

Deionized Water	83.3 % by volume
Shipley Accelerator-19	17.7 % by volume

PM-980 Nickel Plating Solution

Deionized Water	86 % by volume
Shipley PM-980	14 % by volume
Adjust pH using NH_4OH	

Copper Electrolytic Plating Solution

Copper (II) sulphate pentahydrate, $\text{CuSO}_4 \cdot 5\text{H}_2\text{O}$	30 g/L
Sodium pyrophosphate decahydrate, $\text{Na}_4\text{P}_2\text{O}_7 \cdot 10\text{H}_2\text{O}$	120 g/L
Disodium hydrogen phosphate, Na_2HPO_4	36 g/L

3231-24